Dissertation

submitted to the

Combined Faculties of the Natural Sciences and Mathematics

of the Ruperto-Carola-University of Heidelberg. Germany

for the degree of

Doctor of Natural Sciences

Put forward by

Kirsten Schnülle, Dipl.-Phys.

born in: Bremen

Oral examination: July 27, 2017

Studying the Radiative Response

of Circumnuclear Dust

of AGNs

Referees: **Prof. Dr. Hans-Walter Rix**
Prof. Dr. Jochen Heidt

Abstract

Radius measurements of dust tori around the central engine of luminous active galaxies open up the possibility of probing cosmological models out to redshifts beyond where supernovae can be used. Yet, the value of dust tori as standard candles is constrained by the substantial intrinsic scatter in the size-luminosity relation found for samples of AGNs. Indicated by single objects, a probable cause of this scatter is a non-trivial variation in the dust location with the luminosity of the central engine, due to sublimation events and subsequent long-term reformation of the hot dust surface radiating at near-infrared wavelengths.

In this work, I developed a refined dust reverberation model allowing to measure torus sizes and additional observables characterizing the temperature state, stability, and distribution of the innermost, hot dust in AGNs.
Optical to near-infrared photometric data were observed for 24 type 1 AGNs. Of these, I have analyzed the Seyfert 1 galaxies NGC 4151, Ark 120, NGC 5548, and NGC 3227. The derived inner torus radii fit very well into the established size-luminosity relation. While three objects are well-described by a standard model without sublimation, the data of one object could be fit satisfactorily only after allowing for dust sublimation events in the model.

Zusammenfassung

Radiusmessungen von Staubtori um leuchtkräftige aktive Galaxienkerne bieten die Möglichkeit, kosmologische Modelle jenseits von Rotverschiebungen zu testen, bei denen Supernovae als Standardkerze dienen können. Die Nutzbarkeit von Staub-Tori als Standardkerzen ist jedoch stark eingeschränkt durch die wesentliche intrinsische Streuung in der Radius-Leuchtkraft-Relation für AGN-Samples. Wie Daten einzelner Objekte nahelegen, ist eine wahrscheinliche Ursache dieser Streuung eine nicht-triviale Änderung des Torusradius mit der Leuchtkraft der Akkretionsscheibe, hervorgerufen durch Sublimationsereignisse und anschließende Neubildung der heißen Stauboberfläche, welche im nah-infraroten Wellenlängenbereich emittiert.

In dieser Arbeit habe ich ein erweitertes “dust reverberation”-Modell entwickelt, welches die Möglichkeit bietet, Torusradien und weitere Observablen zu messen, die den Temperaturzustand, die Stabilität und die Verteilung des innersten heißen Staubes in AGN charakterisieren.
Optische bis nah-infrarote photometrische Daten wurden für 24 AGN des Typs 1 aufgenommen, wovon ich die Seyfert 1-Galaxien NGC 4151, Ark 120, NGC 5548 und NGC 3227 mit der hier entwickelten Methode analysiert habe. Die abgeleiteten inneren Torusradien passen sehr gut in die etablierte Radius-Leuchtkraft-Relation. Während drei Objekte durch ein Standardmodell ohne Staubsublimation beschrieben werden können, konnten die Daten eines Objekts erst zufriedenstellend abgebildet werden, nachdem ich Sublimationsereignisse im Modell zugelassen habe.

Contents

1 Introduction

1.1 This work

In the thesis presented here, hot dust reverberation analyses are performed on optical to near-infrared (NIR) multi-epoch multi-wavelength data of type 1 active galactic nuclei (AGNs). In contrast to determining the hot dust reverberation delay by a conventional CCF analysis, a maximum likelihood approach is applied in order to be able to derive additional characteristic quantities of the hot dust, such as the hot dust temperature. Central idea is to infer to which extent the hot dust radius can sure enough be identified with the sublimation radius, as is implicitly assumed, for instance, in the radius-luminosity relation for the NIR hot dust around AGNs. For that purpose, general aim is to verify whether or not the hot dust in AGNs is found at or below sublimation temperatures. A further goal is to investigate the long-term stability of the hot dust and detect potential changes in its reverberation delay and radial distribution, in order to conclude on conditions for dust survival and formation in the radiation field of the AGN.

While the first project (Chapter 3) was started off with a limited data set on a single target, and a simple single-epoch approach using a non-linear least-square fitting algorithm, the data, the model and techniques were extended and refined during the course of the thesis.

Specifically, for the second project (Chapter 4), the data set was substantially expanded, by using a significantly longer time series and a broader wavelength coverage. Reduction and analysis techniques were extended as well: precise photometry is performed with an image subtraction method. Further, a multi-epoch multi-wavelength Markov Chain Monte Carlo (MCMC) fit is applied, in order to recover characteristic quantities of the hot dust distribution (inspired by the works of Zu et al. (2011) and Hernitschek et al. (2014) for the BLR), and using the formalism developed by Rybicki & Press (1992).

For the third project (Chapter 5), the data set was again significantly extended. To apply the methods developed in the previous analysis to a broader AGN sample, and to derive sample properties, observations were carried out on 23 additional type 1 AGNs. Three of these additional sources have been analyzed until now, as presented in Chapter 5.3. The methods from the previous analysis were modified to work on the different observational setup and different targets. Motivated by the light-curves of one target, the developed reverberation model was substantially extended for the inclusion of dust sublimation events.

Theoretical and observational fundamentals for the context of this work are given in Chapter 1, starting from Sect. 1.2. Chapter 2 introduces the models developed throughout this work, as well as the techniques used and implemented. Chapters 3 - 5 present details on the observed data, as well as results and discussions on the analyses carried out within the three projects of this thesis. Conclusions as well as an outlook are given in Chapter 6.

1.2 Active Galactic Nuclei

This Section gives a brief overview on AGNs and dust tori in AGNs. The contents are mostly based on Antonucci (1993), Peterson (1997), Ryden et al. (2010), and Bianchi et al. (2012).

1.2.1 The AGN phenomenon

An AGN is a very compact region at the center of a galaxy that emits an unusually large fraction of non-stellar (and often non-thermal) light, resulting from energetic and violent processes in the nucleus. Typically, the luminosity of the central source is so high that it is as bright or even 100 times (or more) brighter than the light emitted by all the stars of the host galaxy. These enormous amounts of energy are produced by the rapid accretion of matter onto a supermassive black hole in the center of the active galaxy. AGN emission is variable on short timescales at almost all wavelengths, with the variability timescale depending both on AGN luminosity and wavelength. In many AGNs, the ultraviolet (UV) to infrared (IR) part of the spectrum is dominated by strong emission lines. Some AGNs possess prominent jets that are observed at X-ray, visible and radio wavelengths, consisting of ionized gas flowing outward at relativistic speeds.
Many different types of AGNs have been observed, though their distinction is often rather historically than physically motivated. Conveniently, these different types are assigned to either of two main classes, namely radio-quiet and radio-loud AGNs. The main types of AGNs are presented in the following.

Radio-quiet AGNs:

- Seyfert galaxies are the objects studied in this work. They are spiral or irregular galaxies with luminous and variable nuclear optical continuum emission, and prominent emission lines in their spectra. Some Seyferts show strong nuclear X-ray emission. While Seyfert 1 AGNs possess both narrow emission lines (with widths of a few hundred km s^{-1}) and broad emission lines (widths $10^3 - 10^4$km s^{-1}) in their spectrum, Seyfert 2 AGNs show only narrow emission lines. Broad and narrow emission lines arise in different regions of the AGN. Broad lines originate from permitted transitions in rapidly moving high-density clouds of atomic gas close to the nucleus. Here, forbidden transitions are collisionally suppressed in the high-density gas. The narrow lines arise both from permitted and forbidden transitions at distances farther out. The nuclei of Seyfert galaxies have typical bolometric luminosities of $10^8 - 10^{12}$ solar luminosities.

- Radio-quiet quasars (RQQs) can be thought of as very luminous Seyfert 1 AGNs. RQQs show strong and variable X-ray to optical continuum emission, narrow and broad emission lines. They are hosted by spiral, irregular or elliptical galaxies. The first discovered quasars had optical luminosities greater than that of the host galaxy, which made them appear quasi-stellar in optical images. For a long time, there was an apparent absence of RQQ 2 AGNS, the high-luminosity analogue of the Seyfert 2 AGNs. This was caused by the fact that quasars were searched for in the optical surveys, designed to detect objects with strong non-stellar UV-optical continuum emission[1] (McLean et al., 1998). Not showing this emission, RQQ 2 AGNs appear like normal galaxies in the optical, and were therefore only detected in more recent searches at X-ray and infrared wavelengths (Lacy et al., 2005; Martínez-Sansigre et al., 2006a,b; Ridgway et al., 2009). Quasars can have intrinsic bolometric luminosities of more than 10^{14} solar luminosities.

Seyfert 1 and RQQ 1 galaxies are often referred to as "type 1" AGNs, whereas Seyfert 2 and RQQ 2 objects are named "type 2" AGNs. Radio-quiet AGNs are hosted by spiral, irregular or elliptical galaxies.

Radio-loud AGNs:

- Radio-loud quasars show the same emission as radio-quiet quasars, with the addition of significant emission at X-ray, visible and radio wavelengths resulting from a relativistic jet emerging from the center, sometimes inflating gigantic extended radio lobes (up to Mpc scales). The radio spectra of these sources are very steep (i.e., $F_\nu \propto \nu^{-\alpha}$, with $\alpha \geq 0.5$).

- Blazars are characterized by their strongly and rapidly variable, polarized emission at X-ray, optical, and radio wavelengths. Blazars comprise optically violent variables (OVVs) and BL Lac objects. Whereas OVVs can be thought of as radio-loud quasars with the additional rapidly variable component, BL Lac objects show no strong emission lines in their spectra. In contrast to normal radio-loud quasars, blazars show a rather flat radio spectrum (i.e., $F_\nu \propto \nu^{-\alpha}$, with $\alpha < 0.5$), and these sources appear rather compact.

- Radio galaxies exhibit compact and extended radio emission. They are often classified as either low-luminosity (named Fanaroff-Riley type I, or FRI) radio galaxies, or high-luminosity (FRII) radio galaxies.

Radio-loud AGNs do not seem to be found in spiral galaxies, but almost always in elliptical galaxies or merging systems.

1.2.2 Unification models

In the radio-quiet unification scheme, Seyfert galaxies and RQQs are recognized as intrinsically same objects, with the primary difference being the luminosity of the central engine.

[1] Seyfert 2 AGNs, in contrast, are more easily detected, since they are searched for locally, mainly based on their host galaxy properties (Sulentic et al., 2012).

Today it is known that there is a smooth transition between Seyfert AGNs and RQQs, and their distinction is rather arbitrary. Moreover, and more importantly, the presence of high- and low-ionization forbidden emission lines as well as very high-ionization coronal lines in type 1 as well and type 2 AGNs suggest that these objects are powered by the intrinsically same mechanism. The radio-quiet unification model attributes the observed absence of strong UV-optical continuum and broad emission lines to a viewing-angle dependent obscuration of the central region of the AGN by a torus of dust. The narrow-line producing region is not affected by obscuration since it is located beyond the obscuring medium. A radio-quiet AGN would, in this picture, consist of the following ingredients:

- The central engine: A supermassive black hole at the center of the galaxy rapidly accretes matter which forms an accretion disc (AD). Dissipative processes in the disk transport matter inwards and angular momentum outwards. The dissipated energy of matter moving inwards heats up the accretion disk which emits strong continuum radiation peaking at UV-optical wavelengths. A corona of hot material above the accretion disc scatters up part of the emitted photons to X-ray energies by the inverse Compton process. The Schwarzschild radius of a typical supermassive black hole is $R_S \approx 10^{-5}$ parsec (pc), assuming a black hole mass of $M_{BH} = 10^8$ solar masses. The "sphere of influence", i.e., the region of space within which the gravitational potential of such a black hole dominates over that of the surrounding stars, is on the order of 10 parsecs, roughly 10^6 times larger than the Schwarzschild radius. The UV-optical emission from the AD originates from scales of roughly 3-100 times the Schwarzschild radius.

- Broad-line region (BLR): Outside the accretion disc, at 10^3 Schwarzschild radii from the center (0.01-1 pc, depending on the luminosity of the central source), clouds of high-density atomic gas move at very high speeds (10^3-10^4 km s^{-1}) around the central black hole. This gas is heavily ionized by the AD radiation and emits characteristic emission lines which are Doppler-broadened due to the high velocities.

- Dust torus: Outside the BLR, a dusty obscurer is located. A lower limit for the innermost "edge" of this obscurer is given by the dust sublimation radius (which is typically at sub-parsec to parsec (pc) scales, depending on the AD luminosity), i.e., the closest point to the central source where dust grains can survive the intense UV radiation. Dust at smaller radii is sublimated. Since the obscuration of the central engine and BLR is orientation-dependent, the accumulation of dust has to be non-spherically symmetric. Rotational symmetry (along the rotational axis of the AD and/or the black hole, if the dust is physically related to the accreted material and/or gravitationally coupled to the black hole) then favors the shape of a toroidal dust distribution. The radial extent of the dusty obscurer can be up to 10-20 times the sublimation radius (Ramos Almeida et al., 2009).

- Narrow-line region (NLR): Beyond the obscuring toroidal dust distribution, at 100 pc scales, clouds of gas moving at speeds of ≈ 100 km s^{-1} are ionized by the central source and emit characteristic lines that are narrow compared to the broad emission

lines due to the lower velocities. Due to the presence of the dust torus, a bi-cone shape of the NLR is expected, with the opening angle of the cones being defined by the dust torus.

Numerous observational evidence in favor of the radio-quiet unified model has been presented up to now (Antonucci & Miller, 1985; Smith & Done, 1996; Maiolino et al., 1998; Pogge, 1988; Storchi-Bergmann et al., 1992; Suganuma et al., 2006; Jaffe et al., 2004; Tristram et al., 2009; Kishimoto et al., 2011a), and similar unification schemes exist for radio-loud AGNs.

In the so-called grand unification scheme, one possible explanation for the observed dichotomy of radio-quiet and radio-loud AGNs is an intrinsically different black hole spin, as a high spin is needed for the AGN to successfully generate powerful jets by magnetohydrodynamic acceleration near the black hole. The postulated dichotomy in black hole spins might be caused by different merger histories of the two AGN classes. In this scheme, a radio-loud AGN would thus consist of the same components as a radio-quiet AGN , with the addition of a relativistic jet and jet-related structures.

Despite the success of AGN unification, there is some indication that this picture might be slightly too simple: evidence has been accumulated for the existence of "true" Seyfert 2 AGNs, i.e., Seyferts intrinsically lacking a BLR (e.g. Veilleux et al. (1997). These "'true" Seyfert 2 AGNs do not seem to give a real contradiction to unification theories, as a critical threshold in luminosity has been confirmed below which an AGN is apparently not capable of forming a BLR (e.g. Nicastro et al. (2003), Bianchi et al. (2008), and Elitzur & Ho (2009)). In some low-luminosity, low-excitation, low-accretion radio-loud AGNs, however, both the hidden nuclear component and evidence for a dust torus are missing (Chiaberge et al., 2002; Ogle et al., 2006). These objects seem to form a different class that cannot be unified with radio-loud quasars.

1.2.3 Astrophysical importance of AGNs and AGN tori

AGNs are highly relevant for cosmology. Being the most luminous persistent sources of electromagnetic radiation in the universe, they offer the possibility to measure distances and constrain cosmological parameters at redshifts beyond where supernovae can be used (Elvis, 2014).

- AGNs can be used as a standard candle. Standard candles are astronomical objects for which the intrinsic luminosity is known. By relating the observed flux F of these targets to their intrinsic luminosity L, their luminosity distance (and the distance of their host galaxy) can be calculated according to:

$$D_L = \sqrt{\frac{L}{4\pi F}}\,. \tag{1.1}$$

  Examples for standard candles are Cepheid variables and supernovae of type 1a. Determining the luminosity distance of astronomical objects as a function of redshift is

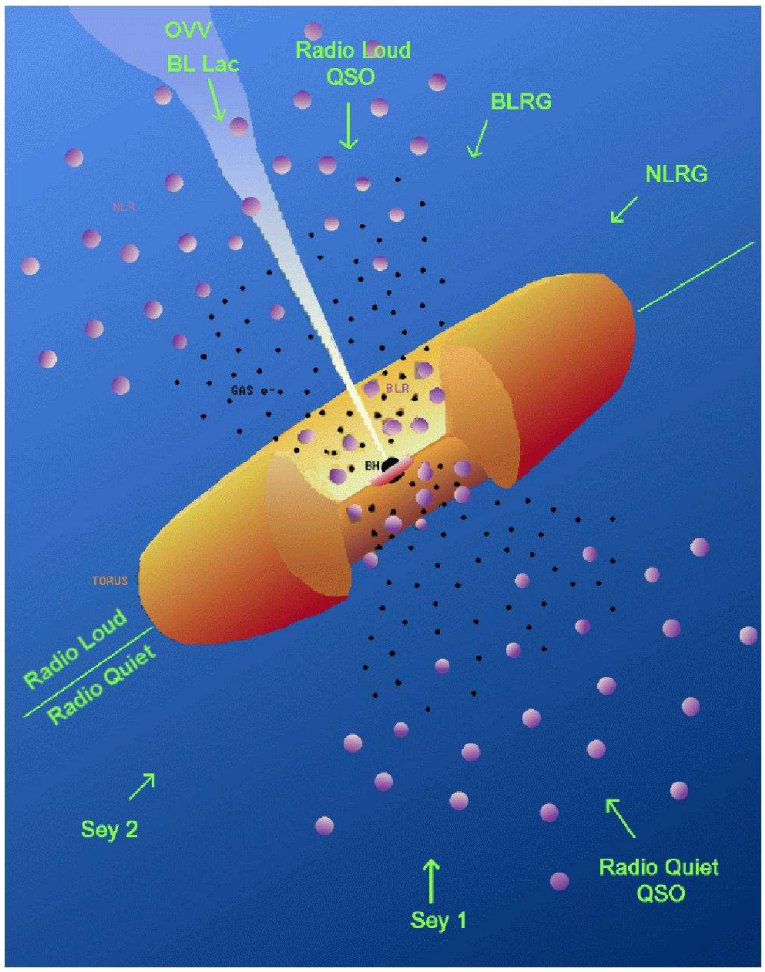

Figure 1.1: *The grand AGN unification scheme (Credit: Southampton Gamma Ray Astrophysics Group).*

important for constraining the cosmological model. AGNs can be used as standard candles by determining their observed brightness, and the distance of the BLR from the center, which is known to correlate with the intrinsic source luminosity according to $R_{\mathrm{BLR}} \propto \sqrt{L}$. Alternatively, the location of the dusty torus – showing a similar correlation with the AD luminosity – can be used as a means to estimate the intrinsic luminosity (Oknyanskij, 1999; Yoshii et al., 2014). The value of this method is still constrained by the substantial scatter in the observed size-luminosity relations, both for the BLR (Sulentic et al., 2012) and the dust torus (Koshida et al., 2014).

- AGNs can also be used as standard rulers using the dust parallax method. This has successfully been done by Hönig et al. (2014) for the case of the Seyfert 1 AGN NGC 4151. The method works in analogy to parallax measurements, however the direction of par-

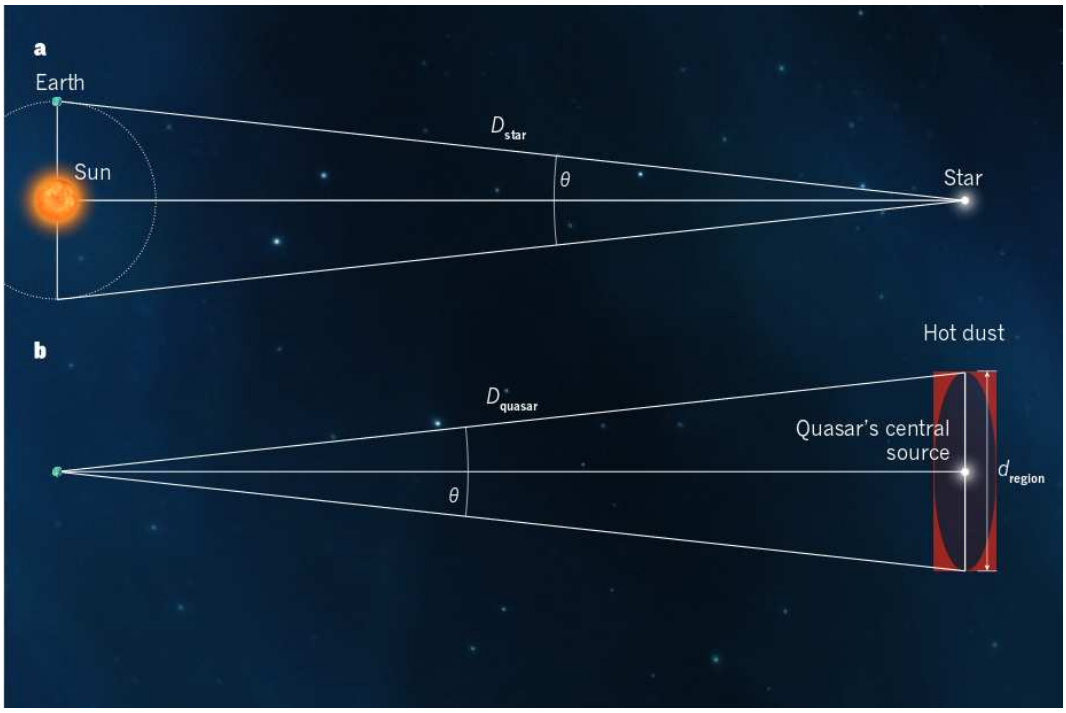

Figure 1.2: *Dust parallax method for AGNs as standard rulers, as proposed by Hönig et al. (2014).*

allactic triangle is being inverted, as shown in Fig. 1.2. The angular diameter distance

$$D_{\mathrm{A}} = \frac{R_{\mathrm{dust}}}{\theta_{\mathrm{dust}}} \tag{1.2}$$

of the AGN can then be inferred by the ratio of the physical and angular sizes of the hot dust torus. Instead of the earth-sun distance as physical size, the radius R_{dust} of the inner edge of the hot dust torus – determined by NIR hot dust reverberation measurements – is used. The angular size θ_{dust} of the hot dust torus is determined by NIR interferometry. Because long-term brightness changes can cause physical and angular sizes to increase or decrease, photometric and interferometric data should be recorded more or less contemporaneously. High precision is needed to get an accuracy of this method below ten percent. In principle, BLR sizes could also be used for this method. However, BLR angular sizes are yet too difficult to resolve with interferometry. Direct BLR angular size measurements could be feasible, however, with the next generation of VLTI instruments (Rakshit et al., 2015) and ELT spectro-astrometry (Stern et al., 2015).

1.3 Dust in AGNs

This Section gives an overview on what is known about the hot dust torus around in AGNs, as well as on models to describe it and observational methods to "resolve" it. The presentation

is mainly based on Bianchi et al. (2012), Hönig & Kishimoto (2010), Hönig et al. (2010), Hönig & Kishimoto (2011), Monnier (2003), and Peterson (1997).

1.3.1 Observational evidence for the dusty torus

The presence of a dusty obscurer around the central region of AGNs was postulated in unified AGNs models, to be able to explain the dichotomy between type 1 and type 2 AGNs. Early evidence for the existence of very hot dust close to sublimation temperature was presented by Storchi-Bergmann et al. (1992), Oliva et al. (1999), and Alonso-Herrero et al. (2001), by detecting the non-stellar continuum emission coming from the nuclear hot dust in near- to mid-infrared photometric and spectroscopic observations of a sample of Seyfert 1 and 2 AGNs, and comparing it to the expected signal of AD radiation reverberated by a dusty torus.

The innermost hot dust around AGNs is expected at the sublimation radius, and has indeed been confirmed to be located at subparsec scales for Seyfert AGNs and rather on parsec scales for luminous quasars. The predicted dependency of the dust location on the luminosity of the central engine as $R_{\mathrm{dust}} \propto \sqrt{L}$ has been confirmed for a sample of AGNs in extensive NIR reverberation campaigns (Oknyanskij et al., 1999; Suganuma et al., 2006; Koshida et al., 2009, 2014).

In the past decade, it has become possible to directly resolve and "image" dust tori on subparsec scales using mid-infrared interferometry. Jaffe et al. (2004) were one of the first to spatially resolve AGN dust tori. For the Seyfert 2 galaxy NGC 1068, they found that the dust distribution was best described by a two-component model, with an inner, hot (> 800 K), compact, and rather elongated structure with 0.5 pc thickness, and an outer, cooler (≈ 300 K), extended, less elongated component at a few parsecs scale. Succeeding observations carried out on other Seyfert 2s as well as Seyfert 1s led to similar results (Tristram et al., 2007; Burtscher et al., 2009; Tristram et al., 2009). Subsequently, the innermost hot dust was resolved in NIR interferometric observations, for instance by Swain et al. (2003), Pott et al. (2010), Kishimoto et al. (2011a), Weigelt et al. (2012), and Kishimoto et al. (2013), confirming the sub-parsec scale of the inner hot dust location in Seyfert AGNs. As for the reverberation measurements, size-luminosity relations of the form $R_{\mathrm{dust}} \propto \sqrt{L}$ have been found in mid- and near-interferometric observations as well.

Combining information from observations and torus radiative transfer models, it became clear that the dust torus is likely to be clumpy, i.e., to consist of dust clouds rather than of a homogeneous distribution of single grains, as will be discussed in more detail in Sect. 1.3.2.

Moreover, SED modeling suggests that the simple single-component dust torus model cannot explain typical infrared SEDs of AGNs (Mor et al., 2009), as shown in Fig. 1.3. Instead, the authors claim the existence of at least three distinct components: NLR dust clouds, a silicate-type clumpy dust torus as modeled by Nenkova et al. (2002), Nenkova et al. (2008a), and Nenkova et al. (2008b), and very hot graphite-only dust clouds located

between the outer edge of the BLR and the sublimation radius for silicate dust. It is this innermost hot graphite dust component (corresponding to the hot, compact component also found by Jaffe et al. (2004) with interferometry) that is studied in this thesis.

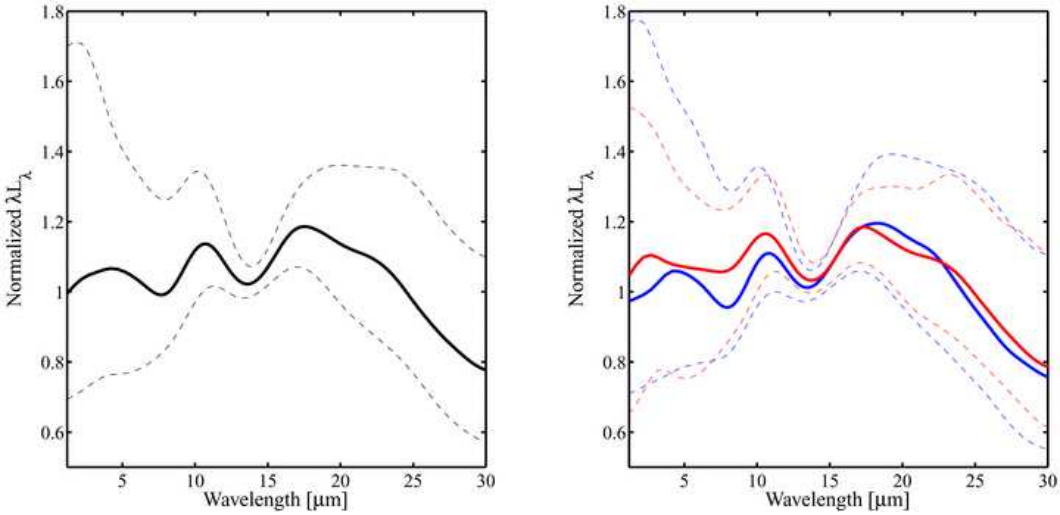

Figure 1.3: *Intrinsic AGN SEDs, i.e., SEDs corrected for the emission from star-forming regions in the host galaxy. Shown are the median intrinsic AGN SEDs for a representative sample of Narrow-Line Seyfert 1 galaxies (blue) and Broad-Line Seyfert 1 galaxies (red). The dashed lines represent the 25th and 75th percentiles of each subgroup. It is apparent that all SEDs exhibit a similar shape, with three peaks at short ($\leq 5\mu m$), medium and long wavelengths, corresponding to the three separate dust components (very hot graphite-only dust clouds, silicate dust torus clouds, and NLR clouds) proposed by Mor & Netzer (2012).*

1.3.2 From smooth to clumpy torus models

Several theoretical models of the physics and structure of the dusty torus have been proposed, trying to reproduce the observed properties.

Early torus models used a simple toroidal structure with a uniform distribution of gas and dust (e.g. Krolik & Begelman (1988)). Problems concerning the dynamical stability in these models were solved by assuming that either the infrared photons within the torus (Krolik, 2007), or turbulence introduced by supernovae or stellar winds (Wada & Tomisaka, 2005; Watabe & Umemura, 2005), would keep the dust distribution geometrically thick. Alternatively, it has been proposed that the observed wide angle of obscuration can be achieved by a warped or tilted disk, which would then not require a geometrically thick torus (Nayakshin, 2005; Lawrence & Elvis, 2010). Still, neither of the proposed "smooth" torus models has been able to account for all of the observed properties of the dusty obscurer, more specifically:

- the very broad infrared spectral energy distribution (SED),
- the small (pc-scale) size of the obscurer, and

- the large scatter of the depth of the 9.7 μm silicate absorption feature as a function of the X-ray gaseous column density.

To reproduce the broad infrared SED, a wide range of dust temperatures is needed. Therefore, in contrast to smooth parsec-scale models (Krolik & Begelman, 1988; Pier & Krolik, 1992), some of the smooth torus models proposed more extended geometries up to 100 pc (Granato & Danese, 1994). While being able to reproduce the observed SEDs, these models contradict the compact parsec-scale size of the dust torus observed in mid-infrared interferometric observations (e.g. Jaffe et al. (2004), Tristram et al. (2007)).

Observations of the 9.7 μm silicate feature (which traces dust absorption at mid-IR wavelengths) in large sample of AGNs (Shi et al., 2006) show that this feature changes from emission to absorption with increasing H I column density. Since the H I column density is a measure of obscuration, this behavior is consistent with unification models, in which the 9.7 μm silicate feature is generally expected in emission for type 1 AGNs, and in absorption for type 2 AGNs. However, the scatter in the observed relation is found to be unexpectedly large (Shi et al., 2006). Another puzzle is the absence of any deeply absorbed features, as well as the fact that the feature is observed in emission in some type 2 AGNs (Nikutta et al., 2009).

These discrepancies between models and observations of the dust torus around AGNs can be overcome when allowing for a clumpy distribution of the dust with a relatively low local dust volume filling factor, i.e., the dust is not smoothly distributed over the whole volume of the torus, but accumulates in clouds. The mean free path between clouds is substantially larger than the cloud size, which makes the torus appear clumpy.
Clumpy torus models are capable of reproducing the required temperature range, and thus broad SEDs, even for small torus sizes (Nenkova et al., 2002; Elitzur & Shlosman, 2006; Nenkova et al., 2008b). The radial temperature distributions assumed in clumpy models show a significantly larger scatter than found in the continuous models. There is no rigid temperature-radius relation anymore, because

- in each single dense cloud, a wide range of temperatures is present already, so very different temperatures can be found at roughly the same radial distance from the central engine;

- depending on the local dust distribution, i.e., shielding by other clouds, clouds can be heated directly by the central accretion disk even at large distances, thus the same temperature can be found at very different radii.

Moreover, clumpy models are able to reproduce the observed 9.7 μm silicate feature depths[2]. Whether and to which extent the 9.7 μm silicate feature is found in absorption or

[2]Hönig et al. (2010) find, however, that while clumpy models generally succeed in reproducing the strength of the silicate feature, additional assumptions (such as a radial change of grain and/or dust composition) need to be made in order to explain other observational properties of the silicate feature, e.g. its observed central wavelength.

in emission depends sensitively on the model parameters describing the radial dust distribution, the optical depth of clouds and inclination angle (Hönig et al., 2006; Schartmann et al., 2008; Hönig et al., 2010).
Summarizing here the basic ingredients of a modern clumpy torus radiative transfer model will provide the concepts that form the basis for the reverberation modeling developed throughout this thesis. This is done in the following at the example of the model proposed by Hönig & Kishimoto (2010).

Model strategy

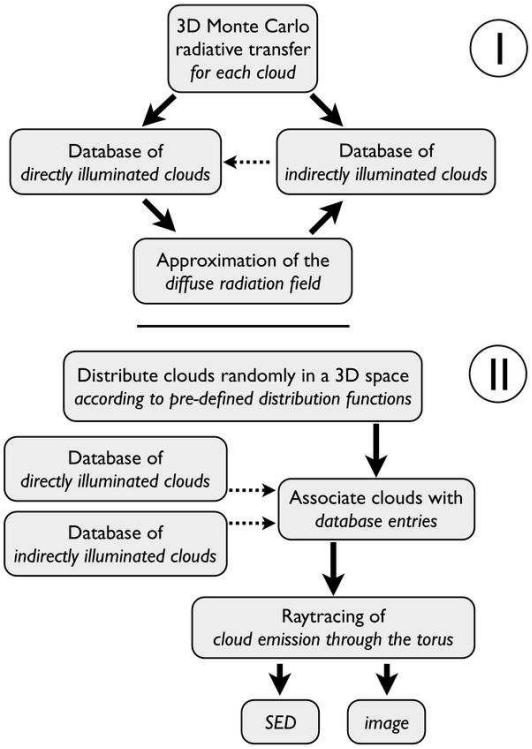

Figure 1.4: *Flow chart of the method for radiative transfer simulations of 3D clumpy tori, as presented by Hönig & Kishimoto (2010).*

The model strategy follows the approach of Nenkova et al. (2008a), but also accounts for the need for a probabilistic treatment of the 3D dust distribution, as required by the statistical nature of clumpy dust distributions. The basic idea is to separate the simulations of individual cloud SEDs and images from the final SEDs and images of the complete torus. The principle of the method is sketched in Fig. 1.4. In a first step, Monte Carlo radiative transfer simulations are used to model the phase-angle-dependent emission for each cloud.

Here, for a given dust composition, the sublimation radius $R_{\rm sub}$[3] is determined, and clouds at various different distances (in units of $R_{\rm sub}$) from the central source are simulated. In a second step, to model the entire torus emission, dust clouds are randomly distributed around the central engine according to pre-defined distribution functions. Here, each cloud is associated with a pre-simulated model cloud from the cloud database calculated in step 1, which consists of two parts:

- clouds that are directly heated by the AGN and
- clouds that are not directly heated due to obscuration by other clouds in the line-of-sight to the AGN. These clouds are only heated indirectly by the diffuse radiation field produced by other clouds in their vicinity.

In a third step, the final torus image and SED are calculated via raytracing along the line-of-sight from each cloud to the observer.

Torus parameters

The random distribution of dust clouds within 3D space is realized via pre-defined distribution functions. Hönig & Kishimoto (2010) characterize the distribution of clouds in the torus by six model parameters:

- the radial dust-cloud distribution power-law index β,
- the effective scale height $h = H(r)/r$,
- the number of clouds along an equatorial line-of-sight N_0,
- the cloud radius $R_{\rm cl;0}$ at the sublimation radius, given in units of $R_{\rm sub}$,
- the cloud-size distribution power-law index b, and
- the outer torus radius $R_{\rm out}$.

The complete 3D dust distribution is then separated into a radial dust distribution η_r and a vertical dust distribution η_z[4] (i.e., $\eta_\phi = \text{const}$, as it should be due to rotational symmetry). Here, η_r can be understood as the normalized number of clouds per unit length, and is given by

$$\eta_r = \frac{1+\beta}{(R_{\rm out}^{1+\beta}-1)} r^{\beta} \cdot \frac{1}{R_{\rm sub}}, \tag{1.3}$$

[3] In their model, Hönig & Kishimoto (2010) assume that the sublimation radius is defined by $R_{\rm sub} = r(T_{\rm sub} = 1500\text{K})$.

[4] Alternatively, Hönig & Kishimoto (2010) also define a vertical cloud distribution η_θ, depending on the coordinate θ in a spherical coordinate system, instead of the coordinate z in cylindrical coordinates. The presentation here is restricted to the cylindrical case.

with the normalization

$$\int_1^{R_{\rm out}} \eta_r \mathrm{d}r = 1\,. \tag{1.4}$$

For the vertical distribution, a Gaussian distribution is used to reproduce the observed smooth transition from the type 1 to type 2 viewing angles. The vertical dust distribution is described by

$$\eta_z = \exp\left(\frac{-z^2}{2H^2}\right), \tag{1.5}$$

with $\eta_z = 1$ for $z = 0$. The cloud-size distribution depends on the radial coordinate as

$$R_{\rm cl}(r) = R_{\rm cl;0} r^b \cdot R_{\rm sub}\,. \tag{1.6}$$

The quantities $r, z, H, R_{\rm cl;0}$ are given in units of $R_{\rm sub}$.

1.3.3 How to measure the dust radius

Interferometry

An interferometer measures the interference pattern produced by light passing two slits or apertures. The interference pattern, also called "fringes", is caused by constructive and destructive interference due to the wave nature of light and the different relative path lengths introduced by the slits.

A brightness distribution on the sky (e.g. a binary system, or an extended object) is said to be resolved by an interferometer when the fringe contrast $|V|$, defined by

$$|V| = \frac{I_{\rm max} - I_{\rm min}}{I_{\rm max} + I_{\rm min}} = \frac{\text{Fringe intensity}}{\text{Average intensity}}, \tag{1.7}$$

goes to zero for the longest separation between two telescopes, projected onto the plane of the sky. Here, $I_{\rm min}$ and $I_{\rm max}$ denote the minimum and maximum intensity of the fringes. As shown in Fig. 1.5, this is the case when the angular separation, e.g. in a binary system equals half the fringe spacing.

Compared to a single telescope with resolution $\Theta \approx \lambda/D$ (with the telescope aperture diameter D), an interferometer has a significantly improved resolution $\Theta \approx \lambda/b_{\rm max}$, where $b_{\rm max}$ is the maximum baseline, i.e., the maximum separation between two telescopes when projected onto the plane of the sky. For a projected baseline length of 100m, this gives a resolution of $\Theta \approx 0.004$ milliarcseconds (mas) at $\lambda = 2\mu$m, which is on the order of typical angular sizes found for the innermost, hot dust. For $\lambda = 10\mu$m, $\Theta \approx 0.02$ mas. Torus sizes in the mid-infrared are typically tens of milliarcseconds.

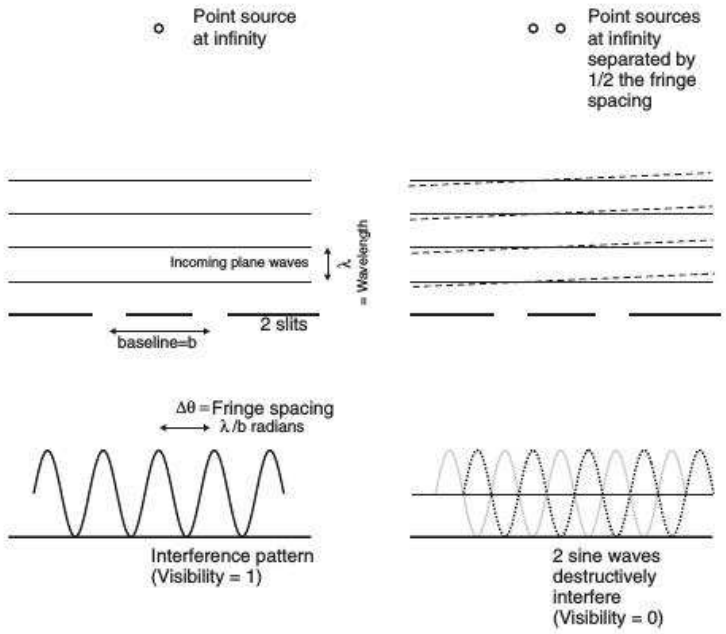

Figure 1.5: *Basic principle of interferometry, as illustrated by Young's two-slit experiment. Left: the visibility amplitude is 1 for an unresolved source. Right: a binary system is said to be resolved when the observed visibility amplitude goes to zero. This is the case when the distance between the binary components equals half the fringe spacing (Credit: Monnier (2003)).*

The complex visibility $V(u,v)$ (defined in the (u,v) plane of spatial frequencies) is the Fourier transform of the brightness distribution $I(x,y)$ on the sky, and can be measured on a discrete number of points. To directly recover the brightness distribution from a Fourier transform of the visibility with sufficient image quality, a good sampling of the visibility in the (u,v) plane is needed. This can be achieved by using multiple telescopes and an accordingly high number of baselines $N = n(n-1)/2$, where n is the number of telescopes. Additionally the rotation of the earth can be used to produce different projected baselines on the plane of the sky for the same separation vectors of the telescopes. In practice, e.g. due to a limited number of telescopes for the same observational project, it is still difficult to achieve a good (u,v) plane coverage. Therefore, instead of directly inferring the brightness distribution from a Fourier transform of the visibility, models of different possible brightness distributions are used, and the "true" brightness distribution is inferred from the best fit to the observed visibilities.

To measure the radius of the hot dust around AGNs, thin-ring models[5] with different sizes (and their corresponding visibility amplitudes) are fit to the observed NIR visibilities, and the inferred hot dust torus size is given by the radius of the best-fit ring model. In Fig. 1.6

[5]In visibility modeling, the thin ring model is the fundamental building block for computing visibilities of complex centro-symmetric objects (Berger & Segransan, 2007).

measured K-band visibilities and the corresponding best-fit ring models are shown for the hot dust around the Seyfert 1 galaxy NGC 4151.

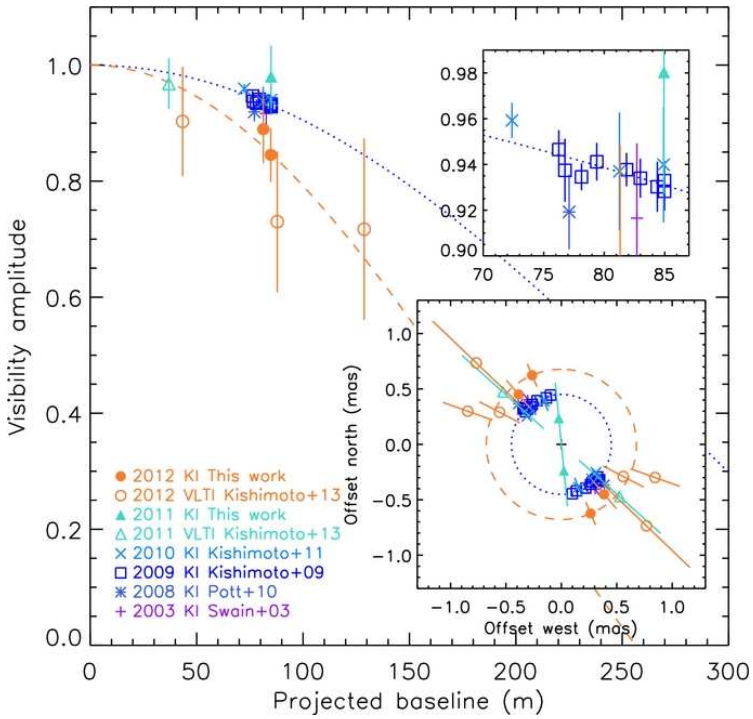

Figure 1.6: *K-band visibilities of the Seyfert 1 galaxy NGC 4151 as published by Kishimoto et al. (2013). The top inset is a zoom into the crowded data points. In the bottom inset, the thin-ring radii are plotted along the baseline position angle. The dashed and dotted lines represent the best-fit thin ring models for the 2009 and 2012 data.*

Reverberation

Reverberation and reverberation mapping techniques have originally been developed for the BLR around a supermassive black hole in an AGN, to draw conclusions on the BLR structure, the time lag $\tau = R_{\rm BLR}/c$ (where $R_{\rm BLR}$ is the radial distance of the line-emitting gas from the AD, and c is the speed of light), the velocity field of characteristic broad emission lines, and the mass of the central black hole. Analyses using this method date back more than two decades for the BLR (Clavel et al., 1991; Peterson et al., 1991; Dietrich et al., 1993; Maoz et al., 1993).

Subsequently, reverberation techniques have also been applied to measure the distance of the hot dust torus from the central engine in AGNs. The idea of dust reverberation is as follows (Peterson, 1993, 1997; Suganuma et al., 2006):
The circumnuclear dust absorbs the radiation coming from the central source and re-emits it in the infrared. The response of dust located at a radial distance $R_{\rm dust}$ from the AD is delayed by a time lag $\tau = R_{\rm dust}/c$ and spread out in time due to light-travel time effects

within the dust torus.

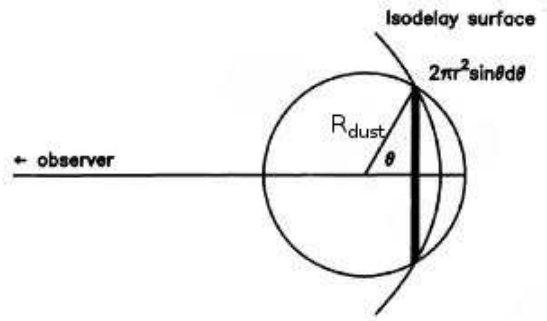

Figure 1.7: *Idealized model of a cloud distribution located in a thin spherical shell: at a given τ, the observer to the left at infinity receives the response from all clouds lying on the "isodelay" surface described by Eq. 1.8 (Credit: Peterson (1993)).*

As a simple example, the response of a thin spherical shell[6] of dust to a δ-function outburst of the AD radiation is described in Fig. 1.7. The δ-pulse expands outwards symmetrically and reaches the dust clouds in the thin shell after a delay $\tau = R_{\rm dust}/c$. The dust particles absorb the AD radiation and re-emit it at infrared wavelengths. A distant observer will observe the light coming from different dust clouds along the thin ring at different points in time, due to the different path lengths of the clouds to the observer. All photons reaching the observer with a fixed delay τ with respect to the arrival of the AD outburst at the observer's location, lie along a so-called "isodelay surface" corresponding to

$$\tau = \frac{(1+\cos\theta)R_{\rm dust}}{c}\,, \tag{1.8}$$

where θ is the angle with respect to the line-of-sight to the observer (see Fig. 1.7).

As a function of time delay τ, the dust response can be written as

$$\Psi(\tau) = 2\pi\xi R_{\rm dust} {\rm d}\tau\,. \tag{1.9}$$

$\Psi(\tau)$ is called the "transfer function", describing the dust response to a δ-function continuum outburst, and ξ is the responsivity per unit area of the dust shell. For a thin spherical shell, the transfer function is constant for $0 \leq \tau \leq 2R_{\rm dust}/c$ (i.e., $\pi \geq \theta \geq 0$) and can be described by a top-head function.

For the reverberation approach to be valid, the light-travel time $t_{\rm LT} \approx R_{\rm dust}/c$ across the torus needs to be the dominant timescale (Peterson, 1997). This is ensured as the dynamical timescale $t_{\rm dyn}$ for substantial changes in the torus geometry is significantly longer than $t_{\rm LT}$

[6] In reality, the dusty torus is better approximated by a series of thin toroidal layers. However, with the thin spherical shell, one can most generally and most easily demonstrate the basic idea of the reverberation method.

($t_{\rm dyn} \approx R_{\rm dust}/v$, v on the order of $0.01c$), and because heating and cooling timescales are instantaneous compared to $t_{\rm LT}$. The dust is mainly heated by absorption of short wavelength radiation, with typical time scales of 10^{-6}s, whereas the cooling happens via blackbody radiation, typically within seconds (Nenkova et al., 2008a).

In reality, at some fixed t, the observer measures radiation coming from all isodelay surfaces simultaneously, and the observed dust flux $F(t)$ at time t can be written as:

$$F(t) = \int \Psi(\tau) C(t-\tau) \mathrm{d}\tau \,. \tag{1.10}$$

In order to unambiguously reconstruct the transfer function from Eq. 1.10, high-quality data and a good temporal sampling are needed. However, with few data or data of lesser quality, it is still possible to measure the location of the hot dust by a cross-correlation analysis of the driving and the responding light-curves. The hot dust radius is then given by $R_{\rm dust} = \tau \cdot c$, where τ is the time lag that maximizes the cross-correlation function (CCF):

$$CCF(\tau) = \int F(t) C(t-\tau) \mathrm{d}t \,. \tag{1.11}$$

In practice, the majority of dust reverberation measurements deal with the determination of the dust reverberation lag. This is mostly achieved by determining the peak or centroid of the CCF between the AD and the dust signals. In the SEDs of type 1 AGNs, an inflection point between AD emission dominating at UV/optical wavelengths and the host dust emission dominating at NIR wavelengths is generally reported around $\lambda = 1\mu$m (Ward et al., 1987; Riffel et al., 2009). Therefore, it is common to use the flux in an optical photometric passband to represent the AD emission, whereas the hot dust emission is given by the measured flux in a NIR passband, generally corrected for the remaining AD contribution in that passband. Recently, Hönig (2014) proposed that even exclusively optical photometric data, e.g. from large optical surveys, can be used to determine the reverberation lag. The idea of this method is to recover the Wien tail of the hot dust emission, which reaches into the optical wavelength regime, using high-quality photometric data (errors $< 1\%$).

1.3.4 The radius-luminosity relation

Sample of AGNs

The radius of the obscuring dust torus has been measured for many type 1 and type 2 AGNs, using mid-infrared or NIR interferometry, or dust reverberation (mostly V to K). A strong correlation with the intrinsic luminosity of the central source has been found, according to the relation:

$$R_{\rm dust} \propto \sqrt{L_{\rm AD}} \,, \tag{1.12}$$

or equally,

$$\tau \propto \sqrt{L_{\rm AD}}, \tag{1.13}$$

where τ is the reverberation delay of the dust. Such behavior is expected due to the inverse square law for the flux incident at the dust location $F_{\rm AD} = L_{\rm AD}/(4\pi R^2_{\rm dust})$, in a model in which the dust temperature and the inner radius of the dust torus are determined by radiation equilibrium and sublimation of dust. A quantitative estimation of the inner radius of the dust torus was performed by Barvainis (1987), taking into account the wavelength-dependent absorption efficiency of dust grains. This approach was extended by Kishimoto et al. (2007) to account for dependencies on the dust grain size as well. The inner dust radius can be estimated by:

$$R_{\rm dust} = 1.3 \left(\frac{L_{\rm UV}}{10^{46}{\rm erg/s}}\right)^{1/2} \left(\frac{T_{\rm sub}}{1500{\rm K}}\right)^{-2.8} \left(\frac{a}{0.05\mu{\rm m}}\right)^{-1/2} {\rm pc}\,, \tag{1.14}$$

with $L_{\rm UV}$ being the UV luminosity of the AD, $T_{\rm sub}$ the sublimation temperature of dust, and a the dust grain size. Assuming $T_{\rm sub} = 1500$ K, and $a = 0.05\mu$m, Kishimoto et al. (2007) found the radii obtained with dust reverberation to be systematically roughly a factor of 3 higher than expected by Eq. 1.14. This discrepancy might be caused either by a higher sublimation temperature, or a larger dust grain size. In a clumpy dust torus model proposed by Kawaguchi & Mori (2010), an anisotropically emitting AD is assumed. As a consequence, dust clouds on the equatorial plane can survive closer to the AD than the expected sublimation radius in models assuming isotropic illumination, which might also resolve the observed differences.

Despite the discrepancy between different models and estimates on the absolute size of the inner dust radius, a strong correlation between AD luminosity and dust radius as expected according to Eq. 1.12 has been confirmed for a sample of AGNs (see Fig. 1.8). Depending on the method of observations (i.e., interferometry versus reverberation), the wavebands used (mid-infrared versus NIR interferometry, V- to K-band reverberation versus multi-wavelengths reverberation), different locations within resp. components of the torus are resolved, so different constants of proportionality for this relation are found. For the warm dust around a sample of 13 type 1 and type 2 AGNs, Tristram et al. (2009) found a strong correlation between the dust radius $R_{\rm dust}$ (in parsecs) and the mid-IR luminosity at $\lambda = 12\mu$m according to $R_{dust;12\mu{\rm m}} = p_{12\mu{\rm m}} \cdot \sqrt{L_{12\mu{\rm m}}}$, with $p_{12\mu{\rm m}} = (1.8 \pm 0.3) \cdot 10^{-18}$pc W$^{-0.5}$. For the NIR hot dust, a relation according to Eq. 1.12 using K-band interferometric observations was confirmed e.g. by Kishimoto et al. (2013), and with reverberation measurements by Minezaki et al. (2004), Suganuma et al. (2006), Koshida et al. (2009), and Koshida et al. (2014). Prior to observing such relations for the dusty torus, similar relations have been established for the BLR as well (see e.g. Kaspi et al. (2005)).

Interferometrically inferred K-band dust radii are on average roughly a factor of 2 larger than radii from K-band reverberation campaigns (Kishimoto et al., 2013; Koshida et al., 2014). This reflects the difference between the two methods: whereas interferometric ring radii rather represent brightness-weighted effective radii, reverberation measurements generally emphasize the smaller responding radii, as the position of the peak of the CCF is most sensitive to material at those radii (Koratkar & Gaskell, 1991). Therefore, reverbera-

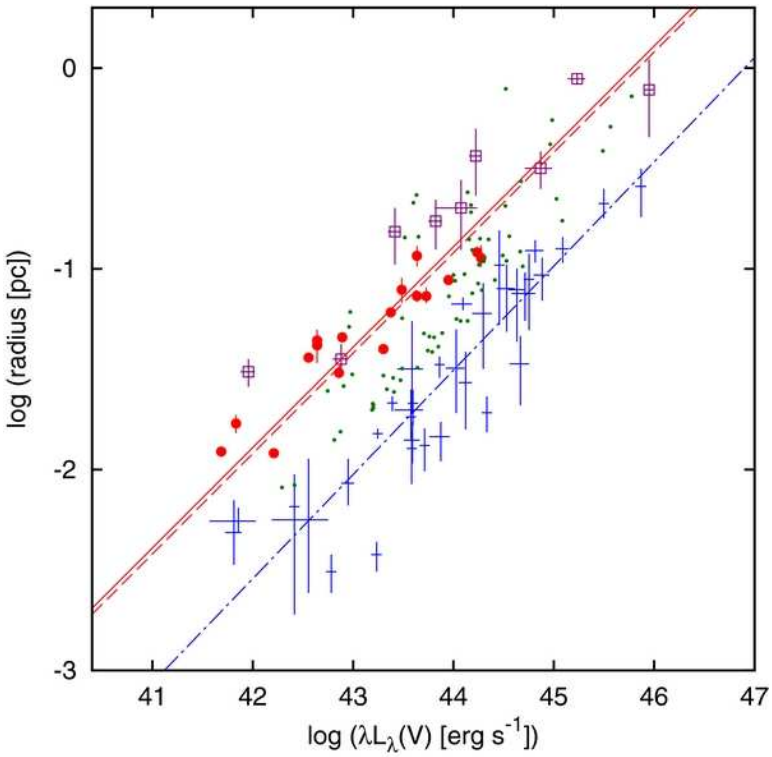

Figure 1.8: *The size-luminosity relation for a sample of AGNs as published by Koshida et al. (2014), showing the systematic offsets between the relation for K-band interferometry (purple squares) versus K-band reverberation (red circles) versus the relation for the BLR (blue). Overplotted is the expected radius for the very hot graphite-only dust clouds (green dots) as modeled by Mor & Netzer (2012).*

tion radii are generally more suitable to represent the radius closer to the inner boundary of the dust distribution (Koshida et al., 2014).

The size-luminosity relation for single targets

Whereas samples of AGNs seem to generally follow the expected relation given by Eq. 1.12, multiple observations of single targets yield contradictory results. Such inconsistencies are seen, for instance, in the radius measurements for the Seyfert 1 galaxy NGC 4151, obtained from *K*-band reverberation studies and *K*-band interferometry. Some data points seem to reflect the expectation that the hot dust radius grows as a consequence of increased AD luminosity (Oknyanskij et al., 1999), and decreases following dim AD times. There are, however, also periods in which the dust radius remains constant despite significant variations in the AD radiation (Pott et al., 2010). Furthermore, for the period 2001-2006, Koshida et al. (2009) observed substantial changes in the hot dust radius, but not at all according to the relation described by Eq. 1.12. The overall decrease in the dust radius seen by Koshida et al. (2009) seems to follow a decline observed in the AD flux a few years before (see Fig. 1.9). In contrast, a re-analysis of these same data by Hönig & Kishimoto (2011), using a radiative

transfer clumpy torus model, seems to favor a constant radius within the observed period.

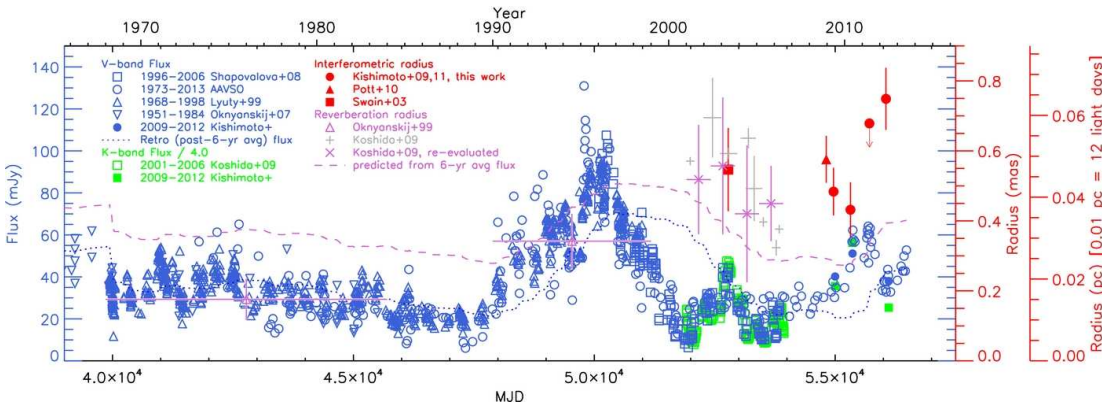

Figure 1.9: *V-band photometry (blue symbols) and hot dust radii for NGC 4151, derived with interferometry (red symbols) and reverberation techniques (purple and gray symbols), as presented in Kishimoto et al. (2013).*

A compilation of historical K-band radius measurements for NGC 4151 has been published by Kishimoto et al. (2013) and is shown in Fig. 1.9. The authors investigate the correlation of the hot dust radius with the instantaneous V-band flux of the central engine, and alternatively, with the flux averaged over some past timescale $\mathcal{T}_{\rm retro}$, separately for the reverberation and interferometric measurements. The averaging timescale $\mathcal{T}_{\rm retro}$ is supposed to represent a mean of the timescales for dust sublimation and dust reformation, with the latter being presumably substantially longer than the former. A correlation with the instantaneous V-band flux is not measured by Kishimoto et al. (2013). However, they find that the interferometrically obtained radii correlate best with the retro flux averaged over the past 6 years, whereas a correlation for the reverberation radii is only seen at longer values ($\mathcal{T}_{\rm retro} \approx 9$ years). A re-analysis of these data is performed in Sect. 5.3.4, putting this finding into question.

As for NGC 4151, changes in the hot dust radius have also been observed for other targets (Koshida et al., 2014), showing a non-trivial dependency on the AD luminosity.

The intrinsic scatter in the radius-luminosity relation

A substantial intrinsic scatter of on average roughly 35 percent (0.13 dex) are found for the size-luminosity relation (Eq.1.12) for AGN samples. A part of this scatter can be explained by differences in internal extinction (0.04 dex, (Koshida et al., 2014)). In the anisotropic radiation model (see 1.3.4) proposed by Kawaguchi & Mori (2010), the dust lag increases with the viewing angle of the dust torus, suggesting that the difference in inclination might contribute substantially to the observed scatter in the size-luminosity relation. Systematic changes in the size-luminosity correlation with the subclass of the Seyfert type (i.e., viewing angle), and further with the Eddington ratio, were searched for by Koshida et al. (2014),

but could not be confirmed. A substantial part of the scatter seems to be caused by a delayed response of changes in the dust radii to AD flux variations (0.11 dex), i.e., by non-trivial variations in the dust location with the luminosity of the central engine due to dust sublimation and reformation, as described above for the case of NGC 4151.

1.3.5 Where does the dust come from?

The origin of dust in AGNs is still an open issue. Self-consistent AGN torus models (Krolik & Begelman, 1988; Schartmann et al., 2010) assume that dust is ejected into the interstellar medium by asymptotic giant branch (AGB) stars or Supernovae (SN), and brought from outside to the central nuclear region.
In the early universe, however, high-redshift quasars are found, containing massive amounts of dust that are difficult, though not impossible, to explain by the SN and AGB scenarios (Dwek & Cherchneff, 2011). Therefore, other alternatives were searched for.
An intrinsic dust formation scenario has been proposed and discussed by Elvis et al. (2002) and Maiolino et al. (2006). Here, the dust formation results from BLR clouds that are assumed to be part of an outflowing AD wind[7]. In the course of a subsequent expansion and cooling process, the conditions of dust condensation are fulfilled and dust is formed, by the AGN itself. In this scenario, the clumpiness of the dust tours could naturally be explained, with the arrangement in clouds being simply inherited from the BLR distribution.

[7] It is not well-understood yet (Peterson & Horne, 2006) if the BLR clouds are infalling, outflowing or in rotation. Recent observations indicate that the signatures of low-ionization broad emission lines are consistent with gas that is infalling or in a rotating Keplerian disk (Grier et al., 2013; Peterson & Horne, 2006), whereas the higher ionized lines seem to trace gas that is part of an outflowing AD wind (Crenshaw et al., 1999; Peterson, 2006; Kollatschny & Zetzl, 2013).

2 Multi-wavelength hot dust reverberation

The methods developed within the three projects of this thesis, as well as the techniques used and implemented, are presented in this Chapter.

Throughout the following Chapters, these conventions will be used:

- The notation t always refers to the date of observation (given here as MJD). To emphasize specific points in time hereof, these will be indexed (e.g. $t_0, t_{\mathrm{start}}, t_{\mathrm{end}}$).
- The notation τ always denotes the hot dust reverberation delay (given here in days), such that $c \cdot \tau$ represents the corresponding hot dust radius R_{dust} (in light-days). Generally, $\tau = \tau(t)$ may evolve over time, if not stated otherwise. Distinguished values of τ at some specific observation date t are abbreviated by adopting the corresponding index from t, e.g. $\tau(t_0) = \tau_0$.
- Timescales will be referred to by the notation $\mathscr{T}$.

2.1 Single-epoch approach

The idea of the single-epoch approach is as follows: as described in Sect. 1.3.3, the circumnuclear dust absorbs the radiation coming from the central source and re-emits it in the infrared, with a characteristic lag time $\tau = R_{\mathrm{dust}}/c$. The dust emission can be approximated by the blackbody function

$$\mathrm{BB}(C_2, \lambda, T) = C_2 \cdot \frac{2hc^2}{\lambda^5} \frac{1}{\mathrm{e}^{hc/\lambda k_{\mathrm{B}} T} - 1}\,, \tag{2.1}$$

with T being the blackbody temperature of the hot dust and C_2 the blackbody constant (consisting of a mixture of emissivity, solid angle, and surface filling factor). The notation k_{B} refers to the Boltzmann constant.

By monitoring the hot dust signal as it responds to the AD signal, the reverberation lag time can be determined. Additionally, by decomposing the observed SEDs into a hot dust and an AD contribution, the evolution of the hot dust temperature and blackbody constant can be analyzed, in order to measure the radial dust distribution and to infer whether or not the hot dust is close to sublimation.

Specifically, it is important to perform such an analysis not only for one epoch, but for a multi-epoch data set. The dust sublimation temperature depends strongly on the assumed

dust species, composition and grain sizes, all of which might change significantly with radial distance from the source. Without detailed knowledge on these dust properties, it is not possible to determine if the innermost dust is close to sublimation from measuring the dust temperature in one single epoch. However, monitoring the hot dust temperature for an extended period allows to draw more reliable conclusions on the immediate dust state, since then – following an increased AD emission – it is possible to discriminate between a constant temperature (in case of sublimation) and rising temperatures (in case of no sublimation).

To be able to apply this method, nuclear light-curves are obtained, with the procedures described in Sects. 2.3.3 and 2.3.4, covering wavelengths regimes that are characteristic of the AD and dust components that should be separated. An inflection point between the two contributions is located around $\lambda = 1\mu$m (Kobayashi et al., 1993; Riffel et al., 2009), and increasing dust emission and decreasing AD contribution is found with increasing wavelength. While fluxes shortward of this inflection point can be used as a proxy for the AD radiation, the hot dust contribution is typically dominant around $\lambda = 2\mu$m. A sufficiently good wavelength coverage enables an unambiguous decomposition of the total nuclear AGN fluxes according to a two-component model – a power-law representing the AD emission, plus a blackbody function describing the hot dust emission:

$$F_\lambda(\lambda, \mathbf{x}) = \widetilde{C}_1 \cdot \lambda^{-\alpha} + C_2 \cdot \frac{2hc^2}{\lambda^5} \frac{1}{e^{hc/\lambda k_B T} - 1}\,. \tag{2.2}$$

The free parameters of this model are given by the hot dust blackbody constant C_2, the hot dust blackbody temperature T, the AD power-law index α and the AD proportionality constant $\widetilde{C}_1$, which are comprised in the vector $\mathbf{x}$ of model parameters. Results from this approach are presented in the Chapters 3 - 4.

2.2 Multi-epoch approach

2.2.1 Standard model without dust sublimation

To decrease the extreme degeneracies shown by the single-epoch approach, and to make use of all data for one target simultaneously, a multi-epoch model was developed and implemented in the second project of this thesis. The multi-epoch multi-wavelength model is given by:

$$F_\lambda(\lambda, t, \mathbf{x}) = C_1 \cdot F_{\rm opt}(t) \cdot \lambda^{-\alpha} + \mathrm{BB}(C_2, \lambda, T(\nu \cdot F_{\rm opt}(t - \tau)))\,, \tag{2.3}$$

Here, $\mathbf{x}$ denotes the complete vector of model parameters, and $F_{\rm opt}$ refers to the flux in the shortest wavelength passband used (which is the z band for the Omega 2000 data presented in Chapter 4, and the g' band for the GROND data of Chapter 5). The first term on the right

of Eq. 2.3 refers to the AD emission, usually described as a power-law in terms of λ, with power-law index α which is assumed to not change significantly over the observed flux range. For completeness, however, a varying α is also used in an alternative fit, and its influence on the results is tested, see Sect. 4.4.2 and Sect. 4.5.3. C_1 is a proportionality constant. In the second term on the right of Eq. 2.3, BB(.) denotes the blackbody function described by Eq. 2.1. It is assumed in Eq. 2.3 that the AD signal has the shape of the interpolated z-band signal (Omega 2000) resp. g'-band signal (GROND), which is justified as the emission shortward of $\lambda = 1\mu$m is dominated by AD emission (Kobayashi et al., 1993; Riffel et al., 2009). Starting from an initial temperature T_0, the blackbody temperature T evolves by construction, for $t > \tau$, in response to the AD variations as

$$\mathrm{d}T(t)/T(t) = \nu \cdot \frac{1}{4} \cdot \mathrm{d}L_{\mathrm{opt}}(t-\tau)/L_{\mathrm{opt}}(t-\tau)\,. \tag{2.4}$$

In this model, $\tau \neq \tau(t)$, i.e., τ does not evolve over time, but the inferred best-fit value of this parameter is taken to represent the whole data set or subset that is to be fit by the model. The variability factor ν accounts for the fact that not necessarily the complete z-band or g'-band variability might be reprocessed by the hot dust (Hönig & Kishimoto, 2011), which would lead to values of $\nu < 1$. Furthermore, values of $\nu \neq 1$, might indicate that the variability of the heating signal is underestimated or overestimated by the z-band resp. g'-band variability. The hot dust around AGNs is heated mainly by the UV part of the AD radiation. The z-band resp. g'-band flux is taken as a proxy for this UV heating, however the actual UV radiation is probably even more variable. The full parameter vector comprises $\mathbf{x} = (C_1, \alpha, C_2, T_0, \tau, \nu)$.

The temperature evolution described by Eq. 2.4 used in this multi-epoch approach can be derived (in the blackbody limit, with absorption efficiency $Q_{\mathrm{abs}} = 1$) from the Stefan-Boltzmann law. It is further confirmed by the measured hot dust temperature evolution of NGC 4151, obtained from single-epoch SED fits, as described by the approach from Sect. 2.1. These single-epoch have successfully been performed for each epoch of the complete NGC 4151 2010-2014 data set (Omega 2000), prior to applying the multi-epoch approach described by Eq. 2.3-2.4. As can be seen in Fig. 4.6, the blackbody temperature obtained from the single-epoch SED fits closely tracks the AD signal, with a stable delay of roughly 30 days, and the temperature variation is significant.

Compared to Eq. 2.2, in this multi-epoch approach the data are temporally connected. Using the temperature evolution described by Eq. 2.4 drastically reduces the number of parameters of the multi-epoch fit, as one only needs to estimate the initial blackbody temperature T_0 instead of a temperature for each single epoch. This makes the algorithm more robust against extreme degeneracies between T and C_2.

Only for the case of NGC 4151, an additional model was used within the standard approach: To check if the distribution of the innermost hot dust is rather compact or, in contrast, substantially radially extended (as conjectured in the analysis of Sect. 3), the

possibility of a further blackbody component contributing to the hot dust signal is tested. Therefore, an alternative 2BB-model of similar type is fit to the NGC 4151 data:

$$\begin{aligned} F_\lambda(\lambda,t,\mathbf{x}) &= C_1\cdot F_{\rm opt}(t)\cdot\lambda^{-\alpha}+\mathrm{BB1}(C_2,\lambda,T_1(\nu_1\cdot F_{\rm opt}(t-\tau_1))) \\ &\quad +\mathrm{BB2}(C_3,\lambda,T_2(\nu_2\cdot F_{\rm opt}(t-\tau_2)))\,, \end{aligned} \tag{2.5}$$

with the temperature evolution of the second blackbody given by an expression as in Eq. 2.4, though with different starting temperature, time lag, and variability factor. This 2BB-model has four additional parameters, and $\mathbf{x}=(C_1,\alpha,C_2,T_{0,1},\tau_1,\nu_1,C_3,T_{0,2},\tau_2,\nu_2)$.

Here, to explicitly discriminate between the two blackbody components, the notations τ_1 versus τ_2, as well as $T_{0,1}$ versus $T_{0,2}$ and ν_1 versus ν_2 are used.

2.2.2 Model including dust sublimation

To my knowledge, dust sublimation events have not yet been incorporated in any published dust reverberation model. However, in a model as described in Sect. 1.3.4, with the dust radius generally being expected at the sublimation radius, dust sublimation is an inevitable consequence whenever the dust radius falls within the sublimation radius for a period significantly longer than the sublimation timescale. Therefore, a first, heuristic approach to model the sublimation process in AGN dust tori has been made within this thesis.

As an alternative to Eq. 2.3, where the hot dust signal is merely a reprocessing of the AD signal, a model allowing for sublimation of hot dust was developed and implemented. Such a model is motivated by the first period of the NGC 3227 data set presented in Chapter 5, i.e., the epochs 1-7, where the NIR response of the hot dust apparently deviates from what one would expect if the dust signal were just a delayed and smoothed-out version of the AD signal (see Sect. 5.3.4). A sketch of this sublimation model is shown in Fig. 2.1.

For a clumpy dust torus, i.e., a distribution of dust clouds with substantial time gaps in between, the following behavior is expected during sublimation:

- a temporary, short-term decrease in the irradiated dust surface, and hence C_2 (due to sublimation of innermost dust clouds at $R_{\rm sub}$ or substantial parts of these),
- a constant dust temperature, since the dust cannot be heated to temperatures exceeding the sublimation temperature
- an increase in the hot dust reverberation delay τ, as a consequence of the destruction of innermost clouds,
- a delayed re-increase in the irradiated dust surface, and hence C_2, when successive clouds (that were shielded before by the innermost clouds) are reached by the AD radiation. This delay is given by the inter-cloud-delay $\tau_{\rm cl}=d_{\rm cl}/c$, where $d_{\rm cl}$ is the mean radial distance between the clouds at the inner edge of the torus.

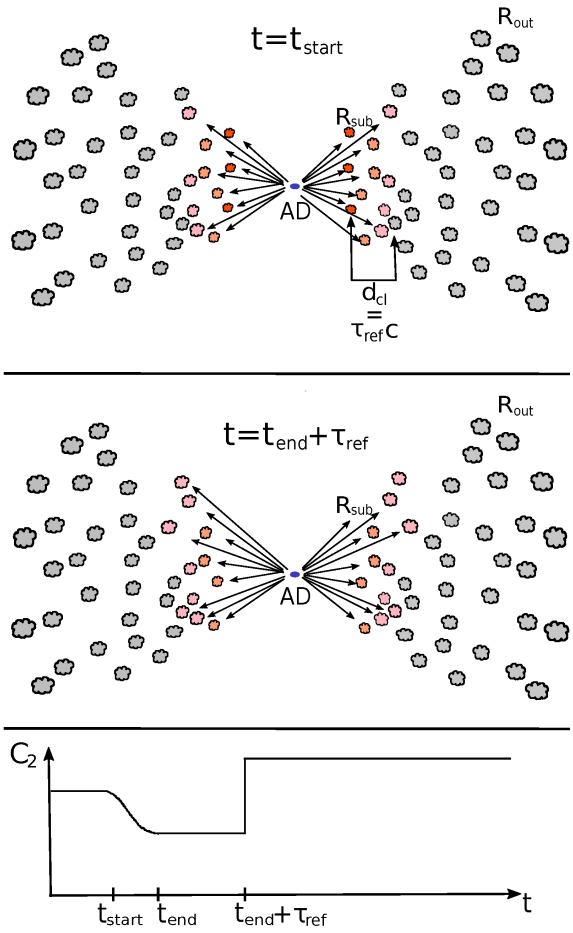

Figure 2.1: *A qualitative sketch of the presented sublimation model. Top panel shows the hot dust distribution before a sublimation event. In the central panel, it is illustrated that after a sublimation event, the hot dust surface is re-illuminated by heating a different set of clouds at slightly larger radii. The bottom panel depicts qualitatively the time evolution of C_2 before, during and after a sublimation event.*

Specifically, it is expectable that this re-increase of C_2 will not happen immediately after the sublimation, as suggested by a rough estimation of $\tau_{\rm cl} \lesssim 1\tau_{\rm sub}$ (see Sect. 5.3.4).
In contrast to the process of reformation, the re-increase of C_2 describes a "re-illumination" of dust, i.e., the flux level is recovered merely due to the contribution of clouds that were shielded before. No dust is reformed here. The amount of this re-increase of C_2 depends on the radial dust distribution. In contrast, a real reformation of dust at the initial sublimation radius after decreasing incident AD flux is only expected on longer timescales ($>$ 6 years, as found by Kishimoto et al. (2013); also see Sect. 5.3.4), and not part of this model. In the following, the term "re-illumination" will be used for the re-increase of C_2.

The sublimation model is given by:

$$F_\lambda(\lambda, t, \mathbf{x}) = C_1 \cdot F_{\rm opt}(t) \cdot \lambda^{-\alpha} + {\rm BB}(C_2(t), \lambda, T(\nu \cdot F_{\rm opt}(t - \tau(t)))), \tag{2.6}$$

where now the parameters C_2 and τ are allowed to evolve over time. The model is separated into two phases: the sublimation phase and the re-illumination phase.

Sublimation phase

The evolution of C_2 during the dust sublimation process is derived for the model as follows: without dust sublimation, the equilibrium temperature of a dust grain is given by the energy balance between the absorption rate of radiation received from the AD and the emission rate of thermal radiation from the dust particle (see e.g. Hönig & Kishimoto (2011)):

$$L_{\rm rec} = L_{\rm em}, \tag{2.7}$$

or

$$\int \frac{L_\nu}{4\pi R_{\rm dust}^2} Q_{{\rm abs};\nu}\, \pi a^2 {\rm d}\nu = \int 4\pi a^2 Q_{{\rm abs};\nu}\, \pi B_\nu(T) {\rm d}\nu = 4\pi a^2 Q_{{\rm abs};P}(T)\, \sigma_{\rm SB}\, T^4, \tag{2.8}$$

where $R_{\rm dust}$ denotes the distance of the dust from the AD, a the radius of the dust particle assumed to be spherical, and $Q_{{\rm abs};P}(T)\,\sigma_{\rm SB}\,T^4 := \int Q_{{\rm abs};\nu}\pi B_\nu(T){\rm d}\nu$ is the Planck mean absorption efficiency.

In case of dust sublimation, another term enters the right-hand side of Eq. 2.7, and the equilibrium temperature of the grain is now calculated by the energy balance between the absorption rate of AD radiation and the emission rate of thermal radiation from the dust particle plus the sublimating dust mass (see e.g. Kimura et al. (2002)):

$$L_{\rm rec} = L_{\rm em;sub} - \frac{{\rm d}m}{{\rm d}t}\mathscr{L}, \tag{2.9}$$

where $\mathscr{L}$ is the latent heat of sublimation (see e.g.Kimura et al. (2002) for values of this constant for some dust species). For the non-sublimation case, $L_{\rm rec} = L_{\rm em}$, so one can replace $L_{\rm rec}$ in Eq. 2.9 by $L_{\rm em} = L_{\rm em;nosub}$, i.e. by the thermal radiation from the particle if sublimation would not be accounted for and the temperature of the dust grain could go beyond the sublimation temperature $T_{\rm sub}$. Equation 2.9 can be then re-written:

$$\left|\frac{{\rm d}m}{{\rm d}t}\right| \mathscr{L} = L_{\rm em;nosub} - L_{\rm em;sub} = 4\pi a^2 \sigma_{\rm SB} \left(Q_{{\rm abs};P}(T_{\rm nosub}) T_{\rm nosub}^4 - Q_{{\rm abs};P}(T_{\rm sub}) T_{\rm sub}^4\right). \tag{2.10}$$

In the blackbody limit ($Q_{{\rm abs};P}$=1, ${\rm d}Q_{{\rm abs};P}/{\rm d}T$=0), one gets

$$\left|\frac{{\rm d}m}{{\rm d}t}\right| \mathscr{L} = 4\pi a^2 \sigma_{\rm SB}\, Q_{{\rm abs};P} \left(T_{\rm nosub}(t)^4 - T_{\rm sub}^4\right). \tag{2.11}$$

During any time t in the sublimation phase, the decrease of the (macroscopic) dust volume V in a small time interval (0.1 day sampling in this model) will be proportional to the (microscopic) sublimated mass in that time interval, so the illuminated dust surface and hence the blackbody constant $C_2 \propto V^{2/3}$ will evolve according to:

$$\mathrm{d}C_2(t) = -C_3 \cdot \left(T_{\mathrm{nosub}}(t)^4 - T_{\mathrm{sub}}^4\right)^{2/3} \cdot C_2(t_0)\,. \tag{2.12}$$

Thus, once the temperature $T(t)$ reaches the sublimation temperature $T_{\mathrm{sub}} = T(t_{\mathrm{start}})$, at time t_{start}, the blackbody constant C_2 decreases according to Eq. 2.12. Here, the term $T_{\mathrm{nosub}}(t)^4 - T_{\mathrm{sub}}^4$ relates to the excess AD energy, and C_2 decreases proportionally to it. In the following, $C_2(t_0)$ will be denoted as $C_{2,0}$.

Furthermore, the hot dust temperature is set to $T(t > t_{\mathrm{start}}) = \mathrm{const.} = T_{\mathrm{sub}}$ during the sublimation phase. At the end of the sublimation phase, marked by $t = t_{\mathrm{end}}$, the reverberation delay is set to $\tau(t_{\mathrm{end}}) = \tau_{\mathrm{end}} = \tau_{\mathrm{max}}$, as determined by the maximum accretion disk illumination level L_{max} (maximum g'-band flux) reached during the sublimation event:

$$\tau_{\mathrm{max}} = \tau_0 \cdot \sqrt{\frac{L_{\mathrm{max}}}{L(t_{\mathrm{start}} - \tau_0)}}\,. \tag{2.13}$$

Re-illumination phase

In the re-illumination phase, the blackbody constant C_2 starts to reform as soon as successive clouds are reached by the AD radiation. The functional form of the temporal evolution of C_2 in the re-illumination phase is restricted in this model to the simplest (though unphysical) shape: after a delay $\mathscr{T}_{\mathrm{ref}}$ with respect to the end of the sublimation process (denoted by t_{end}), C_2 reforms instantaneously according to

$$C_2(t_{\mathrm{end}} + \mathscr{T}_{\mathrm{ref}}) = C_{2,0} \cdot \left(\frac{\tau_{\mathrm{end}}}{\tau_0}\right)^{2+\beta}\,, \tag{2.14}$$

Eq. 2.14 describes how the C_2 evolution depends on $\tau_{\mathrm{end}}/\tau_0$ as well as on the assumed radial dust distribution represented by the exponent.

Equation 2.14 was derived for this model as follows: At any radius $r = \mathrm{const.}$, the illuminated dust surface is given by

$$S = \int \eta(r,\phi,z)\mathrm{d}V \qquad ,r = \mathrm{const.} \tag{2.15}$$

$$= \int\int \eta_r \eta_z r \mathrm{d}\phi \mathrm{d}z\,. \tag{2.16}$$

Inserting η_r and η_z, as defined in Eqs. 1.3 and 1.5 (Hönig & Kishimoto, 2010), into Eq. 2.16 yields

$$S = 2\pi r \eta_r \int \exp\left(\frac{-z^2}{2H^2}\right)\mathrm{d}z$$

$$= \sqrt{8\pi^3} h \eta_r r^2\,. \tag{2.17}$$

During the sublimation phase, the average radius of dust contributing to the NIR signal increases from τ_0 at the beginning of the sublimation process to $\tau_{\rm end}$ at the end of the sublimation process, thus the illuminated dust surface (and hence C_2) will increase roughly as $\left(\frac{\tau_{\rm end}}{\tau_0}\right)^{2+\beta}$ as soon as subsequent dust clouds are reached, leading to Eq. 2.14.

The vector of parameters for this model is thus $\mathbf{x} = (C_1, C_{2,0}, T_0, \tau_0, \alpha, \nu, T_{\rm sub}, C_3, \mathscr{T}_{\rm ref}, C_4)$, i.e., the sublimation model has four parameters more than the standard model. Depending on the used data set, it might be advisable to fix part of the parameters, in order to avoid degeneracies, as was also done for the analysis of NGC 3227 presented in Chapter 5.

Whereas in the standard model, the notation τ_1 was used for the reverberation delay (to distinguish from the delay τ_2 of a potential second blackbody component), the sublimation model uses the notation τ_0 for the reverberation delay parameter, to explicitly refer to the initial delay at $t = 0$.

2.3 Optical and near-infrared photometry of variable sources

To analyze the response of the hot dust to varying AD emission, light-curves need to be recorded in the wavelengths regimes representing these components, with a temporal sampling determined for each object by the corresponding estimated variability timescale of the hot dust. In order to unambiguously distinguish between AD and hot dust emission in the model, multi-band NIR (and preferentially also optical) photometry is needed. While the measured flux in the short wavelength bands can be used as a proxy for the AD radiation, increasing dust emission and decreasing AD contribution is found with increasing wavelength. An inflection point between the two contributions is located around $\lambda = 1\mu$m. The K band is dominated by hot dust emission (Riffel et al., 2009).
The desired multi-epoch, multi-band photometry was obtained with the Omega 2000 camera for the analysis of the Seyfert 1 galaxy NGC 4151 (described in Chapters 3 and 4), and with the GROND camera for a sample of 23 AGNs (see Chapter 5). The two instruments are shortly described in Sect. 2.3.1.
The nuclear fluxes of the targets at various epochs and filters were extracted using one or both of the two approaches presented in Sects. 2.3.3 and 2.3.4, namely `GALFIT` and `ISIS`.

2.3.1 The Omega 2000 and GROND instruments

The Omega 2000 camera

Omega 2000 (Kovács et al., 2004) is a prime focus NIR wide-field camera mounted on the 3.5m telescope in Calar Alto, Spain[1]. Omega 2000 has a field of view $15.4' \times 15.4'$, and its 2048 × 2048 pixel HAWAII-2 detector has a scale of $0.45''$ pixel^{-1}. The target NGC 4151 was observed with Omega 2000, using the $zYJHK$ passbands. The transmission curves for

[1]Based on observations collected at the Centro Astronomico Hispano Aleman (CAHA), operated jointly by the Max-Planck Institut für Astronomie and the Instituto de Astrofisica de Andalucia (CSIC).

these filters are shown in Fig. 2.2.

In order to enable an appropriate sky subtraction in the data reduction (see Sect. 2.3.2), a manual dithering was realized in the observational setup, with the shape of a five-dice pattern. The offsets between the dither positions was chosen to be on the scale of the extent of the host galaxy of NGC 4151, such that no residual flux from the galaxy is present in the center of the constructed median sky image ((i.e., the dither step size was 3.0′)). In each observing night, the target was observed in each of these five dither positions in the $zYJHK$ passbands.

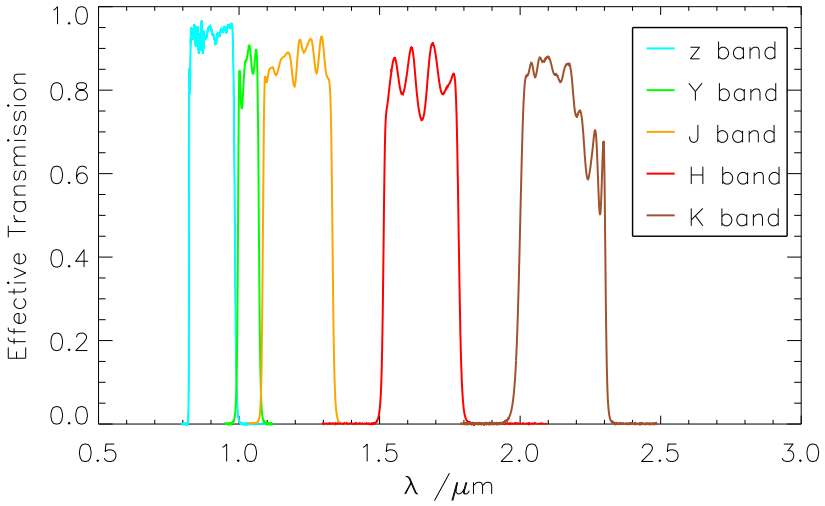

Figure 2.2: *Transmission in the Omega 2000 $zYJHK$ passbands.*

For absolute calibration of the AGN fluxes – derived with the methods presented in Sect. 2.3.3 and Sect. 2.3.4 – the known 2MASS[2] JHK magnitudes of calibration stars in the field of view (FoV) are used, after conversion into linear fluxes according to

$$F = F_0 \cdot 10^{-0.4m}, \tag{2.18}$$

where m is the magnitude of the star in a given passband. F_0 denotes the zero magnitude flux, i.e. the flux of a source with corresponding magnitude $m = 0$, and is given by $F_{0,J} = 1594 \pm 28$ Jy for the J band, $F_{0,H} = 1024 \pm 20$ Jy for the H band, and $F_{0,K} = 667 \pm 13$ Jy for the K band. For the z and Y calibration, a database containing model spectra of main sequence stars is used (kindly provided by R. van Boekel, priv. com.). For each reference

[2]This publication makes use of data products from the Two Micron All Sky Survey, which is a joint project of the University of Massachusetts and the Infrared Processing and Analysis Center/California Institute of Technology, funded by the National Aeronautics and Space Administration and the National Science Foundation.

star, the best-fit spectrum to the $BVJHK$ fluxes as listed by SIMBAD is determined. The zY photometry is then calculated from that spectrum.

The GROND camera

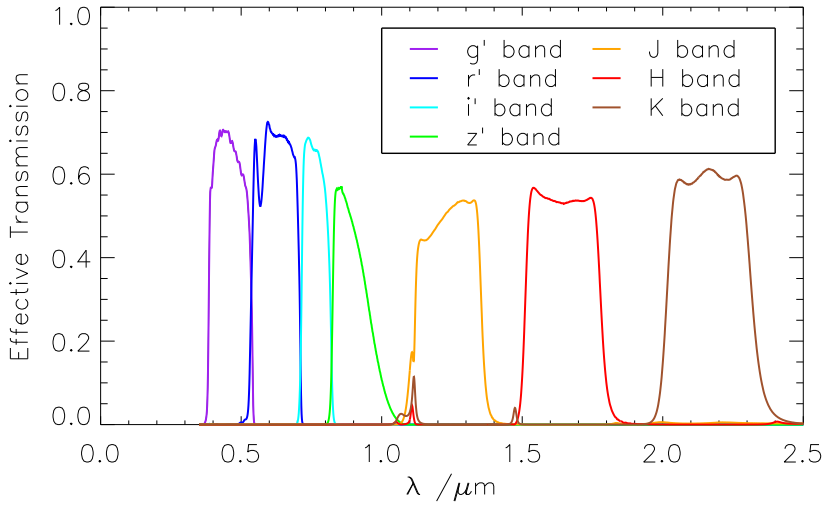

Figure 2.3: *Transmission in the GROND $g'r'i'z'JHK$ passbands.*

The Gamma-Ray Burst Optical and Near-Infrared Detector (GROND) (Greiner et al., 2008) is a 7-channel imager mounted on the MPG 2.2m telescope located at the ESO observatory in La Silla, Chile. GROND has been built by the high-energy group of the Max-Planck Institute for Extraterrestrial Physics (MPE) in Garching in collaboration with the Landessternwarte Tautenburg and the European Southern Observatory (ESO). The instrument is specifically designed for the observations of GRB afterglows. The main goal of GROND is a rapid determination of the redshift of observed GRB explosions, achieved by deriving a photometric redshift based on the Lyα break (Lamb & Reichart, 2000) with the simultaneous multi-band photometry. However, the simultaneous imaging capabilities of GROND in seven different photometric passbands make it ideal for observations of the spectral energy distribution in various variable astrophysical objects, e.g. AGNs. Thus, GROND is an optimal instrument for the hot dust reverberation campaign presented in this work. The seven GROND filters $(g', r', i', z', J, H, K)$ enable the distinction between variations in the AD and hot dust emission, as desired.

The GROND instrument performs separation of the different photometric bands using dichroics. The four optical 2048 × 2048 pixel detectors each have a field of view $5.4' \times 5.4'$, and a scale of $0.158''$ pixel^{-1}. With a focal reducer system, the field of view is adjusted to $10.0' \times 10.0'$ in the NIR part of GROND. The three NIR 1024 × 1024 pixel detectors each

have a scale of $0.6''$ pixel^{-1}. The GROND filter curves are shown in Fig. 2.3.

The observational setup was similar to the Omega 2000 setup, but with seven instead of five dither positions. In order to not have any significant residuals in the center of the constructed sky image, the dither steps were chosen to be on the order of the size of the target (i.e., up to $3.75'$). For very extended objects in the GROND FoV, this leads to the effect that some of the exposures do not include the target itself. The setup was changed in the course of this campaign: the dither steps were chosen as in the standard GROND observing blocks (i.e., $18''$), and separate sky exposures were taken for construction of the median sky image.

The nuclear fluxes obtained with the methods described in Sect. 2.3.3 and Sect. 2.3.4 are calibrated with the known SDSS[3] $g'r'i'z'$ and 2MASS JHK magnitudes of calibration stars in the FoV.

As the GROND i' passband is significantly narrower than the SDSS i' filter, conversion between the two passbands was performed according to the relation (Greiner, 2009):

$$i'_{\mathrm{SDSS}} - i'_{\mathrm{GROND}} = (-0.031 \pm 0.005) + (0.113 \pm 0.014) \cdot (r'_{\mathrm{SDSS}} - i'_{\mathrm{SDSS}}) \,. \tag{2.19}$$

The other passbands are found to be identical within the errors (Greiner, 2009), so no conversion relation is applied here. Conversion from magnitudes to linear fluxes is performed as for the case of Omega 2000 for the JHK passbands, and using

$$F = F_0 \cdot 10^{-0.4m} = 3631\mathrm{Jy} \cdot 10^{-0.4m} \tag{2.20}$$

for the $g'r'i'z'$ passbands, where magnitudes are intended to be (very close to) the AB magnitude system in which an object with $m = 0$ should have the same counts as a source of $F = 3631$ Jy. In the SDSS catalog, magnitudes are given as asinh magnitudes, defined by

$$m = -\frac{2.5}{\ln(10)} \cdot [\mathrm{asinh}((F/F_0)/(2b)) + \ln(b)] \,, \tag{2.21}$$

instead of the standard Pogson magnitudes:

$$m = -2.5 \log\left(\frac{F}{F_0}\right) . \tag{2.22}$$

[3] Funding for the SDSS and SDSS-II has been provided by the Alfred P. Sloan Foundation, the Participating Institutions, the National Science Foundation, the U.S. Department of Energy, the National Aeronautics and Space Administration, the Japanese Monbukagakusho, the Max Planck Society, and the Higher Education Funding Council for England. The SDSS Web Site is http://www.sdss.org/.
The SDSS is managed by the Astrophysical Research Consortium for the Participating Institutions. The Participating Institutions are the American Museum of Natural History, Astrophysical Institute Potsdam, University of Basel, University of Cambridge, Case Western Reserve University, University of Chicago, Drexel University, Fermilab, the Institute for Advanced Study, the Japan Participation Group, Johns Hopkins University, the Joint Institute for Nuclear Astrophysics, the Kavli Institute for Particle Astrophysics and Cosmology, the Korean Scientist Group, the Chinese Academy of Sciences (LAMOST), Los Alamos National Laboratory, the Max-Planck-Institute for Astronomy (MPIA), the Max-Planck-Institute for Astrophysics (MPA), New Mexico State University, Ohio State University, University of Pittsburgh, University of Portsmouth, Princeton University, the United States Naval Observatory, and the University of Washington.

Here, F_0 is the flux of an object with conventional Pogson magnitude of zero, and b is called the softening parameter. The asinh magnitudes are practically identical to the standard astronomical magnitude for high SNR measurements, but also behave reasonably at low SNR and even at negative values of flux, where the logarithm in the Pogson magnitude is not defined. Differences between Pogson and asinh magnitudes are less than 1% for an object with $F/F_0 \geq 10b \approx 10^{-9}$, which is the case for all objects considered in this work.

2.3.2 Data reduction

The raw images are reduced with pipelines developed by R. Decarli for the Omega 2000 data, and by R. Decarli and G. De Rosa (e.g. cited in Morganson et al. (2012)) for the GROND data, making use of `IRAF` [4] routines. These pipelines were modified and extended in the course of this work, to match the setup used in this project. After bias / dark subtraction and flat-fielding of each individual image, a scaled median sky image is subtracted from each frame. The median sky image is created by stacking individual dithered exposures without realignment. After sky subtraction, the individual images are realigned and combined.

2.3.3 GALFIT

From the final reduced science images, the AGN flux has to be determined in order to produce the light-curves as input for the models described in Sects. 2.1 and 2.2. When performing aperture photometry on the nucleus of an active galaxy, the flux in the aperture always contains a contribution from the host galaxy. Similarly, when extracting the AGN flux by fitting the point spread function (PSF) to the observed brightness distribution, the resulting light-curves will be altered by remaining host contributions. For multi-component objects, such as galaxies in general, or active galaxies with the additional point source component on top, precise photometry can be achieved with `GALFIT` (Peng et al., 2002), allowing for the simultaneous fitting of different galaxy components to the objects in an image.

Prior to the fit, the user has to specify in an input file the image region and the objects that should be fit by `GALFIT`, including by which model components each object should be described. Further, a PSF model has to be given to `GALFIT`. The PSF for each image in the present work has been constructed with the help of the `IRAF` DAOPHOT package.

During the fit, the algorithm convolves the model image with the given PSF and compares it to the empirical image, by minimizing the reduced χ^2, defined as:

$$\chi^2_{\mathrm{red}} = \frac{1}{N_{\mathrm{dof}}} \sum_{x=1}^{nx} \sum_{y=1}^{ny} \frac{(F_{x,y} - m_{x,y})^2}{\sigma^2_{x,y}} \tag{2.23}$$

[4] IRAF is distributed by the National Optical Astronomy Observatory, which is operated by the Association of Universities for Research in Astronomy, Inc., under cooperative agreement with the National Science Foundation.

using the Levenberg-Marquardt downhill-gradient method. The convolution is done by multiplying the Fourier transforms of the PSF and the models, and then inverse transform them, using a fast Fourier transform (FFT) algorithm. In Eq. 2.23, N_{dof} is the number of degrees of freedom of the fit, nx and ny the image dimensions, and $F_{x,y}$ denotes the flux at pixel (x, y). The flux error $\sigma_{x,y}$ is given by the Poisson error at each pixel. The model $m_{x,y}$ is given by the sum of the nf model functions $f_{i;x,y}$ that are determined by the model parameters $(\alpha_1, ..., \alpha_n)$:

$$m_{x,y} = \sum_{i=1}^{nf} f_{i;x,y}(\alpha_1, ..., \alpha_n)\,. \tag{2.24}$$

In `GALFIT`, varying observing conditions, leading to a varying seeing in the empirical image, are automatically accounted for by the convolution of the model with the PSF. The output best-fit model parameters thus correspond to the best-fit parameters of the "intrinsic" brightness distribution, meaning the brightness distribution without degradation by telescope optics or the atmosphere. Possible model components are, for instance:

- the PSF model for a point source (for instance, the AGN or calibration stars),
- a Sersic profile,
- an exponential disc profile.

The exponential disc profile has the functional form

$$\Sigma(r) = \Sigma_0 \exp\left(-r/R_{\mathrm{s}}\right)\,, \tag{2.25}$$

where R_{s} is the disc scale length, and Σ_0 the central surface brightness. The Sersic profile is given by

$$\Sigma(r) = \Sigma_{\mathrm{e}} \exp\left(-\kappa[(r/R_{\mathrm{e}})^{1/n} - 1]\right)\,, \tag{2.26}$$

where R_{e} denotes the effective radius, and Σ_{e} is the surface brightness at the effective radius. The Sersic index n is coupled to κ to ensure that always half of the flux falls within R_{e}. For $n = 0.5$, $\Sigma(r)$ represents a Gaussian profile, and for $n = 4$ the de Vaucouleurs profile, often used for describing classical galaxy bulges, is recovered.

One characteristic of the Sersic profile is that for high values of n, it gets very steep in the inner region and becomes very flat far from the center. Here, one has to pay attention in case of a PSF that fails to represent well the AGN at the center of the galaxy – caused, for instance, by saturation of the AGN (or of one of the stars that were used to construct the PSF), or by low-SNR stars used to construct the PSF of a bright nucleus. Such a PSF mismatch can lead to high n values, as `GALFIT` might try to model the nucleus by the steep inner Sersic profile, whose very flat outer parts then mimic the sky background. To avoid such behavior, the PSF must be constructed to represent the AGN as well as possible. In particular, the brightness of the stars used for PSF construction should be on the order of

the brightness of the AGN. When it is not possible to construct a sufficiently appropriate PSF for some epoch or target, particular care must be taken, and in some cases it can be useful to fix parameters, e.g. the sky level or n.

A variety of other possible galaxy components are proposed in Peng et al. (2002). However, since the aim of this analysis is not to derive the best-fit model of the host galaxy in all its details, but rather to obtain a reasonable estimate of the host contribution within the central region, the decomposition is here restricted to the few presented model functions.

2.3.4 ISIS

As an alternative to `GALFIT`, the `ISIS` image subtraction package (Alard & Lupton, 1998; Alard, 2000) can be used, which enables the precise measurement of flux variations in variable objects. Following the procedures described by Shappee & Stanek (2011), the images in each band are first aligned using the program Sexterp (Siverd et al., 2012). A reference image has to be chosen or constructed – in this work, the image with the best SNR and/or seeing is used. Then, a spatially variable convolution kernel K is determined that minimizes the discrepancy

$$D = \sum_i ([R \otimes K](x_i, y_i) - I(x_i, y_i))^2 \,, \tag{2.27}$$

i.e. the kernel optimally transforms the reference image R to the seeing and flux level of a given individual image I.

Each frame is then subtracted from the convolved reference image. Light curves, i.e. difference fluxes relative to the reference image, are then extracted from the subtracted images by performing aperture photometry on the residual nuclear flux. The error in the difference flux is estimated by measuring the residual flux of non-variable stars in the field (which should ideally be zero). Absolute calibration of the difference flux of each individual frame is performed with the same calibration stars as used in the `GALFIT` analysis for each target. The absolute nuclear flux level in the reference image is also adopted from the `GALFIT` results. A comparison of the two methods is shown in Fig. 4.1 for the K-band fluxes of NGC 4151. The `GALFIT` and `ISIS` fluxes agree well within the given errors.

For targets at substantially farther distance than NGC 4151 (as are present in the broad AGN sample analyzed in this work), a `GALFIT` decomposition might be more difficult due to increased degeneracies between PSF and bulge. Therefore, extracting the light-curves with `ISIS` should be preferred for distant objects. However, depending on the complexity of the convolution kernel, `ISIS` requires a minimum number of $N = ((n_\mathrm{d}+1)\times(n_\mathrm{d}+2))/2$ (with n_d the degree of spatial variations of the kernel) high-SNR non-variable stars in the field of view, preferentially with a brightness roughly on the order of the AGN. This criterion could not always be met for the GROND targets. For instance, high-SNR stars that are saturated, or variable stars, need to be masked, thereby decreasing the number of usable high-SNR stars. In the NIR, due to the nearly four times larger pixel scale and thus a poorly sampled

PSF, plus a PSF that varies over the detector (which affords $n_{\rm d} > 0$), using ISIS requires a much higher number of high SNR stars than in the optical, but the SNR is poorer. For part of the so far analyzed targets (see Sect. 5.4), the larger NIR FoV can compensate for the other effects resulting in a sufficient number of stars for the use of ISIS.

2.4 Interpolation of the input AD signal

The theoretical background for interpolation of the input signal to the multi-epoch model fit is presented in this Section. The interpolation makes use of a formalism proposed by Rybicki & Press (1992) and Press et al. (1992), which was implemented in this work using IDL routines.

To calculate the blackbody temperature T described by Eq. 2.4 for any arbitrary value of τ in the range of the data, one first needs to interpolate the input AD signal, which is represented by the z-band light-curve for the Omega 2000 data, and by the g'-band light-curve for the GROND data. This interpolation is done with the formalism for interpolation, realization and reconstruction of noisy irregularly sampled data by Rybicki & Press (1992), which has been previously used for reverberation studies of the BLR, e.g. by Zu et al. (2011) or Hernitschek et al. (2014). The AD signal can be described as a stochastic process characterized by two structure function parameters, which are estimated from the data. With this, the signal can be predicted for unmeasured times.

The M measurements $\mathbf{y} = \{y_i\}, i = 1, ..., M$ of the AD flux can be written as

$$\mathbf{y} = \mathbf{s} + \mathbf{E}\bar{y} + \mathbf{n}\,, \tag{2.28}$$

where $\mathbf{s}$ represents the intrinsic variability signal, $\mathbf{E}$ is the vector $(1, 1, 1..., 1)^T$, $\bar{y}$ is an appropriate estimator of the mean of the data, and $\mathbf{n}$ represents the measurement noise. The intrinsic signal $\mathbf{s}$ can be described as a stochastic process with a certain correlation structure, and an estimate $\hat{s_*}$ of the signal can be calculated at any (measured or unmeasured) point using the M already obtained measurements:

$$\hat{s_*} = \hat{\mathbf{d}}_*^T(\mathbf{y} - \mathbf{E}\bar{y}) + x_*\,. \tag{2.29}$$

Here, $\hat{\mathbf{d}}_*$ are linear coefficients that depend on the particular point to be estimated, and x_* is the discrepancy between the estimated and the true value. Minimizing the discrepancy with respect to the linear coefficients yields then the solution for the coefficients, and the least variance estimate of the signal

$$\hat{s_*} = \mathbf{S}_*^T[\mathbf{S} + \mathbf{N}]^{-1}(\mathbf{y} - \mathbf{E}\bar{y}) + \bar{y}\,. \tag{2.30}$$

Here, $\mathbf{S}$ is the covariance matrix of the data, $\mathbf{S}_*$ is the covariance vector between the measured data points and the new data point, and $\mathbf{N}$ is the noise covariance matrix. In Eq. 2.29-

2.30, the mean $\bar{y}$ is subtracted off the data before determining the coefficients [5], and is added back to the estimate afterwards. The variance of the true value s_* about the best estimate $\hat{s_*}$ is given by

$$\langle (s_* - \hat{s_*})^2 \rangle = \langle s_*^2 \rangle - \mathbf{S}_*^T [\mathbf{S} + \mathbf{N}]^{-1} \mathbf{S}_* \,. \tag{2.31}$$

In order to apply Eq. 2.30, the covariance structure of the underlying stochastic process must be estimated from the data. Assuming stationarity, so that $S_{ij} \equiv S(t_i - t_j) \equiv S(\Delta t)$, the covariance matrix can be replaced by the population mean square and the structure function $V(\Delta t)$:

$$S(\Delta t) = \langle s^2 \rangle - V(\Delta t) \,, \tag{2.32}$$

$$V(\Delta t) \equiv \frac{1}{2} \langle [s(t + \Delta t) - s(t)]^2 \rangle \,. \tag{2.33}$$

Following the method described by Press et al. (1992), for each pair (i, j) a lag $\Delta t_{ij} = |t_i - t_j|$ and an estimate of the structure function $v_{ij} = (y_i - y_j)^2 - n_i^2 - n_j^2$ are calculated, where n_i is the measurement error of data point y_i. The $M(M-1)/2$ pairs are binned into n_b bins, equally spaced in Δt. In Fig. 4.3, $\sqrt{v_{ij}}$ is plotted against Δt_{ij} in logarithmic scale for NGC 4151, and in Fig. 5.7 for NGC 3227. A straight line

$$\log(\sqrt{V(\Delta t)}) = \log(A) + \frac{\gamma}{2} \log(\Delta t) \tag{2.34}$$

is fitted to these data, representing a power-law model of the form

$$V(\Delta t) = A^2 \cdot \left(\frac{\Delta t}{1 \text{ yr}} \right)^\gamma \,. \tag{2.35}$$

A is the average flux variability on a one-year timescale, and γ is the gradient of this variability. With the obtained best-fit structure function parameter values, the covariance matrix and vector are calculated, and the input AD light-curve is interpolated according to Eq. 2.30. This light-curve is shown in Fig. 4.4 for the analysis of NGC 4151 and in Fig. 5.8 for NGC 3227.

An alternative approach of the structure function to describe AGN variability is the damped random walk (DRW) model:

$$V(\Delta t) = \sigma^2 \, (1 - \exp(-\Delta t / \mathscr{T}_\mathrm{d})) \,, \tag{2.36}$$

[5] The appropriate mean is calculated by

$$\bar{y} = \frac{\mathbf{E}^T [\mathbf{S} + \mathbf{N}]^{-1} \mathbf{y}}{\mathbf{E}^T [\mathbf{S} + \mathbf{N}]^{-1} \mathbf{E}} \,,$$

and corresponds to the value $\bar{y}$ that minimizes

$$\chi^2 = (\mathbf{y} - \mathbf{E}\bar{y})^T [\mathbf{S} + \mathbf{N}]^{-1} (\mathbf{y} - \mathbf{E}\bar{y})$$

when subtracted off the data.

where σ^2 is the long-term variance of the process, and $\mathscr{T}_\mathrm{d}$ the damping timescale. In comparison to a classical random walk, the exponential damping term ensures that the variability will not take arbitrarily large steps away from the mean. Compared to the power-law approach, while for a substantial Δt range, the variability increases with increasing time lag following a power-law $V(\Delta t) \propto \Delta t^\gamma$, the DRW model takes into account that there is a plateau at which the variability saturates, at time lags that are longer than the longest correlation timescale of the stochastic process (MacLeod et al., 2010; Beckmann & Shrader, 2012).

2.5 Model fitting using a Markov Chain Monte Carlo algorithm

2.5.1 Differential Evolution Markov Chain

For the inference of the best model parameters from the data, a Differential Evolution Markov Chain (DE-MC) algorithm was implemented (in IDL routines), in order to match the purposes of this project. DE-MC is a population Markov Chain Monte Carlo (MCMC) algorithm (Ter Braak, 2006), with multiple chains running in parallel. Its basic principle is similar to random walk metropolis (RWM) type MCMC algorithms: starting from an appropriately over-dispersed initial distribution for the model parameters, for each iteration step n and chain i, the probabilities $p(\mathbf{x}_i)$ of the current parameter vector $\mathbf{x}_i$ and $p(\mathbf{x}_\mathrm{p})$ of a proposal vector $\mathbf{x}_\mathrm{p}$ are evaluated. If the Metropolis ratio $p(\mathbf{x}_\mathrm{p})/p(\mathbf{x}_i)$ is higher than uniform$(0,1)$, $\mathbf{x}_i$ is replaced by $\mathbf{x}_\mathrm{p}$ in the next iteration step, otherwise $\mathbf{x}_i$ is retained. $\mathbf{x}_\mathrm{p}$ is thus accepted with probability $p = \min(1, r)$. This way, the algorithm will sample the high density regions of the target distribution.

The proposal vector, or precisely, its increment with respect to the current parameter vector, is generated by sampling from a suitable jumping distribution. RWM commonly uses a multivariate normal distribution as jumping distribution, with a covariance matrix that has to be appropriately estimated beforehand[6]. The main advantage of DE-MC is that the problem of choosing a jumping distribution and hence an appropriate scale and direction of the jumps, is solved by generating jumps as a fixed multiple of two random parameter vectors $\mathbf{x}_{R1}$ and $\mathbf{x}_{R2}$ that are currently in the population:

$$\mathbf{x}_\mathrm{p} = \mathbf{x}_i + \gamma \cdot (\mathbf{x}_{R1} - \mathbf{x}_{R2}) + \mathbf{e}\,, \tag{2.37}$$

where the small random number $\mathbf{e}$ is added to ensure that the whole parameter space can be reached. Recommended values for γ and the number m of chains are $\gamma \leq 2.38/\sqrt{2d}$ (d being the number of model parameters) and $2d \leq m \leq 20d$ (the more complicated the target distribution, the smaller γ and the larger m should be). With a proposal scheme of Eq. 2.37, the step-size and direction of the increments are obtained automatically. The

[6]The covariance matrix of this normal distribution has to be specified appropriately for the underlying target, in order to define a suitable scale and direction of the jumps, and thereby achieve a reasonable acceptance rate of the proposals. Therefore, often trials runs have to be performed in order to estimate the covariance matrix.

chains "learn from each other", hence the name "Differential Evolution".

2.5.2 Gelman convergence diagnostics

To check for convergence of the DE-MC algorithm, the Gelman convergence diagnostics proposed by (Gelman & Rubin, 1992) and Brooks & Gelman (1998) were applied. The idea is as follows: given m independent[7] chains and $2n$ iterations of the sampler, one can calculate for the second half of the iterations[8] in each step and for each parameter estimand x the potential scale reduction factor (PSRF)

$$\hat{R} = \frac{\hat{V}}{W} = \frac{\hat{\sigma}_+^2 + B/(mn)}{W}, \tag{2.38}$$

which serves as an (over-) estimate of the true scale reduction factor $R = \hat{V}/\sigma^2$. Here,

$$\hat{\sigma}_+^2 = \frac{n-1}{n} W + \frac{B}{n} \tag{2.39}$$

is an estimator of the true target variance σ^2 and is calculated by a weighted mean of the between-chain variance B/n

$$B/n = \frac{1}{m-1} \sum_{j=1}^{m} (\bar{x}_{j.} - \bar{x}_{..})^2, \tag{2.40}$$

i.e. the variance between the m chain means $\bar{x}_{j.}$ (where $\bar{x}_{..}$ denotes the global mean over all chains and iterations), and the pooled within-chain variance W:

$$W = \frac{1}{m(n-1)} \sum_{j=1}^{m} \sum_{t=1}^{n} (\bar{x}_{jt} - \bar{x}_{j.})^2. \tag{2.41}$$

The true target mean μ is estimated by the global sample mean of x, i.e. $\hat{\mu} = \bar{x}_{..}$, and the term $B/(mn)$ in Eq. 2.38 refers to the sampling variability of $\hat{\mu}$. As W always underestimates the true variance ($W \to \sigma^2$ for $n \to \infty$) for any finite n, the PSRF $\hat{R}$ will always overestimate the true scale reduction factor, and can be used as convergence diagnostic: High values of $\hat{R}$, i.e. values significantly above 1, indicate that further simulations may lead

[7] The DE-MC proposal scheme presented in Eq. 2.37 might at first glance seem to violate one of the basic assumptions for monitoring convergence with the $\hat{R}$-statistic of Gelman & Rubin (1992), namely the assumption that the m individual chains are independent of each other. However, Ter Braak (2006) demonstrates that the conditional stationary pdf of one individual chain does not depend on the states of the other chains and is identical for all chains, so that the joint stationary pdf $p(\mathbf{x}_1, ..., \mathbf{x}_m)$ of the m chains is simply given by the product $p(\mathbf{x}_1) \times ... \times p(\mathbf{x}_m)$. Thus, the states of the individual chains $\mathbf{x}_1, ..., \mathbf{x}_m$ are independent of each other at any iteration step after the burn-in phase (Ter Braak, 2006; Mengersen & Robert, 2003), i.e., after the algorithm has become independent of the starting distribution. Convergence of the DE-MC algorithm can therefore be monitored using Gelman's convergence criterion.

[8] Only the second half is evaluated in order to lower effects of the influence of the starting distribution, i.e., the burn-in phase is discarded.

to an improved inference of the target distribution – either because the variance estimates in the numerator of Eq. 2.38 can be further decreased by running more iterations, or because W will increase with continuing iterations, as the chains have not yet covered the complete target distribution. If $\hat{R}$ is close to 1, it can be assumed that W has nearly converged to the target variance and that each of the m chains of n iterations is sufficiently close to the target distribution.
The above holds if the sampler is started with a sufficiently over-dispersed starting distribution. Otherwise $\hat{R}$ values close to 1 might falsely diagnose convergence (Brooks & Gelman, 1998). Therefore, it is strongly recommended to graphically inspect the evolution of W and $\hat{V}$, to exclude that they are still evolving.

2.5.3 Implementation of the algorithm

The DE-MC algorithm for the 6-parameter 1BB model of Eq. 2.3 is run with 15 simultaneous Markov chains, and with 25 simultaneous chains for the case of the 10-parameter 2BB model of Eq. 2.5 as well as for the 10-parameter model of Eq. 2.6.

In each iteration step and for each chain, the algorithm evaluates – for the current parameter vector $\mathbf{x}_i$ and for the proposal vector $\mathbf{x_p}$ – the posterior probability density function (pdf)

$$\begin{aligned} p(\mathbf{x}|\mathbf{y}) &\propto p(\mathbf{x}) \cdot p(\mathbf{y}|\mathbf{x}) \\ &\propto p(\mathbf{x}) \cdot \exp\left(-\frac{\chi^2}{2}\right) \\ &= p(\mathbf{x}) \cdot \exp\left(-\frac{1}{2}\sum_{k=1}^{N}\left(\frac{m_k - y_k}{\sigma_k}\right)^2\right), \end{aligned} \tag{2.42}$$

which is proportional to the prior pdf times the likelihood function according to Bayes' theorem. Here, $\mathbf{x}$ represents the parameter vector, and $\mathbf{y}$ are the data. The notations m_k and y_k refer to the values of the model resp. the data for the kth data point of the complete data set, and σ_k is the related photometric error. For each parameter x, a uniform prior pdf

$$p(x) = \begin{cases} \frac{1}{x_{\max} - x_{\min}}, & x_{\min} \leq x \leq x_{\max} \\ 0, & x < x_{\min} \vee x > x_{\max} \end{cases} \tag{2.43}$$

is chosen within reasonable limits $x_{\min}, x_{\max}$, in order to exclude unphysical parameter ranges. Using uniform priors leads to the posterior pdf being directly proportional to the likelihood. The maximum of the posterior will occur when χ^2 is smallest.

A uniform distribution within the limits of the priors serves as initial distribution for the parameters, which is thus sufficiently over-dispersed.
For determination of convergence, a value $\hat{R} \leq 1.2$ is considered as sufficiently close to 1 in this work (Ter Braak, 2006), and W and $\hat{V}$ are graphically inspected.

3 NGC 4151: A first glance analysis

This chapter is based on the publication "Dust physics in NGC 4151" by Schnülle et al., which has been published in A & A (Schnülle et al., 2013).
The analysis presented here is based on the method described in Sect. 2.1. This first project uses a limited data set on a single target, NGC 4151, and focuses on the evolution of the hot dust temperature as the central parameter, in order to conclude on the temperature state and the stability of the hot dust distribution around this archetypical Seyfert 1 galaxy.

3.1 Introduction

Using dust reverberation mapping, the effects of AGN continuum variability are monitored, in order to determine the temperature and covering factor of the circumnuclear dust, and to constrain the physical conditions for dust survival and formation in the radiation field of the AGN. Multi-band photometry observations in the z, Y, J, H, and K bands were carried out on the nucleus of NGC 4151 over six epochs from 2010 January to June, supported by spectroscopic observations, in order to investigate the response of the hot dust to varying accretion disk emission. The data confirm that most of the hot dust reacts to increased radiation from the central source with a delayed brightening of roughly 50 days. In accretion disk brightening, no signatures of dust destruction are seen in the data. The innermost dust appears to increase in temperature rather than sublimate, suggesting that it is cooler than sublimation temperature and located beyond the current sublimation radius. The dust geometry is characterized here by interpreting the wavelength-dependent reverberation response with a simplified torus model, pointing to a static, radially extended distribution of the central ($\approx$0.1 pc) hot dust.

After presenting some basic information on NGC 4151 in Sect. 3.2, the observations are described in Sect. 3.3. The results on NGC 4151, as found in this project, are presented in Sect. 3.4, followed by a discussion in Sect. 3.5. Conclusions are given in Sect. 3.6.

3.2 The galaxy NGC 4151

NGC 4151 is a Seyfert 1 galaxy with the morphology of an intermediate spiral galaxy (SAB), i.e., in between the classifications of a barred spiral galaxy and an unbarred spiral galaxy in the galaxy morphological classification scheme. It was discovered by William Herschel on March 17 in the year 1787, and is located at a right ascension $\alpha = 12\text{h}\ 10\text{m}\ 32.5\text{s}$ and declination $\delta = +39^\circ\ 24'\ 21''$ in the constellation Canes Venatici. Its major diameter is roughly $6.3'$, and its minor diameter $4.5'$. The absolute magnitude of NGC 4151 in the V band is $M_V = -18.0$ mag (Véron-Cetty & Véron, 2010), and – compared to most other Seyfert

galaxies – it is a very bright source on the sky with an apparent magnitude of $m_V = 11.85$ mag.

NGC 4151 was one of the galaxies studied in the paper by Seyfert (1943) in the which the term “Seyfert Galaxy” was originally defined. In Fig. 3.1, a composite image of NGC 4151 is shown, combining X-ray data from the Chandra X-ray Observatory, optical observations of H II regions with the 1-meter Jacobus Kapteyn Telescope on La Palma, and radio observations of neutral hydrogen regions with the NSF Very Large Array. NGC 4151 is one of the most nearby galaxies hosting an actively growing black hole, with a redshift of $z = 0.003$. It is still an active debate whether or not NGC 4151 harbors a binary black hole in its center, with an orbital period of 15.8 years.

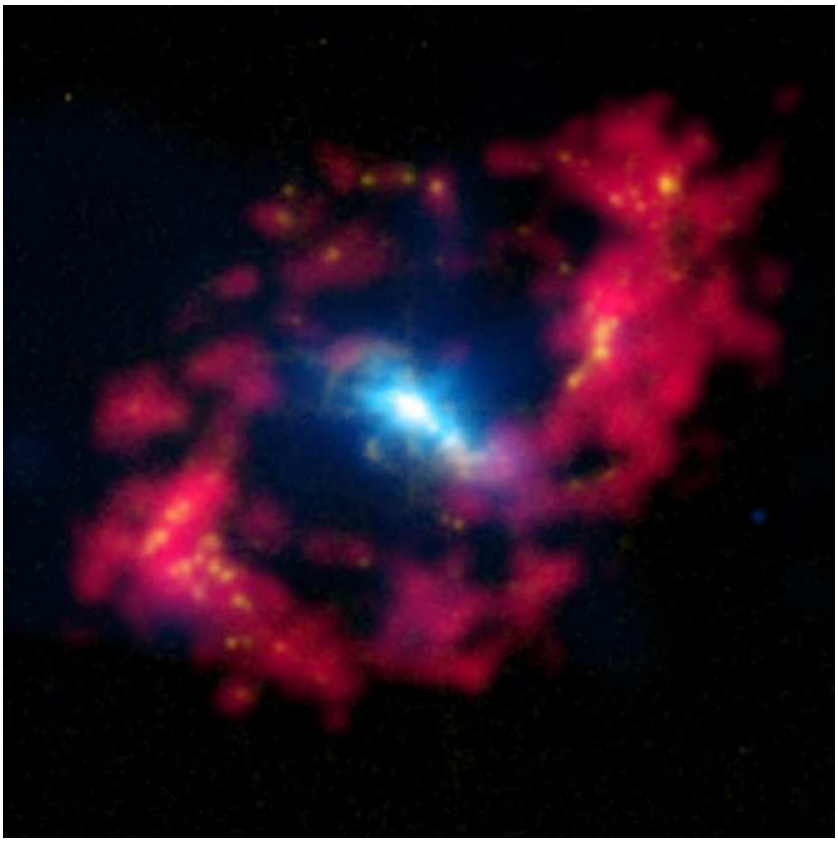

Figure 3.1: *The Seyfert 1 galaxy NGC 4151, observed at X-ray (blue), optical (yellow) and radio (red) wavelengths (Credit: NASA).*

NGC 4151, being one of the brightest and most nearby Seyfert 1 galaxies on the sky and highly variable in its continuum emission, is a perfect candidate for the hot dust reverberation study of this work.

3.3 Observations

As a start of the AGN hot dust monitoring program presented in this work, NGC 4151 was observed from 2010 January - 2010 June with a roughly monthly sampling, using NIR multi-band photometry obtained with Omega 2000 (Sect. 2.3.1). Images of NGC 4151 and three reference stars in the field of view in the spectral bands z, Y, J, H and K, were taken in six epochs in 2010. The five filters were chosen to be able to distinguish unambiguously between AD and hot dust emission. Dithering was used to estimate the sky background. High signal-to-noise ratios were reached with an on-source integration time of a few minutes for each filter and night. The weather conditions ranged from clear to photometric, and the typical seeing was $\sim 0.9''$ - $1.5''$.

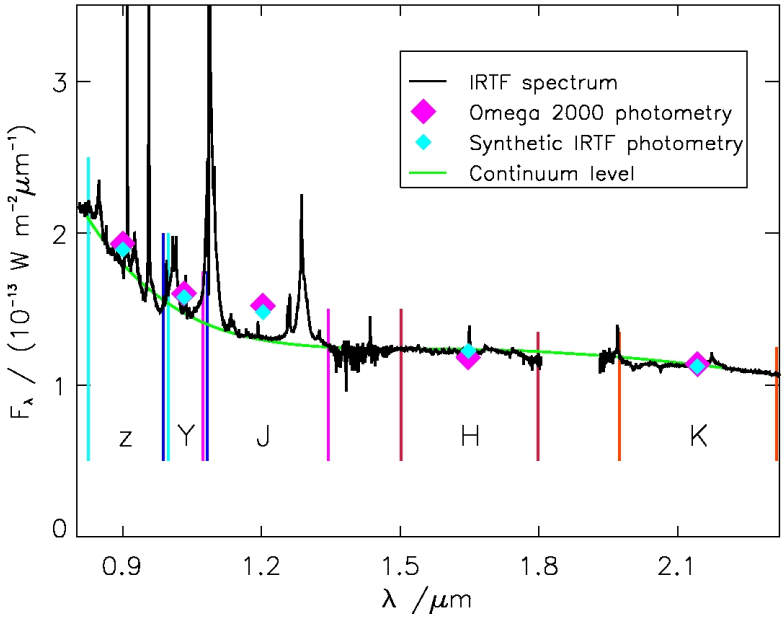

Figure 3.2: *The 2010 February (MJD 55252) photometry of the nucleus of NGC 4151, shown with the parallely observed IRTF spectrum. Vertical lines mark the filter widths of the zYJHK bands.*

Data reduction was performed as explained in Sect. 2.3.2. The nuclear fluxes were then extracted from the final science images using `GALFIT` (Sect. 2.3.3). For NGC 4151, the fit model consisted of the PSF plus a Sersic profile and an exponential disk profile. This strategy lead to sufficiently small statistical errors of the fit (typically ~ 0.01 mag for the brightness of the PSF and Sersic components, and ~ 0.02 mag for the disk component) as well as sufficiently smooth residuals. The Sersic half-light radii R_e, Sersic indices n, and disk scale lengths R_s for the different filters and epochs were found to be temporally stable. In a final fit, R_e, n, and R_s were fixed to their average values determined from the previous fits, i.e. $R_e = 9.0''$, $n = 3.0$, $R_s = 41.8''$. These parameter values for NGC 4151 are consistent

with the literature, e.g. Bentz et al. (2009).

Only in the PSF regime do the residuals significantly deviate from zero, while they are very smooth on larger scales. The residuals in the PSF domain are likely to be caused by the highly distorted PSF (due to defocussing plus seeing) which is in addition highly variable over the detector. Aperture photometry performed on these residuals yields low fluxes, on the order of a 2-3 % of the PSF flux of the AGN. The fluxes of the reference stars were determined by fitting the PSF model.

Absolute flux calibration was performed according to the description in Sect. 2.3.1. The flux ratios between the reference stars were found to be temporally stable for each filter, and the resulting photometric errors – which are dominated by spatial PSF variations – are in the range of $\sim$ 0.005 - 0.03 mag.

In order to correct for emission line contributions in the data, a NIR spectrum (0.8 - 5.0 μm) of NGC 4151 was obtained in parallel with the 2010 February photometry, using the SpeX spectrograph (Rayner et al., 2003) at the NASA Infrared Telescope Facility (IRTF), a 3m telescope on Mauna Kea, Hawai'i.
By combining the spectra observed in the short-wavelength cross-dispersed mode (SXD) and the long-wavelength cross-dispersed mode (LXD), the resulting wavelength coverage is 0.8 - 5.0 μm.

The 2010 February photometry is in excellent agreement with the synthetic photometry derived from the IRTF spectrum of NGC 4151 (see Fig. 3.2), indicating the high accuracy of the photometry results. For each filter, a correction factor was applied to the photometric data, given by the ratio of the measured 2010 February photometry to the continuum flux level at the respective effective wavelength, in order to remove the emission line contributions[1]. That is the photometry used throughout this Chapter.

For the analysis presented in the following of this Chapter, the single-epoch approach described in Sect. 2.1 was applied, i.e., the model given by Eq. 2.2 was fit to the SED of each single epoch, using the IDL routine `mpfit`.

3.4 Results

The temporal evolution of the band-normalized photometry of the nucleus of NGC 4151 is shown in Fig. 3.3 for the five filters. The flux variations in the other bands lag behind those in the AD-dominated z band, and this effect increases with wavelength. This band-wise behavior from z to K shows increasing dust contribution and decreasing AD contribution going to longer wavelengths, and one clearly sees that the hot dust – dominating the HK bands – reacts with delayed brightening to AD flux increases. The time lag between AD and

[1]Here, the emission line contributions are assumed to not change significantly over time, which is a valid zeroth order approximation (B. M. Peterson, priv. com.)

dust emission can be estimated by the separation of the z- and K-band peaks, yielding $\tau \sim$ 50 days, consistent with the observations by Minezaki et al. (2004) and Hönig & Kishimoto (2011).

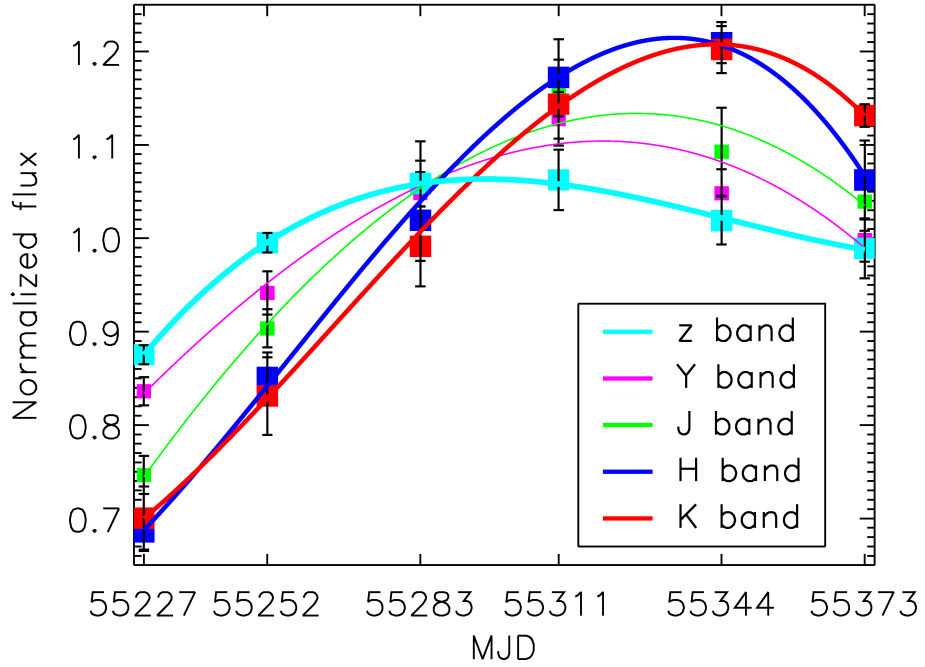

Figure 3.3: *Results from the 2010 data: Calibrated, band-normalized Omega 2000 photometry of NGC 4151. The average flux in each band has been normalized to unity to show the relative variability. Squares mark the data, while the continuous lines have been overplotted merely to guide the eye.*

Figure 3.4 shows the temporal evolution of the decomposed blackbody (dust) and power-law (AD) contributions. A significant rise of the hot dust emission is observed from epoch 1 (MJD 55227) to epoch 5 (MJD 55344), in correspondence to the clear flux increase in the H and K bands. Furthermore, from comparing the evolution of the AD and hot dust flux, it is found that the AD variability is completely reprocessed by the dust.

The hot dust temperature and blackbody constant are presented in Fig. 3.5 for the six observed epochs. A temperature increase from roughly 1300K to 1500K is found, with a peak at MJD 55319 – 30 days after the state of highest AD brightness (MJD 55289). The hot dust blackbody constant first decreases from epoch 1 (MJD 55227) to epoch 3 (MJD 55283), followed by a monotonic increase until epoch 6 (MJD 55373).

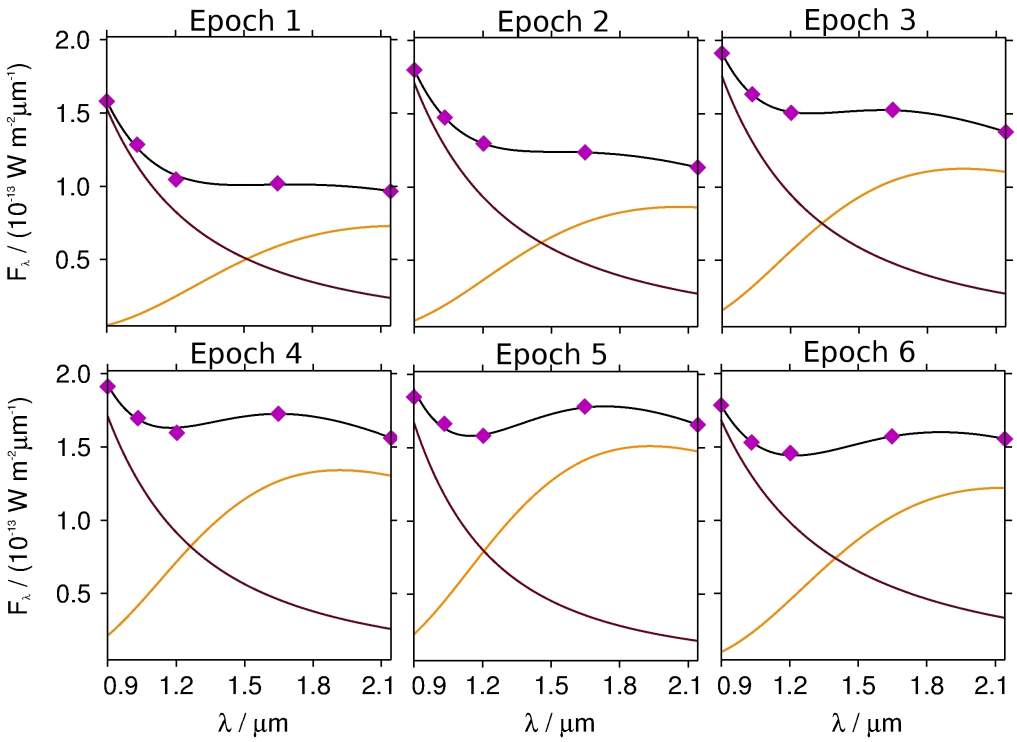

Figure 3.4: *Two-component decomposition of the SED into AD and hot dust contribution. The Omega 2000 zYJHK data of NGC 4151 are given by magenta squares. Purple lines and orange lines represent the power-law and blackbody contributions respectively, whereas the black lines show the sum of these two components.*

3.5 Discussion

Following times of high AD brightness in NGC 4151, a significant rise of the emission of the innermost hot dust is found, peaking with a time lag of roughly 50 days after the AD emission peaks. Furthermore, the hot dust temperature rises significantly from roughly 1300K to 1500K as a reaction to the increased irradiation by the central source.

This indicates that the hot dust in NGC 4151 is apparently not destroyed following the high AD state around MJD 55289, but is simply heated up, suggesting that the hot dust is cooler than sublimation temperature. It therefore seems likely that the dust in this galaxy is not located as far in as possible, but located or formed further out.

However, the observed behavior of the temperature as well as the blackbody deviates from what one would expect if the hot dust were well represented by a single blackbody function (i.e., a compact dust distribution with one unique temperature):

- The hot dust blackbody temperature peaks only $\sim$ 30 days after the state of highest AD emission, whereas the K-band flux shows a delay of roughly 50 days.

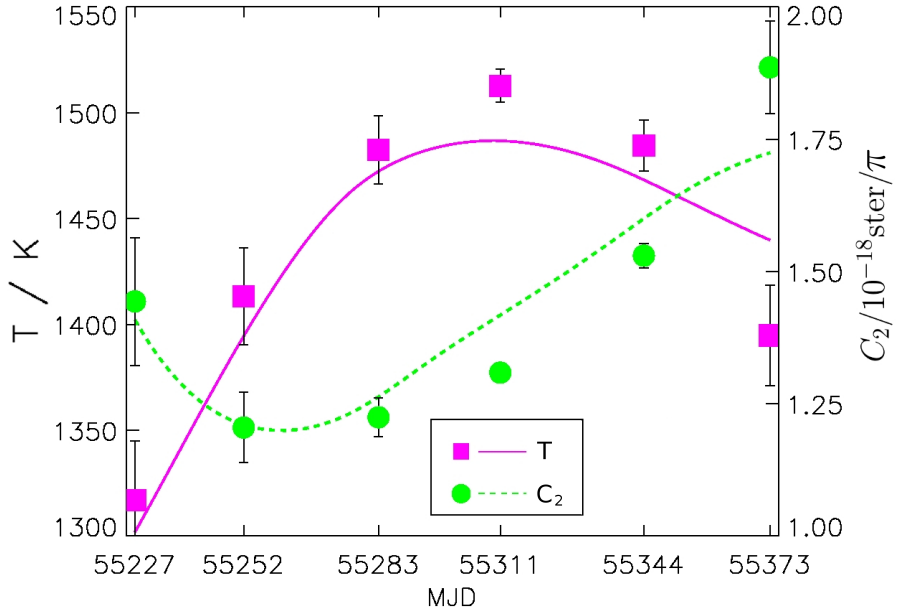

Figure 3.5: *Temporal evolution of the blackbody temperature and blackbody constant for the innermost, hot dust of NGC 4151, derived from the two-component decomposition (magenta squares and green circles). The solid magenta and dashed green lines represent the temperature and blackbody constant as calculated from the simplified torus model (see Sect. 3.5).*

- The blackbody constant decreases from epoch 1 to epoch 3, before it starts to rise monotonically again until epoch 6.

This observed behavior might be resolved, if a radially extended distribution of the innermost, hot dust is assumed. In this case, the dust would be better approximated by a continuous radial distribution of blackbody components with different temperatures – higher temperatures corresponding to a smaller distance from the source. To test this assumption, a very basic torus model is applied, making use of the following simplifications:

(1) No radiative transfer model is used, but a simple, multi-component blackbody model. For each radius, a single radiating surface is used, represented by a single blackbody function.

(2) The model is static, i.e. the dust distribution does not vary over time.

(3) Only directly illuminated dust contributes significantly to the observed flux (Hönig & Kishimoto, 2010).

(4) The continuous radial structure is approximated as the discrete sum of only a few blackbody components, located at different radial distances from the center.

(5) The variation of the dust temperature at each surface due to the changing AD irradiation is given by $\mathrm{d}T/T = 1/4 \cdot \mathrm{d}L/L$ (Hönig & Kishimoto, 2011), assuming that variations in the incident radiation are completely reprocessed by the dust. Here, the blackbody assumption (absorption efficiency $Q_{\mathrm{abs}}(\nu, T) = 1$) is used, which is a sufficiently good approximation according to Hönig & Kishimoto (2011).

(6) As the main heating source for the dust is the UV part of the AD radiation, $\mathrm{d}L/L \approx \mathrm{d}L_{\mathrm{UV}}/L_{\mathrm{UV}}$ is used as approximation. Considering $F_\lambda \propto \lambda^{-2}$ (Meusinger et al., 2011), and assuming $F_\lambda \propto \lambda^{-1.75}$ in the UV - z regime (Zheng et al., 1997; Kishimoto et al., 2008), the UV luminosity variations are predicted by the z-band variations according to $\mathrm{d}L_{\mathrm{UV}}/L_{\mathrm{UV}} \approx 1.8 \cdot \mathrm{d}L_z/L_z$.

A model consisting of three blackbody components – with 5% of the hot dust being located at 25 light-days distance from the source, 25% at 50 light-days distance and 70% at 100 light-days distance already matches the data sufficiently well (see Fig. 3.5). The model deviations from the SED fit show a similar behavior for the temperature and solid angle, and including further components might lead to an even better agreement with the data. In contrast, when using one component only, it is not possible to reproduce the observed behavior.

This suggests that, in fact, the innermost hot dust might be well-represented by a radially extended distribution rather than one compact component. Thus, a small innermost fraction of the dust sees the increased AD emission first, therefore increasing its temperature and NIR emission prior to the dust located further out. This leads to a stronger weighting of this small fraction of the hottest, innermost dust, and therefore to an early temperature peak (i.e. earlier than the HK bands which represent the bulk of the hot dust) and an overall decrease in the emitting surface in the early epochs, before the other dust surfaces start to respond as well.

In this picture, the innermost dust morphology would not have a well-defined sharp edge, but dust clouds would start to be present from the outer edge of the BLR on. This is in good agreement with the accretion wind scenarios (see Sect. 1.3.5), in which the BLR and the dust torus are assumed to be essentially the same phenomenon, and the transition between BLR and dust torus occurs simply when the dust condensation conditions are fulfilled.

Furthermore, a very good agreement between the observed temperature variations and those predicted by the model is found, which supports the finding from Sect. 3.4 that the variations in the incident AD radiation are completely reprocessed by variations in the hot dust emission. This can only be achieved with constant covering factors, and thus points at a static dust distribution without significant dust destruction.

3.6 Conclusions

In this project, dust reverberation was used as a tool to explore the dust morphology in AGNs. As a first step, NIR multi-band photometry was carried out on the nucleus of the Seyfert 1 galaxy NGC 4151 with Omega 2000 (Calar Alto, Spain) in six epochs in 2010, supplemented by a NIR IRTF spectrum in 2010 February. The first results are as follows:

- From the NIR light-curves of NGC 4151, a lag time of roughly 50 days between the AD emission (represented by the z band) and the K-band hot dust emission is found, which is in very good agreement with previously measured single-band hot dust reverberation lags.
- A significant rise of the hot dust emission is observed following times of high AD brightness. Moreover, the hot dust blackbody temperature increased as a reaction to the enhanced irradiation from the central source, with a lag time of roughly 30 days.
- Indications are found that the morphology of the innermost hot dust is static and does not have a sharp inner edge, but is rather radially extended.

Central finding is that a static dust distribution can explain the observed flux and temperature variations. While motion is not expected on half-year timescales[2], significant dust destruction in bright times can be excluded in the observed period.
With a temporally extended data set of observations of NGC 4151 (see Chapter 4), however, a potential change in the dust distribution might be detected.

[2]Assuming that the BLR clouds move outwards with speeds of $v \ll c$ (Elvis et al. (2002) assume $v \gtrsim$ 1000km s^{-1}), the time scale for significant changes in the dust morphology would be substantially larger than the six months of monitoring.

4 NGC 4151: Extended analysis

This chapter is based on the publication "Monitoring the temperature and reverberation delay of the circumnuclear hot dust in NGC 4151" by Schnülle et al., which has been published in A & A (Schnülle et al., 2015).
The analysis in this project is based on the method presented in Sect. 2.2.1, which constitutes a more robust approach than the one used in the previous Chapter. Moreover, not only the hot dust temperature (as in Chapter 3) or the reverberation delay (as for conventional reverberation studies) are derived, but a more comprehensive set of characteristic quantities characterizing the hot dust is monitored, with the aim to investigate its temperature state, long-term stability, and radial distribution.

4.1 Introduction

Reverberation mapping of the hot circumnuclear dust in NGC 4151 is used, to monitor its temperature and reverberation lag as a function of the varying accretion disk brightness. Multi-band, multi-epoch photometric observations of the nucleus of NGC 4151 in the z, Y, J, H, and K bands were carried out for 29 epochs from 2010 January to 2014 June, supported by new NIR and optical spectroscopic observations, and archived WISE data. No signatures of dust destruction due to sublimation are seen in the data, since they show no increase in the hot dust reverberation delay directly correlated with substantial accretion disk flux increases in the observed period. Instead, the hot dust in NGC 4151 appears to merely heat up, and the hot dust temperature closely tracks the accretion disk luminosity variations. Indications of a decreased reverberation delay within the observed period are found, from $\tau = 42.5 \pm 4.0$ days in 2010 to $\tau = 29.6 \pm 1.7$ days in 2013-2014. Such a varying reverberation radius on longer timescales would help to explain the intrinsic scatter observed in the radius-luminosity relation of dust around AGNs. The observations rule out that a second, larger dust component within a 100-light-day radius from the source contributes significantly to the observed NIR flux in this galaxy.

In comparison to the analysis presented in Chapter 3, the data set was substantially extended, by using a significantly longer time series and a broader wavelength coverage. The reduction and analysis techniques were extended as well, performing precise photometry with an image subtraction method (see Sect. 2.3.4), using a sophisticated interpolation method for the input light-curves (see Sect. 2.4), and employing a multi-epoch multi-wavelength MCMC fit (see Sect. 2.5).

The observations are described in Sect. 4.2, and Sect. 4.3 gives some target-specific details concerning the methods presented in Chapter 2. The updated results on NGC 4151 are

Table 4.1: *NIR fluxes of the nucleus of NGC 4151, derived with* ISIS.

Epoch	MJD	F_λ / $10^{-13} W\,m^{-2}\mu m^{-1}$				
		z	Y	J	H	K
1	55227	1.321 ± 0.103	1.107 ± 0.074	1.075 ± 0.039	0.970 ± 0.032	0.965 ± 0.034
2	55252	1.577 ± 0.068	1.324 ± 0.052	1.284 ± 0.043	1.239 ± 0.045	1.127 ± 0.051
3	55283	1.691 ± 0.070	1.469 ± 0.050	1.489 ± 0.051	1.499 ± 0.054	1.397 ± 0.034
4	55311	1.733 ± 0.059	1.550 ± 0.044	1.585 ± 0.071	1.637 ± 0.052	1.529 ± 0.08
5	55344	1.573 ± 0.085	1.431 ± 0.058	1.536 ± 0.043	1.723 ± 0.049	1.643 ± 0.056
6	55373	1.530 ± 0.083	1.390 ± 0.042	1.424 ± 0.064	1.546 ± 0.050	1.543 ± 0.056
7	55969	0.739 ± 0.075	0.516 ± 0.056	0.625 ± 0.060	0.712 ± 0.083	0.802 ± 0.037
8	55998	0.630 ± 0.050	0.483 ± 0.037	0.539 ± 0.056	0.605 ± 0.040	0.642 ± 0.041
9	56024	0.950 ± 0.032	0.749 ± 0.039	0.7142 ± 0.064	0.653 ± 0.073	0.670 ± 0.042
10	56255	1.270 ± 0.061	1.038 ± 0.042	1.080 ± 0.060	1.068 ± 0.040	1.004 ± 0.033
11	56264	1.030 ± 0.034	0.881 ± 0.033	0.971 ± 0.031	0.973 ± 0.030	0.969 ± 0.050
12	56285	1.193 ± 0.082	1.195 ± 0.172	1.089 ± 0.060	1.116 ± 0.035	1.086 ± 0.039
13	56319	1.169 ± 0.040	1.047 ± 0.035	1.103 ± 0.033	1.161 ± 0.039	1.199 ± 0.037
14	56374	0.953 ± 0.074	0.770 ± 0.045	0.826 ± 0.064	0.889 ± 0.064	0.915 ± 0.033
15	56436	1.007 ± 0.030	0.830 ± 0.030	0.901 ± 0.030	0.977 ± 0.030	0.966 ± 0.030
16	56465	0.721 ± 0.037	0.570 ± 0.048	0.746 ± 0.039	0.827 ± 0.032	0.913 ± 0.039
17	56500	0.558 ± 0.035	0.389 ± 0.055	0.526 ± 0.043	0.626 ± 0.059	0.701 ± 0.039
18	56523	0.613 ± 0.067	0.462 ± 0.063	0.578 ± 0.057	0.570 ± 0.048	0.648 ± 0.038
19	56586	0.914 ± 0.039	0.732 ± 0.035	0.791 ± 0.079	0.781 ± 0.080	0.857 ± 0.048
20	56611	0.917 ± 0.031	0.736 ± 0.058	0.862 ± 0.032	0.916 ± 0.033	0.909 ± 0.071
21	56617	0.810 ± 0.034	0.675 ± 0.074	0.792 ± 0.031	0.885 ± 0.032	0.921 ± 0.040
22	56669	0.500 ± 0.036	0.393 ± 0.037	0.453 ± 0.055	0.592 ± 0.035	0.729 ± 0.045
23	56732	0.498 ± 0.039	0.393 ± 0.042	0.378 ± 0.034	0.358 ± 0.044	0.413 ± 0.051
24	56737	0.559 ± 0.034	0.392 ± 0.040	0.400 ± 0.039	0.357 ± 0.048	0.413 ± 0.044
25	56763	0.569 ± 0.040	0.394 ± 0.051	0.453 ± 0.030	0.434 ± 0.038	0.469 ± 0.034
26	56787	0.505 ± 0.056	0.418 ± 0.031	0.453 ± 0.040	0.482 ± 0.042	0.520 ± 0.037
27	56792	0.501 ± 0.032	0.380 ± 0.038	0.453 ± 0.035	0.465 ± 0.044	0.533 ± 0.042
28	56797	0.560 ± 0.043	0.392 ± 0.055	0.464 ± 0.043	0.482 ± 0.043	0.526 ± 0.042
29	56826	0.551 ± 0.049	0.429 ± 0.043	0.478 ± 0.047	0.482 ± 0.030	0.532 ± 0.030

presented in Sect. 4.4, and discussed in Sect. 4.5. A summary of the results is given in Sect. 4.6.

4.2 Observations

4.2.1 Near-infrared data

Following the 2010 January - June NIR multi-band photometric observations of the NGC 4151 (see Sect. 3.3) with Omega 2000, monitoring of NGC 4151 was continued from 2012 February - 2014 June, with roughly 2-4 weeks sampling (apart from data gaps in 2010 July - 2012 February and 2012 May - November). In each of the 29 epochs, broadband photometry of NGC 4151 and of three calibration stars in the field of view were obtained in the z, Y, J, H, and K spectral bands. The weather conditions ranged from clear to photometric, and the

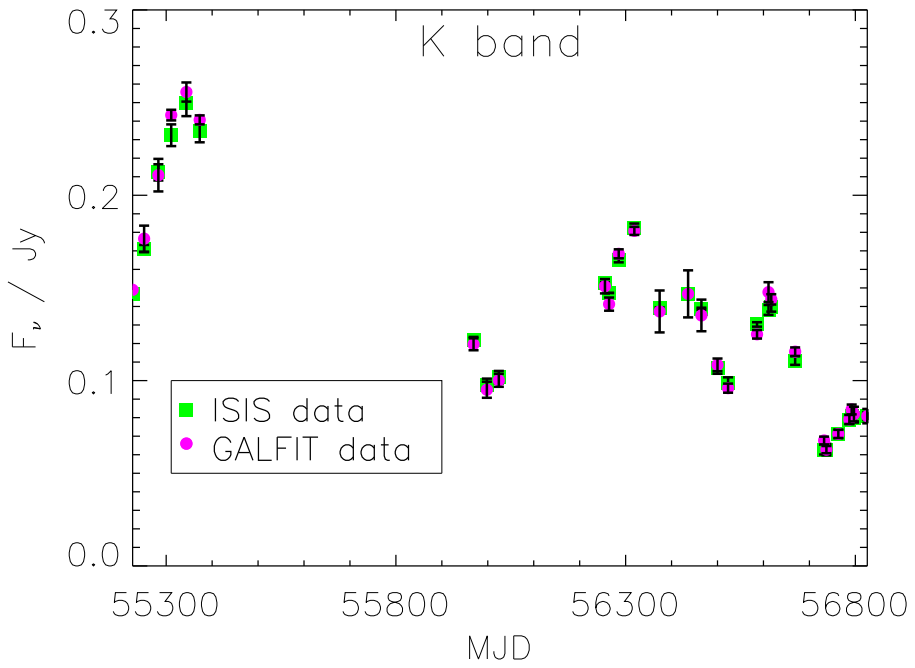

Figure 4.1: *Nuclear fluxes of NGC 4151 derived with* `ISIS` *(green) and* `GALFIT` *(magenta), shown here for the K band. Within the photometric errors, excellent agreement is found between the two methods. The agreement is on a similar level for all other bands, suggesting that both methods manage to separate the nuclear flux of interest from the bulge and disk.*

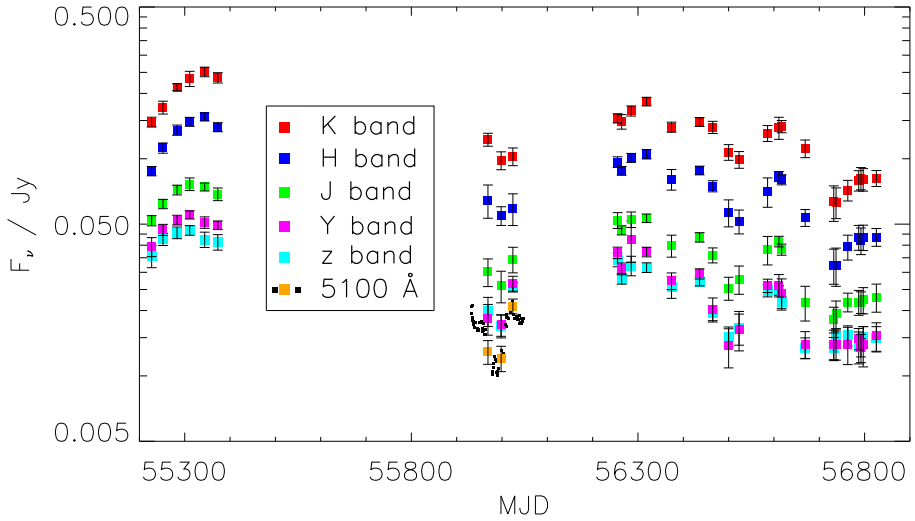

Figure 4.2: *Calibrated 2010 - 2013 photometry of NGC 4151. The optical data are plotted in orange for the epochs that coincide with the NIR epochs, and in black otherwise. Photometry of the NIR data has been performed with* `ISIS`*, and is highly consistent with the previously determined fluxes with* `GALFIT` *(also see Fig. 4.1).*

Table 4.2: *WISE W1, W2, W3 photometric fluxes of NGC 4151, derived with* GALFIT. *Very good agreement is found with the total NGC 4151 fluxes as listed in the ALLWISE catalog (column 5). The fluxes in column 4 are systematically slightly lower than the catalog fluxes, which is partly caused by the correction term that was applied to shift the derived* GALFIT *fluxes from the mean epoch to 2010 May (see text for details). From 2010 May-December, the AGN got approximately 25% brighter.*

Filter	F_λ / $10^{-13} W\,m^{-2}\mu m^{-1}$			
	AGN	host	total	total acc. ALLWISE
W1	0.685 ± 0.094	0.625 ± 0.077	1.311 ± 0.171	1.625 ± 0.088
W2	0.538 ± 0.068	0.301 ± 0.101	0.839 ± 0.170	1.022 ± 0.044
W3	0.192 ± 0.035	0.076 ± 0.011	0.268 ± 0.047	0.311 ± 0.028

seeing was 0.9″-2.5″.

Following the data reduction with IRAF, the nuclear fluxes of NGC 4151 were extracted at various epochs and filters, using GALFIT and ISIS. First, a PSF-bulge-disk decomposition with GALFIT (Peng et al., 2002) was performed, as already described for the 2010 data (see Sect. 3.3). Absolute flux calibration was performed as described in Sect. 2.3.1, and resulting photometric uncertainties were ≈ 0.005 - 0.05 mag.

As an alternative to GALFIT, photometry was performed with ISIS, as described in Sect. 2.3.4. As can be seen in Fig. 4.1 for the *K* band, the GALFIT and ISIS fluxes agree well within the given errors. The ISIS photometry (listed in Table 4.1) is used throughout this Chapter.
Further, the fluxes were corrected for foreground Galactic extinction, using the Schlafly & Finkbeiner (2011) recalibration of the dust map by Schlegel et al. (1998), as given in the NASA/IPAC Extragalactic Database (NED)[1].
Emission line contributions were removed from the total nuclear fluxes in the same way as for the 2010 data (Sect. 3.3).

4.2.2 Mid-infrared data

Furthermore, MIR images of NGC 4151 in the WISE W1, W2, and W3 bands were used, downloaded from the NASA / IPAC Infrared Science Archive (IRSA), and the nuclear fluxes were extracted with GALFIT. The downloaded images in each band are a stack of 31 individual frames, taken on 2010 May 31 and 2010 December 08. Whereas images are only available in stacked form, the total magnitude per band is given in the ALLWISE multi-epoch catalog table for each of the 31 individual observations. From a weighted magnitude difference between 2010 May and 2010 December (that was here attributed to the variability of the nucleus), a correction term was derived to scale the nuclear fluxes determined with GALFIT to the epoch 2010 May 31 (MJD 55347, then almost coinciding with epoch 5 of

[1]This research has made use of the NASA/IPAC Extragalactic Database (NED) which is operated by the Jet Propulsion Laboratory, California Institute of Technology, under contract with the National Aeronautics and Space Administration.

the NIR observations). The derived AGN and host fluxes are listed in Table 4.2. The total flux in each band agrees very well with the average total flux for NGC 4151 given in the ALLWISE catalog.

4.2.3 Optical data

Further, optical spectra were obtained between 2012 January and April as part of a reverberation mapping campaign described elsewhere (De Rosa & et al., 2017). Observations were made on the 1.3-m McGraw-Hill Telescope at the MDM Observatory on Kitt Peak with the Boller & Chivens CCDS spectrograph. A 350 lines mm^{-1} grating yielded a dispersion of 1.33 Å $pixel^{-1}$. The entrance slit was oriented North–South (P.*A.* $= 0^o$) with a projected width of $5.0'$. This configuration yielded spectra covering the range 4400–5850 Å, with a spectral resolution of 7.9 Å. An extraction window of $15.0'$ in the cross-dispersion direction was used.

Spectra were scaled to a common [O III] λ4959 flux of 3.76×10^{-12} ergs $s^{-1}\,cm^{-2}$. The starlight contribution to each spectrum was estimated from host-galaxy surface brightness models based on Hubble Space Telescope images as 18.4 ($\pm$1.8) $\times 10^{-15}$ ergs $s^{-1}\,cm^{-2\ -1}$ (Bentz et al., 2013).

The continuum fluxes at 5100 Å (listed in Table 4.3) are then derived by averaging the spectrum over a 20 Å range around the lowest point, which is located between the [O III] λ4959, λ5007 lines and the [Fe II] blends.

4.3 Methods

The two reverberation models described by Eq. 2.3 and Eq. 2.5 were fit to the data, with the algorithm described in Sect. 2.5.

For the interpolation of the AD signal (given by the z-band light-curve) as input to the fit, the formalism by Rybicki & Press (1992), presented in Sect. 2.4, was implemented and used. To test the influence of the particular choice of structure function model and its parameters, three different structure functions models were applied for the interpolation.

First, a power-law structure function approach given by Eq. 2.35 was used. From the data, best-fit structure function parameter values of $A = 0.011 \pm 0.001$ Jy (resp. $A = 0.423 \pm 0.019 \cdot 10^{-13}$W $m^{-2}\mu m^{-1}$) and $\gamma = 0.881 \pm 0.067$ are obtained from the z-band data. With these values, the z-band light-curve is interpolated according to Eq. 2.30. The interpolated z-band light-curve is shown in Fig. 4.4. Since the measurement errors are generally small (at the 5% level), the interpolated light-curve runs almost perfectly through the data points. In Fig. 4.3, a potential substructure seems to be evident around $\Delta t = 2.5$ yrs. However, this apparent feature might be merely an artifact, caused by insufficient sampling in that range of Δt. Indeed, the bins around $\Delta t = 2.5$ yrs contain by far the least amount

Table 4.3: *Optical continuum fluxes of the nucleus of NGC 4151 at 5100 Å .*

MJD	F_λ ($10^{-13} W m^{-2} \mu m^{-1}$)	ΔF_λ ($10^{-13} W m^{-2} \mu m^{-1}$)	MJD	F_λ ($10^{-13} W m^{-2} \mu m^{-1}$)	ΔF_λ ($10^{-13} W m^{-2} \mu m^{-1}$)
55932	2.243	0.208	55991	1.155	0.204
55933	2.401	0.209	55992	1.241	0.204
55934	2.443	0.209	55997	1.436	0.205
55935	2.150	0.208	55998	1.392	0.205
55936	2.079	0.208	55999	1.515	0.205
55937	2.047	0.207	56000	1.352	0.205
55938	1.997	0.207	56001	1.386	0.205
55940	1.917	0.207	56002	1.412	0.205
55941	2.022	0.207	56003	1.469	0.205
55945	1.914	0.207	56004	1.446	0.205
55946	1.885	0.207	56008	1.993	0.207
55947	1.860	0.207	56009	1.955	0.207
55948	1.881	0.207	56010	2.147	0.208
55949	1.860	0.207	56011	2.218	0.208
55950	2.035	0.207	56012	2.151	0.208
55952	2.022	0.207	56014	2.116	0.208
55954	2.049	0.207	56016	2.342	0.209
55957	1.911	0.207	56017	2.417	0.209
55958	1.847	0.207	56018	2.411	0.209
55959	1.863	0.207	56019	2.258	0.209
55960	2.012	0.207	56021	2.483	0.209
55961	1.886	0.207	56022	2.489	0.209
55962	1.792	0.206	56023	2.548	0.210
55963	1.879	0.207	56024	2.413	0.190
55964	1.785	0.206	56026	2.205	0.189
55968	1.543	0.205	56028	2.118	0.189
55969	1.490	0.205	56031	2.161	0.189
55978	1.171	0.204	56034	2.118	0.189
55979	1.208	0.204	56035	2.104	0.189
55981	1.265	0.204	56036	2.087	0.189
55982	1.310	0.205	56038	2.018	0.188
55983	1.409	0.205	56039	2.180	0.189
55984	1.422	0.205	56040	2.032	0.188
55985	1.373	0.205	56042	2.124	0.189
55987	1.344	0.205	56043	2.007	0.188
55988	1.191	0.204	56045	2.051	0.188
55989	1.197	0.204	56046	2.070	0.189
55990	1.203	0.204	56047	2.120	0.189

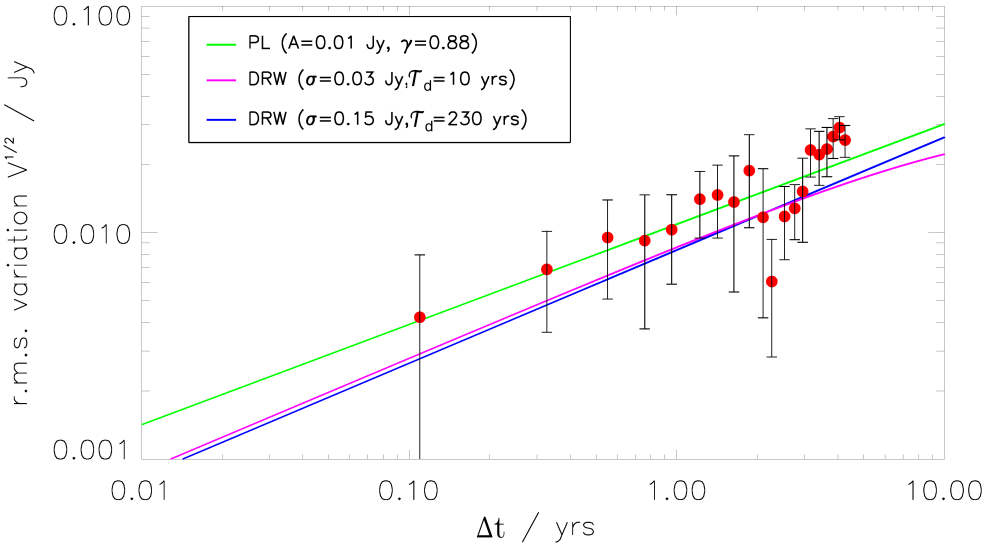

Figure 4.3: *The estimated* $(v_{ij})^{1/2}$ *(red dots) from the z-band data versus* Δt_{ij}*, shown in logarithmic scale. The three different structure function models that fit to these data (see text of Sects. 2.4 and 4.3) are represented by the green, magenta, and blue lines.*

of data points, obviously due to the large data gap between June 2010 and February 2012. An apparent feature as seen in Fig. 4.3 seems to be common in the empirical structure functions of single targets (see e.g. figures in Press et al. (1992), Schmidt et al. (2010), and Morganson et al. (2014)), while it is averaged out in the observed structure function of samples of AGNs (see e.g. Schmidt et al. (2010)).

The derived power-law structure function parameters are in agreement with values found in the literature. While typical values of the power-law slope are $\gamma \approx 0.3-0.4$ (Bauer et al., 2009; Schmidt et al., 2010), specifically for NGC 4151, Czerny et al. (2003) report power-law slopes of $\approx 0.65-1.0$ for the V-band structure function at different timescales and epochs.

Further, the alternative DRW model structure function was used, and best-fit parameter values $\sigma = 0.148 \pm 0.505$ Jy and $\mathcal{T}_{\rm d} = 230.0 \pm 576.1$ yrs were obtained from the z-band data. Clearly, the fitted damping timescale, typically between 0.1 and 3 years (MacLeod et al., 2010), seems physically unreasonable. When looking at the observed structure function data plotted in Fig. 4.3, it can be seen that obviously the time series is not long enough to sufficiently constrain the damping timescale for NGC 4151, as also evident from its large error. Obviously, no plateau is reached, but the variability increases throughout the observed time range. This is consistent with the results of Czerny et al. (2003), who find an unusually long damping timescale of roughly 10 years for this object. As third approach, the fit was re-performed, with fixed $\mathcal{T}_{\rm d} = 10$ yrs, leading to $\sigma = 0.032 \pm 0.002$ Jy.

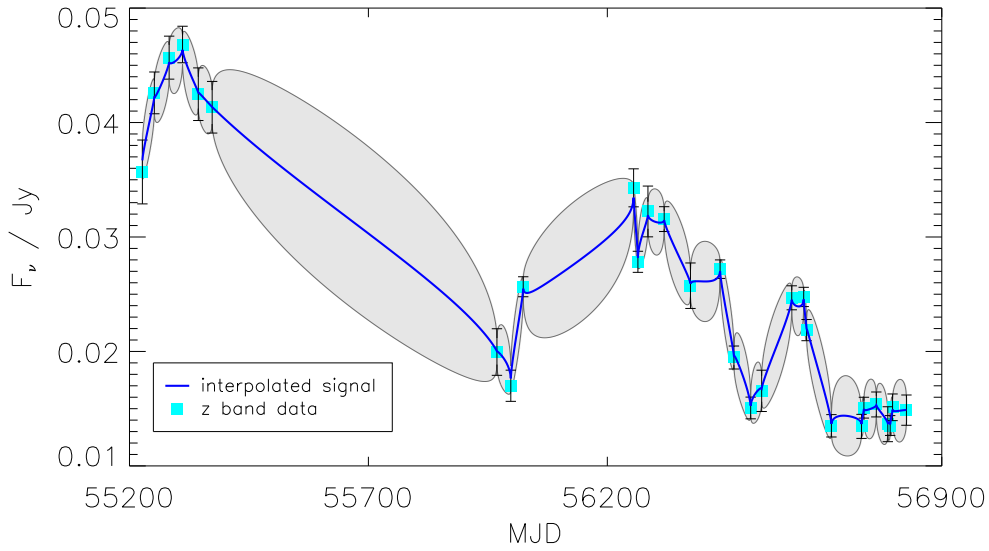

Figure 4.4: *The z-band light-curve, interpolated with the method of Rybicki & Press (1992). Interpolations were performed using the three models described in Sects. 2.4 and 4.3. For clarity, only the interpolation resulting from the power-law structure function is shown here. This interpolated signal is the least variance estimate of the stochastic process and therefore very smooth. The error of this prediction is indicated by the shaded gray region. Single realizations of the process have much more structure on short timescales and will also make excursions outside of the estimated error regions.*

The obtained structure functions for the power-law and the DRW model are plotted in Fig. 4.3. To test the influence of the particular choice of structure function on the robustness of the results, all of the analyses presented in the following of this chapter (i.e., the interpolation of the AD signal as well as the various fits) were performed with all three models shown in Fig. 4.3.

The DE-MC algorithm was run for the 6-parameter 1BB model of Eq. 2.3 with 15 simultaneous Markov chains, and with 25 simultaneous chains for the case of the 10-parameter 2BB model of Eq. 2.5.

A total of the $N = 211$ NIR plus optical data points (the WISE data were not included into the model fit) were used for the fit. However, to not overweight the low flux epochs around MJD 56000, where all of the 5100 Å measurements are assembled, in the evaluation of χ^2 and hence the pdf given by Eq. 2.42, a weighted $\chi^2 = \chi^2_{\rm NIR} + \chi^2_{5100}/3$ was used. Thus, the effective number of data points is $N = 160$.

The limits for the prior pdfs used for each parameter are given in Table 4.4. The 1BB model converged within 10000-15000 iterations on average. The alternative 10-parameter 2BB model took 50000-100000 iterations on average to converge. Figure 4.5 shows the evolution of the parameter $T_{0,1}$ (for one chain and for the population mean) of the model described by Eq. 2.3, for one exemplary run, as well as the evolution of the pooled within

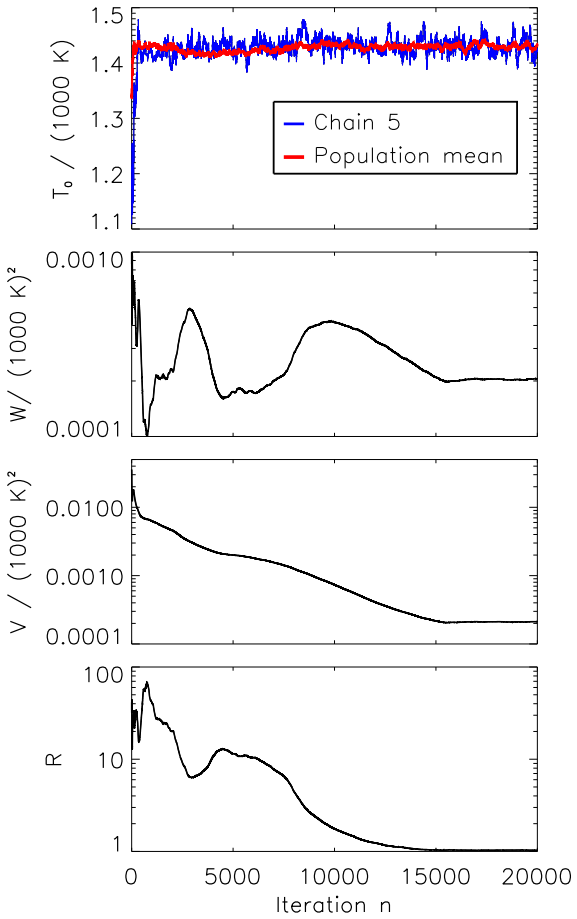

Figure 4.5: *To demonstrate the convergence diagnostics, the evolution of the parameter $T_{0,1}$ (for one chain and the population mean) of the model described by Eq. 2.3 is shown, for one exemplary run in the analysis of NGC 4151 (Chapter4). Further shown are the evolution of W, $\hat{V}$, and $\hat{R}$. Convergence was diagnosed at iteration step $n = 13599$, where $\hat{R} < 1.1$ was reached for all parameters. Graphical inspection shows that W and $\hat{V}$ are not evolving anymore and convergence was diagnosed correctly.*

chain variance W (Eq. 2.41), maximum variance estimate $\hat{V}$ (defined in Eq. 2.38) and the resulting convergence parameter $\hat{R}$ (Eq. 2.38).

4.4 Results

4.4.1 Constant power-law index

All results presented in this section were obtained using the power-law structure function model and a constant AD power-law index α. For results under the use of different structure function and α models, see Sect. 4.4.2 and Sect. 4.5.3. The temporal evolution of the photometry of the nucleus of NGC 4151 is shown in Fig. 4.2. The flux variations in the

Table 4.4: *Upper and lower limits x_{min}, x_{max} for uniform pdfs of the model parameters, for the 1BB model (with constant and varying α) and the 2BB model. The upper limit for C_1 is given by the fact that for the z band ($\lambda \approx 0.9\mu m$), $C_1 \cdot \lambda^{\alpha}$ must not exceed 1. In the 2BB model, the maximum temperature for the second blackbody component is given by $T_{max} = T_1 \cdot \sqrt{\tau_1/\tau_2}$. A value of $\tau_2 = 100$ days was chosen as an upper limit for the reverberation lag of the second blackbody component, because at that distance (and resulting low temperatures), its contribution to the NIR fluxes would become negligible, unless the blackbody constant C_3 would be several orders of magnitude higher than C_2. Further, $p(\tau_2) = 0$ for $\tau_2 < \tau_1$ was set.*

Parameter	Unit	1BB model		1BB model (var. α)		2BB model	
		x_{min}	x_{max}	x_{min}	x_{max}	x_{min}	x_{max}
C_1	–	0.0	0.85	0.0	0.85	0.0	0.85
α	–	1.5	2.5	1.5	2.5	1.5	2.5
α_1	–	–	–	0.0	1.0	–	–
C_2	10^{-18}ster	1.0	30.0	1.0	30.0	1.0	20.0
$T_{0,1}$	1000K	1.0	2.0	1.0	2.0	1.0	2.0
τ_1	days	0.0	80.0	0.0	80.0	0.0	40.0
ν_1	–	0.5	2.0	0.5	2.0	0.5	2.0
C_3	10^{-18}ster	–	–	–	–	10.0	100.0
$T_{0,2}$	1000K	–	–	–	–	0.5	1.0
τ_2	days	–	–	–	–	30.0	100.0
ν_2	–	–	–	–	–	0.5	2.0

other bands show a time lag behind those of the AD-dominated z band – except for the 5100 Å fluxes, which seem to be concurrent with the z-band fluxes – and this lag increases with wavelength. This band-dependent behavior can be explained with the reverberation delay of the hot dust, and the increasing dust contribution and decreasing AD contribution for longer wavelengths.

Figure 4.6 shows a single-epoch decomposition of the fluxes into AD and hot dust according to Eq. 2.2. The hot dust temperature closely follows the overplotted AD z-band flux (with a delay of $\approx$ 30 days), as expected.

The results of the multi-epoch multi-wavelength fit is shown in a temporal plot in Fig. 4.8 for the 1BB model and in Fig. 4.9 for the 2BB model. For the 1BB model, the best-fit lag is $\tau = 31.0 \pm 1.6$ days, and the best-fit value for the power-law slope is $\alpha = 1.63 \pm 0.04$ (see Table 4.5 for values of the other parameters), nicely matching the $F_\nu \propto \nu^{1/3}$ law expected from a standard Shakura-Sunyaev accretion disk. The initial blackbody temperature has a best-fit value of $T_0 = 1436 \pm 15$ K, and then evolves (by construction) as in Eq. 2.4. Epochs 1 and 2 are not included in the evaluation of the fit, as in the used model, T evolves only for $t \geq \tau$. A value of $\chi^2_{red} = 1.87$ is found for this fit, indicating that the measurement errors were either slightly underestimated, or that the model is too simple.

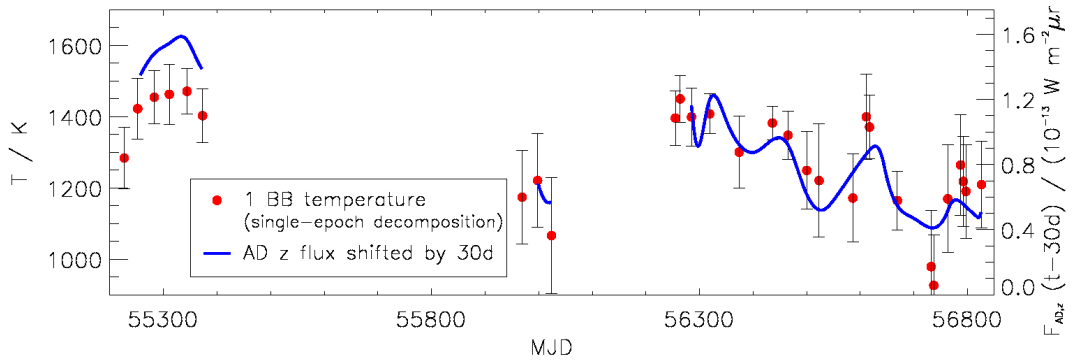

Figure 4.6: *Hot dust temperature evolution derived from the single-epoch decomposition. The hot dust temperature changes follow the relative AD z-band flux changes with a delay of roughly 30 days. The minimum that is seen in the temperature around MJD 56700 (and also in the corresponding JHK flux minima) is not covered within the sampling of the z-band data (see Fig. 4.8 and Fig. 4.2), therefore a substantial discrepancy is observed here. Comparing epochs 1-9 with epochs 10-29, one can see that the ratio $F_{AD,z}/T$ is higher in the first epochs, already indicating the later finding that in these early epochs the reverberation lag might be larger than in the later epochs, so that the AD flux is more diluted and the dust heated less in epochs 1-9.*

For the 2BB model, the best-fit values are $\tau_1 = 29.3 \pm 1.9$ days, $T_{0,1} = 1479 \pm 27$ K, $\tau_2 = 67.2 \pm 8.3$ days, $T_{0,2} = 698 \pm 64$ K, $\alpha = 1.65 \pm 0.04$, and a reduced χ^2 value of $\chi^2_{\rm red} = 1.89$ is found. Here, epochs 1-3 are not included into the fit, because T_2 evolves only for $t \geq \tau_2$. The best-fit values for the complete set of parameters are given in Table 4.5. For both the 1BB and the 2BB model, the data can be fit well with a stable time lag.

In Fig. 4.7, the results from the 1BB fit is shown in the spectral domain, for the epochs 3, 5, 9, and 10. It is clearly visible how the observed SED changes from epoch 3 to 5, and one can see a hot dust bump emerging, with the peak of the blackbody emission shifted to lower wavelengths ($\lambda \approx 1.9\mu$m), thus indicating the detected temperature increase. Though degeneracies between the blackbody constant and the blackbody temperature are non-negligible (in the single-epoch fits, where the temperature can evolve freely, the correlation coefficient is as large as ≈ -0.75), the visual inspection of the data and the systematic changes of the NIR color, correlating with the delayed AD brightness, underline the actual temperature increase. The hot dust peak is shifted to much longer wavelengths ($\lambda \approx 2.5\mu$m) in epoch 9, and until epoch 10, again rising temperatures are observed.

In Fig. 4.10, the marginalized posterior probability distributions are shown for the parameters C_2, T_0, τ, and α. As can be seen, C_2 and T_0 are strongly anti-correlated. However, any increase or decrease in C_2, and hence decrease or increase in T_0, will only shift the resulting temperature curve in vertical direction, due to the approach of Eq. 2.4. The significance of the temperature variations justifying this approach has already been shown with the single-epoch fits (Fig. 4.6), and can also be seen from the SEDs shown in Fig. 4.7.

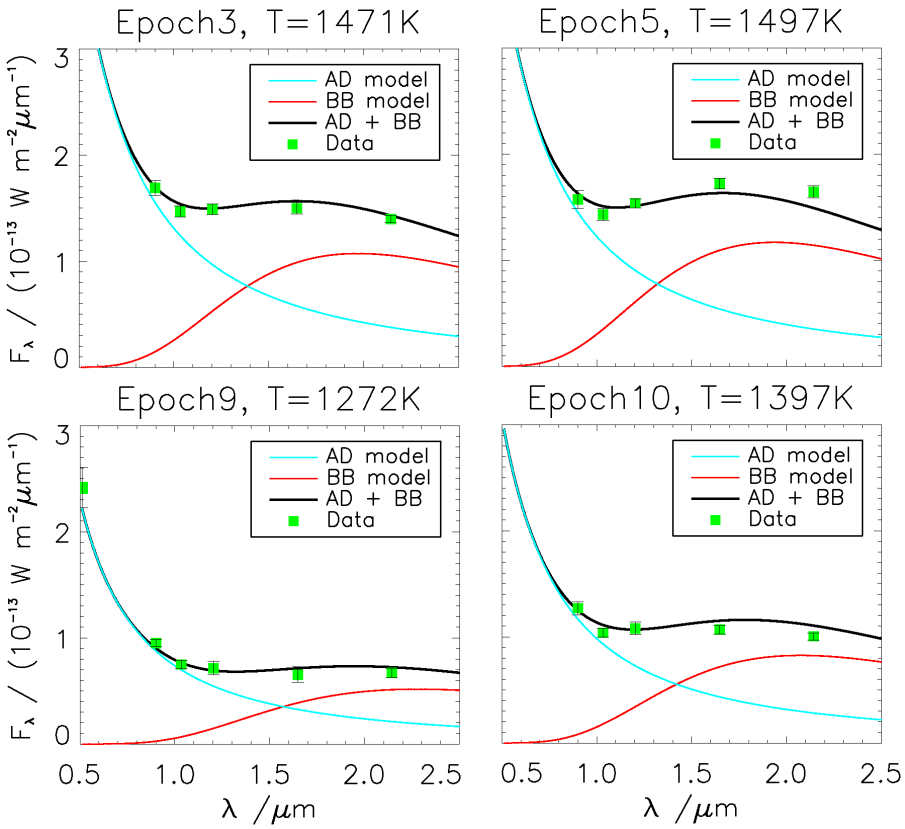

Figure 4.7: *NGC 4151 data and the 1BB model fit for the epochs 3, 5, 9, and 10. Overplotted is the AD model, the 1BB model, and the sum of both components. From the data, a clear rise in the blackbody flux is observed, and a clear shift of the blackbody emission peak to shorter wavelengths until epoch 5. This emerging bump is confirmed by the blackbody temperature maximum in epoch 5 of the single-epoch fit (see Fig. 4.6).*

The reverberation delay τ does not seem to show significant correlations with any other parameter, while α is slightly anti-correlated resp. correlated with C_2 resp. T_0. Interestingly, a multi-modal pdf of the reverberation lag τ is observed. This is on the one hand caused by slightly different reverberation delays in 2010 and 2013-2014 (see Sect. 4.5.3), but mainly by a strong bimodality in τ in the 2012-2014 part of the data set (epochs 7-29, see Fig. 4.14). As that second period dominates the fit due to a higher amount of data points and lower photometric errors, the bimodal pdf is also visible in the fit of the complete data set. This bimodality will be discussed in more detail in Sect. 4.5.3.

4.4.2 Further structure function models and time-variable power-law index

As described in Sect. 4.3, the robustness of all performed multi-epoch multi-wavelength fits using three different structure function models was tested. It turned out that the results are highly stable under the exchange of the structure function model or its particular pa-

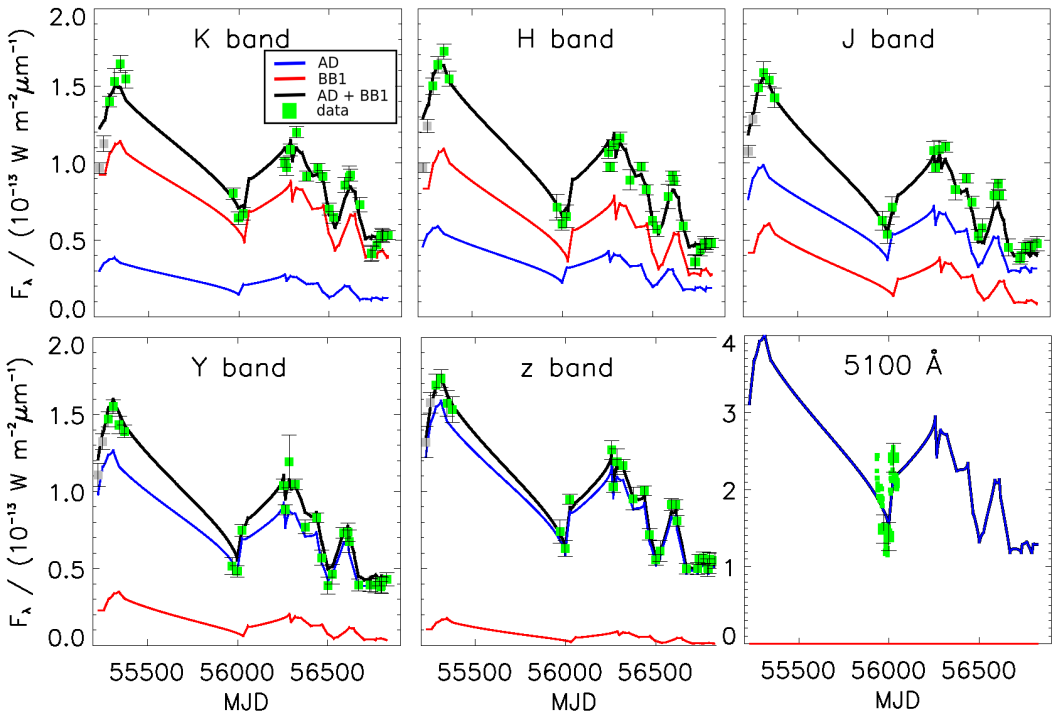

Figure 4.8: *Results of the 1BB model fit. Plotted are the K, H, J, Y, z, and 5100 Å data (green) over time. The bigger dots with errors bars in the 5100 Å panel mark the data points that coincide with the NIR epochs. The red line represents the blackbody contribution for each band, blue the AD contribution, and the black line is the sum of both. Note that epochs 1 and 2 are not included in the evaluation of the fit (as $t < \tau$).*

rameters. In Table 4.5, the results are only listed for the power-law model, while Table 4.7 shows the influence of the structure function on a subset of the results.

Further, the influence of the AD power-law slope α on the results was examined. As an alternative approach to keeping α fixed over the whole time and flux range, a varying α was allowed. As the continuum emission from the AD is found to get harder as the AD brightens (see e.g. Trèvese et al. (2001) and references therein), an alternative 1BB fit was performed allowing for a varying power-law slope of the form $\alpha_{\mathrm{var}}(t) = \alpha + \alpha_1 \cdot L_z(t)/\langle L_z(t)\rangle$. Best-fit values $\alpha = 1.56 \pm 0.07$ and $\alpha_1 = 0.10 \pm 0.07$ were obtained, while all other parameters stayed nearly the same (Table 4.6).

At this point, it should be noted that unfortunately the power-law slope is only well-determined in those epochs where also optical measurements were available (epochs 7-9). Thus, the applied approach of fitting a varying α to the data might be insufficient to determine the true variability range of the AD power-law slope. Therefore, published empirical relations between α and the AD luminosity were used as an alternative. According to Trèvese et al. (2001), who analyzed multi-epoch data of a sample of quasars, there is a

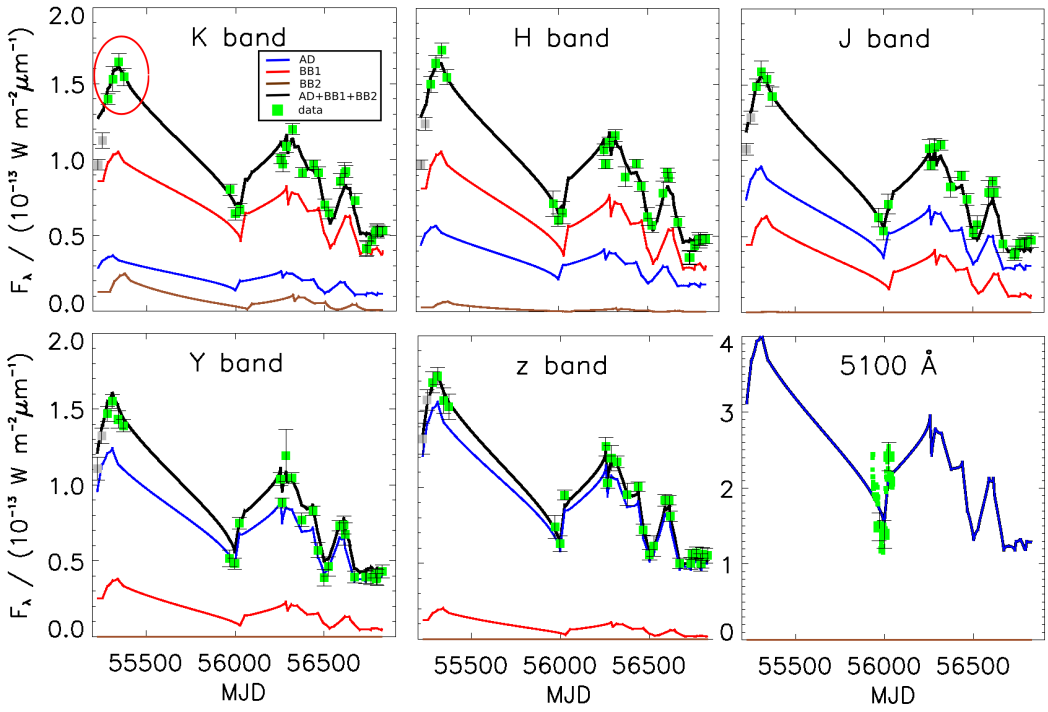

Figure 4.9: *Results of the 2BB model fit. Plotted are the K, H, J, Y, z, and 5100 Å data (green) over time. The bigger dots with error bars in the 5100 Å panel mark the data points that coincide with the NIR epochs. The red line represents the contribution of the inner blackbody component (at 29 light-days distance) for each band, the brown line is the second blackbody (at 67 light-days), blue the AD contribution, and the black line is the sum of all three components. Note that epochs 1, 2, and 3 are not included in the evaluation of the fit (as $t < \tau_2$). The resulting 2BB model fit only differs significantly from the 1BB model fit in the high-flux epochs 4-6, in the K band, as marked with a red circle.*

relation $\Delta\alpha = a + b\Delta(\log F_\nu)$ between the change of the spectral index and the logarithmic optical continuum flux change of the AD, with $a = -8.49 \pm 5.50 \cdot 10^{-2}$ and $b = 2.55 \pm 0.75$. Specifically for NGC 4151, Fanti et al. (1984) report the relation $\alpha = b \cdot \log F_\nu$ with $b \approx 4$. Making use of the inferred α values in epochs 7-9 and the flux differences of the z-band signal with respect to the z flux in these three epochs, the cited two models were applied for deriving an alternative, more representative evolution of α over the whole time and flux range. Thus, instead of fitting the evolution of α to the data, which may problematic because of the absence of optical data in most epochs, those two models were used as input for the fit. The results were found to be qualitatively robust under the use of these different models (also see Sect. 4.5.3), even though values as high as $\alpha \approx 3.3$ are reached in the high-flux epochs. The influence of the particular choice of α for a subset of the results is shown in Table 4.6.

Table 4.5: *Global mean and errors for the parameters of the various models, and reduced χ^2. The errors are given by $\Delta x = \sqrt{\hat{V}}$ for each parameter. All results shown here are derived from using the power-law structure function.*

Parameter	Unit	1BB	1BB (var. α)	1BB (ep. 1-9)	1BB (ep. 7-29)	2BB
C_1	–	0.78 ± 0.01	0.78 ± 0.01	0.78 ± 0.01	0.78 ± 0.01	0.77 ± 0.01
α	–	1.63 ± 0.04	1.56 ± 0.07	1.65 ± 0.07	1.63 ± 0.04	1.65 ± 0.04
α_1	–	–	0.10 ± 0.07	–	–	–
C_2	10^{-18}ster	3.82 ± 0.19	3.88 ± 0.20	4.63 ± 0.33	3.52 ± 0.22	3.16 ± 0.34
$T_{0,1}$	1000K	1.436 ± 0.015	1.436 ± 0.015	1.392 ± 0.020	1.455 ± 0.018	1.479 ± 0.027
τ_1	days	31.0 ± 1.6	30.8 ± 1.5	42.5 ± 4.0	29.6 ± 1.7	29.3 ± 1.9
ν_1	–	0.81 ± 0.02	0.82 ± 0.02	0.96 ± 0.04	0.81 ± 0.03	0.80 ± 0.02
C_3	10^{-18}ster	–	–	–	–	56.47 ± 25.65
$T_{0,2}$	1000K	–	–	–	–	0.698 ± 0.064
τ_2	days	–	–	–	–	67.2 ± 8.3
ν_2	–	–	–	–	–	1.26 ± 0.20
$\chi^2_{\rm red}$	–	1.87	1.87	1.13	1.76	1.89

4.5 Discussion

4.5.1 Single-blackbody model

As for the 2010 data of NGC 4151, a significant rise of the emission and temperature of the innermost hot dust is observed, following states of increased AD brightness. The hot dust temperature follows the AD flux with a time delay of roughly 31 days. This indicates that the hot dust in NGC 4151 currently observed is simply heated up by increased AD irradiation, and not destroyed due to sublimation. In case of significant dust destruction, one would expect an increase in the reverberation delay, which is not seen in the data. Obviously, the major part of the hot dust in the nucleus of NGC 4151 is not located at its current sublimation radius, but is cooler than sublimation temperature.

There are strong indications that the hot circumnuclear dust around AGNs mainly consists of large graphite grains ($\approx 0.2\mu$m grain size), with sublimation temperatures $\gtrsim$ 1500K (Gaskell et al., 2004; Kishimoto et al., 2007, 2011b). Since the inferred dust temperatures do not reach 1500K (see Fig. 4.6 and Fig. 4.13), it is expectable that no dust sublimation is seen in the data.

Limitations of the method are given by the z-band sampling, and thus the interpolation of the input AD signal – for instance, the minimum observed in JHK around MJD 56700, is missed in the z-band observations (and therefore in the interpolated AD signal), so the resulting model fits the JHK fluxes around MJD 56700 very poorly. Apart from this mismatch, the 1BB model already fits the data remarkably well within the errors. Only in the epochs 4-6 (i.e., spring 2010), the modeled K-band fluxes are systematically lower than the actually measured K-band peak fluxes.

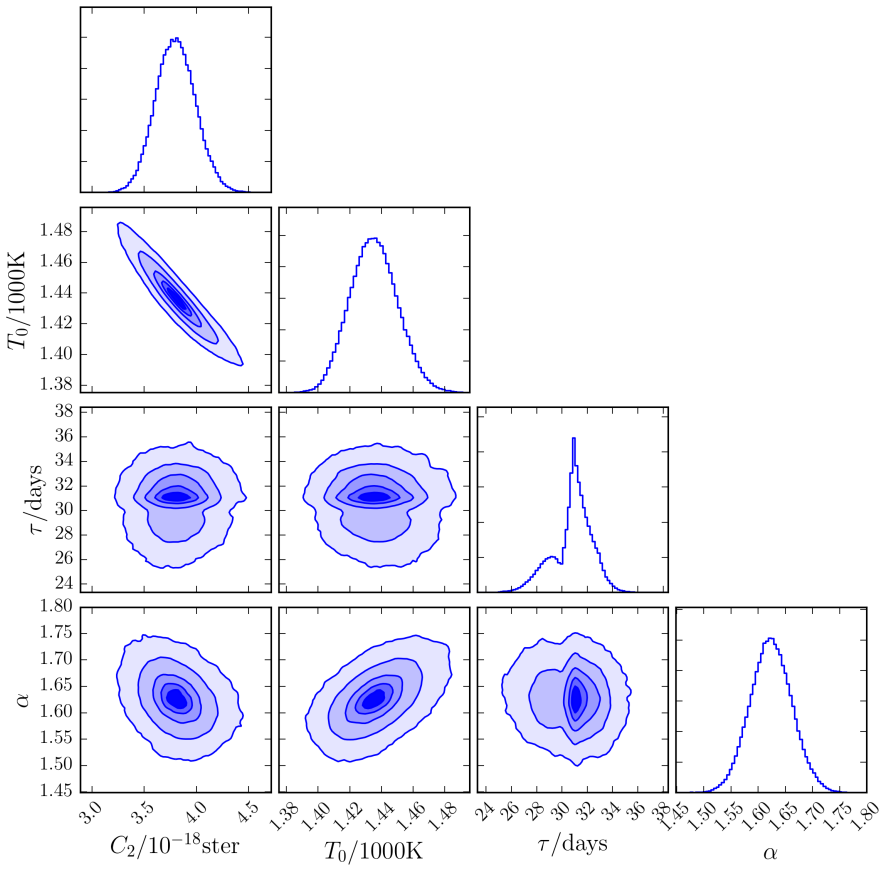

Figure 4.10: *Marginalized posterior probability distributions for the four parameters C_2, T_0, τ, and α of the 1BB model fit, with the 1-dimensional projections shown along the diagonal, and the 2-dimensional projections in the other panels. Contours mark the 10%, 25%, 50%, 85% and 99% confidence intervals.*

4.5.2 Two-blackbody model

In the 2BB model, epochs 4-6 are fit better, indicating that a second BB component might actually contribute significantly to the observed K-band flux. However, it should be pointed out that the goodness of the fit is not improved when using the 2BB model ($\chi^2_{\rm red}$=1.89) instead of the 1BB model ($\chi^2_{\rm red}$=1.87)). This is not surprising, as the weight of the few 2010 HK data points is low compared to the global data set.
In Sect. 3.5, it was already argued that the hot, NIR dust around NGC 4151 might be substantially radially extended and better represented by more than one blackbody component.

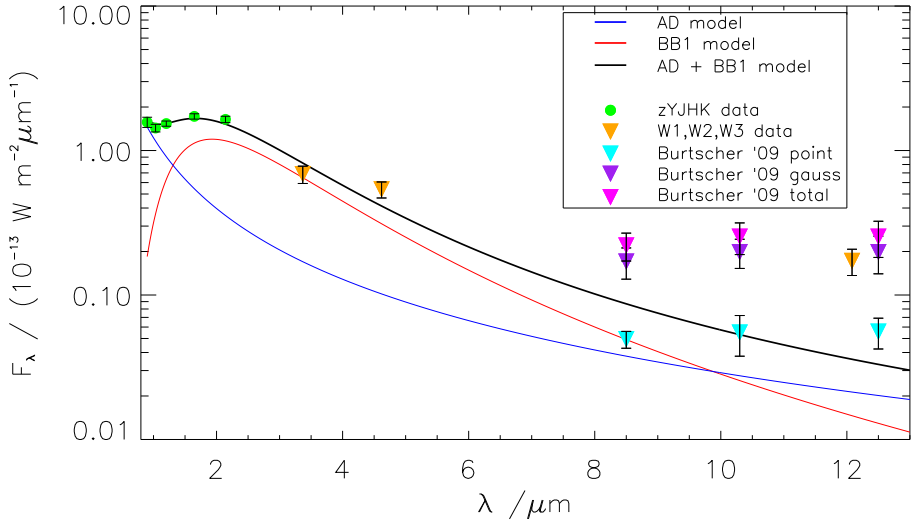

Figure 4.11: *Resulting fluxes from the 1BB model fit in the high temperature epoch 5, plotted over wavelength. Overplotted are the derived NIR and MIR fluxes (zYJHK and W1, W2, W3). The 1BB model roughly matches the MIR point source fluxes, given by Burtscher et al. (2009). As the model was fit to the zYJHK data only (also see Sect. 4.5.2), these are marked with green circles, while the other data are represented by triangles.*

However, when including data at longer wavelengths, i.e. the WISE W1-W3 bands, the 2BB model has to be rejected[2]. From Fig. 4.11 and Fig. 4.12, it becomes apparent that the fluxes are fit better with the 1BB model.

This finding agrees with the data of Burtscher et al. (2009). The unresolved point source that they measure with N-band interferometry, and which they attribute to the inner rim of the hot dust torus (at 0.04 - 0.05 pc $\approx$ 50 light-days), is apparently the same source that constitutes the observed NIR fluxes, as the observed Burtscher PS fluxes are consistent with the SED of the 1BB model (Fig. 4.11). In Fig. 4.11 and Fig. 4.12, the fluxes of an extended Gaussian source measured by Burtscher et al. (2009) are also overplotted, and the sum of both components (PS + Gaussian). The extended source is interpreted as the warm component of the clumpy torus located farther out, at 2.0 $\pm$ 0.4 pc $\approx$ 240 light-days. As this extended source is not resolved in the WISE photometry, it contributes to the WISE PSF flux of the W3 band (which matches the Burtscher total flux at 12.5 μm), while the W1 and W2 bands obviously show no significant warm dust contribution. A clear excess of the observed PS + Gaussian fluxes over the modeled 1BB fluxes can only be seen from the N band ($\lambda \geq 8\mu$m) on. Here, the single blackbody approximation is not sufficient anymore, but a second blackbody component contributes to, or even dominates, the measured fluxes. This is however not the 698 $\pm$ 64K blackbody component from the 2BB fit, but a blackbody of lower temperature ($T = 285^{+25}_{-50}$) that is located farther out (Burtscher et al., 2009). A

[2]The WISE data were not included into the χ^2 of the fit, as the aim was to test for an extended structure in the NIR regime up to the K band. Nevertheless, any resulting 2BB model would have to match the WISE fluxes as well.

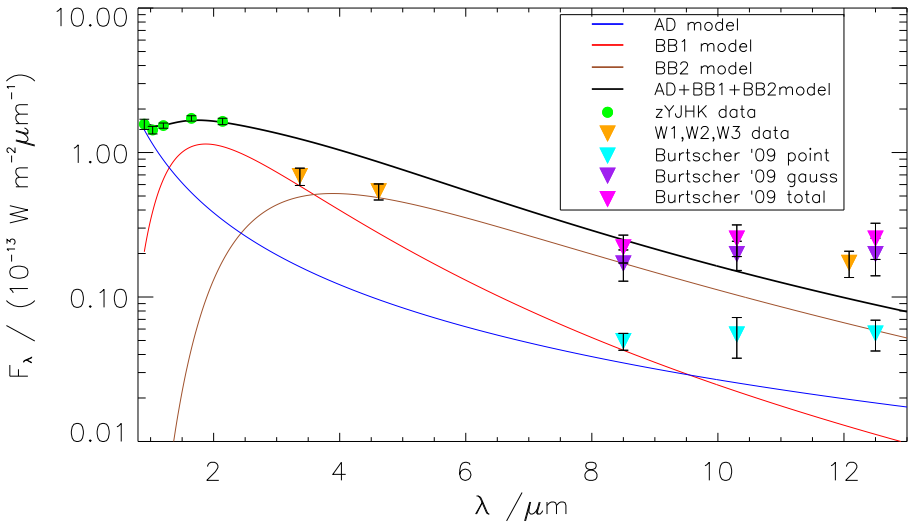

Figure 4.12: *Resulting fluxes from the 2BB model fit in the high temperature epoch 5, plotted over wavelength. Overplotted are the derived NIR and MIR fluxes (zYJHK and W1, W2, W3). While matching the observed HK fluxes better than the 1BB model, the 2BB model total fluxes exceed by far the WISE W1, W2 measurements. A second blackbody component inside of 100 days can be clearly rejected. Again, the model was fit to the zYJHK data only (marked with green circles, while the other data are represented by triangles).*

second blackbody component within 100 light-days distance from the source (which was set as an upper limit in the prior for τ_2, see caption of Table 4.4) is thereby clearly ruled out.

4.5.3 Variable time lag

Besides a second blackbody component contributing to the NIR fluxes, there might another explanation for the missed 2010 K-band peak by the fit. The resulting lag of $\tau_1 = 31.0 \pm 1.6$ days found for the 1BB model fits the global data very well. This holds for all data except for the K-band peak in epochs 4-6. Here, it looks as if the actual lag might still be a bit higher.

Table 4.6: *Global mean and errors for the parameters in the first period (epochs 1-9) and in the second period (epochs 7-29) for the 1BB model. The errors are given by $\Delta x = \sqrt{\hat{V}}$ for each parameter. In particular, the influence of the evolution of α (see Sect. 4.4.2) on the robustness of the results is shown. All results are shown for the power-law structure function model.*

Parameter	Unit	ep. 1-9 α =const	ep. 1-9 α (Trev. 2001)	ep. 1-9 α (Fan. 1984)	ep. 7-29 α =const	ep. 7-29 α (Trev. 2001)	ep. 7-29 α (Fan. 1984)
C_1	–	0.78 ± 0.01	0.75 ± 0.01	0.70 ± 0.01	0.78 ± 0.01	0.79 ± 0.01	0.77 ± 0.01
α	–	1.65 ± 0.07	–	–	1.63 ± 0.04	–	–
C_2	10^{-18}ster	4.63 ± 0.33	4.83 ± 0.43	4.42 ± 0.28	3.52 ± 0.22	3.80 ± 0.35	3.70 ± 0.21
$T_{0,1}$	1000K	1.392 ± 0.020	1.405 ± 0.036	1.451 ± 0.018	1.455 ± 0.018	1.463 ± 0.027	1.505 ± 0.039
τ_1	days	42.5 ± 4.0	36.5 ± 5.3	33.9 ± 4.2	29.6 ± 1.7	28.3 ± 2.8	25.9 ± 2.5
ν_1	–	0.96 ± 0.04	1.09 ± 0.04	1.15 ± 0.05	0.81 ± 0.03	1.03 ± 0.02	1.24 ± 0.04

If the data set is split into two subsets (set 1: epoch 1-9 (2010 - spring 2012 data), set 2: epochs 7-29 (2012 - 2014 data)[3]), one finds that the fitted hot dust reverberation delay is $\tau^{2010} = 42.5 \pm 4.0$ days if only epochs 1-9 are included (see Table 4.5 for the other parameter values of this fit), consistent with Hönig & Kishimoto (2011) and Kishimoto et al. (2011a). For the epoch 7-29 fit, the best-fit delay is $\tau^{2013} = 29.6 \pm 1.7$ days (also see Table 4.5). It has been checked and excluded that this decrease in τ is merely an effect of the improved sampling in the second period. The blackbody constant also changes between the two different fits, from $C_2^{2010} = 4.63 \pm 0.33$ to $C_2^{2013} = 3.52 \pm 0.22$, and the initial temperature from $T_0^{2010} = 1392 \pm 20$K to $T_0^{2013} = 1455 \pm 18$K. Note, however, that T_0^{2013} refers to the initial temperature in epoch 1 and hence has no real physical meaning for the second period fit of epochs 7-29. See Fig. 4.13 for the resulting temperature evolution of this fit. Interestingly, while all other parameters stay nearly the same, also the variability factor changes between the two fits, from $\nu^{2010} = 0.96 \pm 0.04$ to $\nu^{2013} = 0.81 \pm 0.03$, which might indicate that the AD illumination is less efficiently reprocessed by the hot dust in the second period.

As discussed in Sect. 4.4.2, the influence of different structure function models and different evolutions of the AD power-law index α on the results was examined. It seems particularly important to test the robustness of the apparent decrease in the reverberation lag under the different models. While for the global 1BB model which includes all epochs, the parameter values are very insensitive to the different models and model parameters, the parameters inferred for the epoch 1-9 fit and epoch 7-29 fit do undergo certain changes when applying the different structure functions and α models. The influence of α is shown in Table 4.6, while the influence of the various structure function models on the results are shown in Table 4.7. One can see a change in the derived absolute parameter values, especially the time lag seems to be sensitive to the applied variability model of α. Nevertheless, relative to each other, the inferred lags for the epoch 1-9 fit and the epoch 7-29 and the decrease in the delay, remain unchanged. While for a constant α (and different structure functions), the lag decreases from $\tau^{2010} \approx 43$ days to $\tau^{2013} \approx 30$ days, the values $\tau^{2010} \approx 37$ days, $\tau^{2013} \approx 28$ days are found using the model according to Trèvese et al. (2001), and $\tau^{2010} \approx 34$ days, $\tau^{2013} \approx 26$ using the one presented by Fanti et al. (1984). Thus, qualitatively the results are unaltered: a significant decrease in the reverberation delay from 2010 to 2013-2014 is seen.

In Fig. 4.13, the temperature evolution resulting from the epoch 1-9 and epoch 7-29 fits is plotted versus the temperature from the single-epoch decomposition (Eq. 2.2). Naively one would expect that due to the decreased AD radiation by 50% on average from 2010 to end of 2012-2014 ($\langle L_z \rangle^{2013} / \langle L_z \rangle^{2010} \approx 0.49$), the blackbody temperature would have decreased by a factor $0.5^{1/4} \approx 0.84$ following $L \propto T^4$. This temperature decrease due to the dimmer AD would be roughly balanced by a temperature increase due to a new dust location further inside by a factor of $\sqrt{\tau^{2010}/\tau^{2013}} \approx 1.18$. Thus, one would expect the

[3]The whole data set was split into these two overlapping data sets because, while it was obvious that the delay in epochs 1-6 would be larger than the delay in epochs 10-29, a priori the delay of epochs 7-9 was not apparent, as fitting only 3 epochs is rather ambiguous.

Table 4.7: *Global mean and errors for the parameters in the first period (epochs 1-9) and in the second period (epochs 7-29) for the 1BB model. The errors are given by* $\Delta x = \sqrt{\hat{V}}$ *for each parameter. In particular, the influence of different structure function models discussed in Sect. 4.3 on the results is shown. Here, DRW1 refers to the damped random walk model with* σ*=0.15 and* τ*=230, DRW2 to the damped random walk model with* σ*=0.03 and* τ*=10. All results are shown for constant* α*.*

Parameter	Unit	ep. 1-9 power-law	ep. 1-9 DRW1	ep. 1-9 DRW2	ep. 7-29 power-law	ep. 7-29 DRW1	ep. 7-29 DRW2
C_1	–	0.78 ± 0.01	0.78 ± 0.01	0.78 ± 0.01	0.78 ± 0.01	0.78 ± 0.01	0.78 ± 0.01
α	–	1.65 ± 0.07	1.65 ± 0.08	1.65 ± 0.08	1.63 ± 0.04	1.64 ± 0.06	1.64 ± 0.05
C_2	10^{-18}ster	4.63 ± 0.33	4.66 ± 0.35	4.67 ± 0.36	3.52 ± 0.22	3.55 ± 0.34	3.55 ± 0.32
$T_{0,1}$	1000K	1.392 ± 0.020	1.393 ± 0.027	1.389 ± 0.026	1.455 ± 0.018	1.449 ± 0.017	1.443 ± 0.019
τ_1	days	42.5 ± 4.0	42.4 ± 4.6	42.2 ± 4.4	29.6 ± 1.7	30.1 ± 2.1	30.2 ± 2.0
ν_1	–	0.96 ± 0.04	0.91 ± 0.03	0.91 ± 0.04	0.81 ± 0.03	0.77 ± 0.03	0.76 ± 0.03

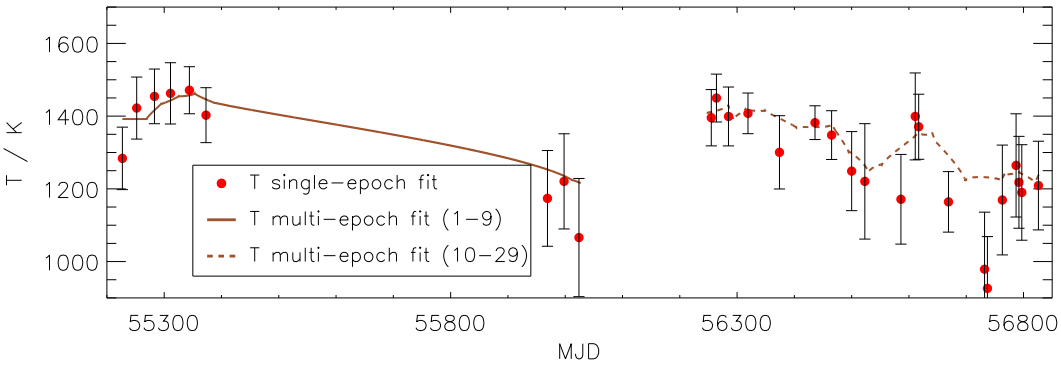

Figure 4.13: *Hot dust temperature* $T_{\rm single}$ *derived from the single-epoch decomposition, where T is a free parameter in each epoch, versus the temperature* $T_{\rm multi}$ *from the multi-epoch fits, in which T evolves according to Eq. 2.4 and only the initial temperature* T_0 *is a free parameter. For epochs 1-9, the temperature resulting from the epoch 1-9 fit is plotted, for epochs 10-29 the temperature from the epoch 7-29 fit. The minimum that is seen in* $T_{\rm single}$ *around MJD 56700 (and also in the corresponding JHK flux minima) is not covered within the sampling of the z-band data (see Fig. 4.8 and Fig. 4.2), therefore a substantial discrepancy between* $T_{\rm single}$ *and* $T_{\rm multi}$ *is observed around that date.*

blackbody temperature for 2010 to be on the same average level as in end of 2012-2014.

Nevertheless, one observes a decreased average temperature in the second part of the data set ($\langle T\rangle^{2013}/\langle T\rangle^{2010} \approx 0.86$), in the single-epoch fits. This is confirmed by the temperature curve of the multi-epoch fit for epochs 7-29, and achieved through a lower variability factor, with $\nu^{2013}/\nu^{2010} \approx 0.84$. Obviously, in the second part of the data set, the dust is heated less efficiently by the AD radiation estimated from the z-band flux.

Physical reasons of this could be an increase in dust grain size, or a geometrical cause. In a model proposed by Czerny & Hryniewicz (2011), the dust clouds resulting from an AD wind only become exposed to the AD radiation in the process of moving farther outside, as dust that is still located farther inside tends to have a small height above the disk, whereas the dust further outside has a larger height. The innermost dust would then be heated less

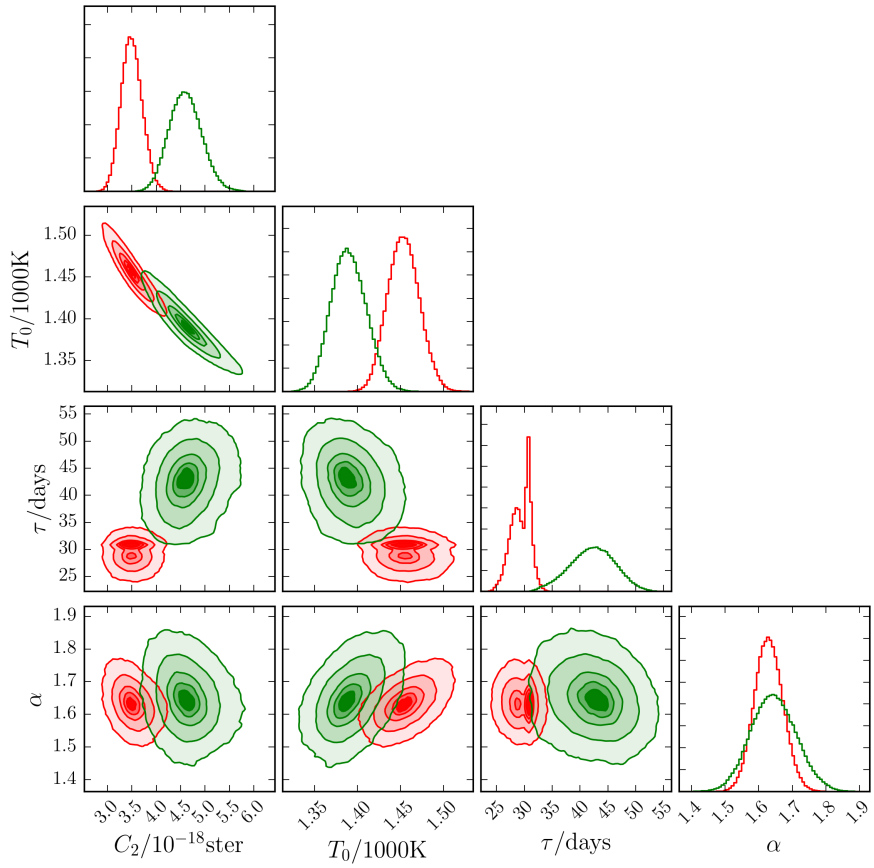

Figure 4.14: *Marginalized posterior probability distributions for the four parameters C_2, T_0, τ, and α of the 1BB model fit, for the first part of the data set (epochs 1-9) in green and the second part (epochs 7-29) in red. The 1-dimensional projections are shown along the diagonal, and the 2-dimensional projections in the other panels.*

efficiently assuming an anisotropic radiation characteristic of the AD. The discussed parameter changes between the two periods might point to a changed dust distribution.

In Fig. 4.14, the marginalized posterior probability distributions of the parameters C_2, T_0, τ, and α are shown for the epoch 1-9 fit (green) and the epoch 7-29 fit (red). Clearly, a significantly decreased reverberation lag is seen, from $\tau^{2010} = 42.5 \pm 4.0$ in 2010 to $\tau^{2013} = 29.6 \pm 1.7$ in 2012-2014. As already mentioned in Sect. 4.4, the pdf of τ^{2013} is bimodal. Interestingly, no bimodality is observed for τ^{2010}. Here, the pdf of seems perfectly unimodal. Possibly, the bimodality is washed out by the higher photometric errors in the first period, or this missing bimodality in period 1 versus the observed bimodality in period 2 points to a changed dust distribution as well. In support of this, increasing the errors in the second period to the level of the epoch 1-9 errors, only slightly washes out the bimodality but does not make the it vanish completely. Further, it has been checked and

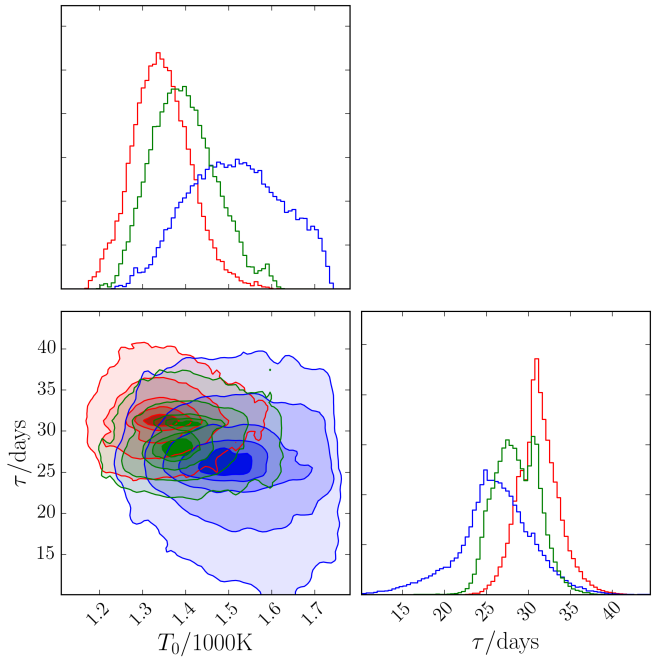

Figure 4.15: *Marginalized posterior probability distributions for the parameters T_0 and τ of the epoch 7-29 1BB model fit, obtained by fitting the J, H, and K bands separately (also see text of this Section). The J-band fit is shown in blue, H band in green, and K band in red. The 1-dimensional projections of the pdfs are shown along the diagonal, and the 2-dimensional projections in the other panel. While the two-dimensional projections are hard to disentangle by the eye, in the right panel one can nicely see an "inflection point" of the two different reverberation delays around $\tau \approx 30$ days. Also note the fitted blackbody temperature T_0 in the upper panel rising from K to H to J.*

excluded that the detected bimodality in epochs 1-9 in contrast to the missing bimodality in epochs 7-29 is merely due to the improved sampling in the second period. This supports the supposition that a changed dust distribution is seen in the second period.

The resolved bimodality in τ^{2013} is caused by slightly different delays for the bands JHK (constituting the blackbody emission), as confirmed by performing separate fits for each band[4], i.e. $\tau_J^{2013} = 26.1 \pm 4.8$, $\tau_H^{2013} = 28.9 \pm 2.6$ and $\tau_K^{2013} = 31.4 \pm 2.4$, pointing to a slight radial extent of the innermost dust within a narrow region around τ^{2013}. Interestingly, one observes not just a smoothly extended structure, but at least two separate blackbodies at two discrete, nearby, but different radii. This feature is visible in Fig. 4.15, especially in the H band. Here, the pdf peaks at two different delays, $\tau_{\mathrm{inner}} \approx 26$ days and $\tau_{\mathrm{outer}} \approx 31$ days. In the K band, τ_{outer} dominates the pdf, while τ_{inner} is slightly visible as well. In the J band, the pdf is clearly dominated by the shorter lag, while the longer lag can only be marginally "resolved" due to a slight asymmetry in the pdf. Note that the intersection point between the pdfs of the two different delays always occurs at $\tau \approx 30$ days, for all

[4] C_1, α and ν were fixed to their best-fit values of the epoch 7-29 fit for these single-band fits, to avoid too high degeneracies between the parameters.

three bands, and H and K even exhibit a minimum there. As expected, the fitted blackbody temperatures of the three bands decrease with wavelength, from $T_{0,J}^{2013} = 1521 \pm 105$K to $T_{0,H}^{2013} = 1392 \pm 74$K, and $T_{0,K}^{2013} = 1351 \pm 102$K. Due to missing color information in the single-band fits, the degeneracies between T_0 and C_2 are extremely high, so the fitted temperatures should not be taken too seriously. The delay τ for each band, however, is not influenced by degeneracies with any other parameter. The detected 2BB structure within a narrow range around τ^{2013} does not contradict the result of the previous 2BB model fit, which was mainly performed to test for a significantly radially extended dust distribution rather than a compact distribution. The two distinct blackbodies resolved within the epoch 7-29 fit, still represent a rather compact dust distribution, as they are very close, and are therefore not in conflict with the finding from the 2BB model fit.

The results indicate a decreased time delay from 2010 (MJD 55300-55400) to 2012-2013 (MJD 56000-56300). This stands in strong contrast to interferometric observations by Kishimoto et al. (2013), who measured an increased delay, from roughly 40-50 days in 2010 to 70-80 days in spring 2012 – a delay that is clearly not consistent with the data presented here.

The shift in time lag seems to imply that the dust radius has indeed decreased by inflow of dust from outside due to the low luminosity state of the AD and thereby decreased dust sublimation radius. Alternatively, BLR clouds could have been launched from farther inside due to decreased AD luminosity.

Dust condensation only occurs when the clouds have expanded to roughly three times their initial radius, which happens at a distance $d \approx 1000 \cdot d_0$, with d_0 being the initial distance of the clouds from the source (Elvis et al., 2002). Dust condensation would set in after roughly $3-9$ years from the initial launching of the clouds. Interestingly, the measured decrease in time lag seems to continue the decline from $\tau \approx 60$ days observed end of 2008 (Pott et al., 2010) to $\tau \approx 50-45$ days in 2009/2010 (Kishimoto et al., 2009, 2011a). This total decrease in τ from 2008-2012 seems to track a decline in the AD flux from 2003 until 2006 with a delay of roughly 5-6 years (see Fig. 3 in Kishimoto et al. (2013), perfectly matching the timescale expected within the accretion wind scenario.

An upper limit for the infall velocity of dust produced by stars, which is moving in from outside, is the free fall velocity $v_{\rm free} = \sqrt{2GM/R_{\rm dust}}$ onto the central black hole ($M_{\rm BH} \approx 4.6 \cdot 10^7 M_{\rm Sun}$, Bentz et al. 2006). An infall velocity of $v_{\rm free} \approx 0.01c$ is obtained at the location of the hot dust torus. It would thus take $\gtrsim 1300$ days to decrease the dust radius from 43 to 30 days. This time span seems only marginally possible within the observations. Although these qualitative arguments seem to favor the accretion wind scenario over the inflow model, it must be noted that detailed modeling of the different scenarios is needed to reliably conclude on the dust formation mechanism in AGNs.

4.6 Conclusions

Updated results from the 2010-2014 NGC 4151 photometric and spectroscopic data were presented, which are part of the AGN hot dust reverberation project to monitor the evolution of the hot dust temperature and reverberation lag around AGNs. The findings for NGC 4151 are:

- Dust sublimation: If dust sublimation occurred in response to increased AD flux, it would happen at the inner edge of the dust distribution, thereby increasing the time delay. Although the AD brightness increased substantially within the observed time range, one can see no signatures of dust sublimation traced by the data. In particular, after detected AD flux increases by more than 30% in 2010, and by roughly 100 % from spring 2012 to fall 2012, no increase in the hot dust reverberation delay is found, thus ruling out significant dust destruction for the time range 2010-2014. It seems that the hot dust in this galaxy is currently located beyond its sublimation radius.

- Dust temperature: The hot dust emission, and moreover, the host dust temperature in NGC 4151 closely tracks the AD flux variations on a short-term response timescale, which is roughly 1 month on average. Maximum hot dust temperatures lower than 1500 K are measured throughout 2010-2014. The large graphite dust grains that are typically assumed for the hot circumnuclear dust around AGNs, have a sublimation temperature of $T_{\rm sub} \gtrsim 1500K$. It thus seems perfectly consistent that no dust sublimation is seen in the observed period.

- Dust distribution radius: On a long-term timescale, a change of the hot dust reverberation delay of ≈13 days in 2 years is measured. Detailed comparison of these results with seemingly comparable interferometric experiments reveals different variations of the derived dust radii. These apparent observational inconsistencies could imply that the real dust distribution in NGC 4151 is rather complex, so that the comparison of hot dust radii measured with interferometry and reverberation is not straightforward.

- Dust distribution: In the 2010 data, slight indications for a second blackbody component of ≈ 700K were seen, which could not be confirmed without broader wavelength coverage. Here, a new analysis was presented, now including WISE photometry, which rules out significant thermal radiation at 700K from radii smaller than 100 days.

To sum up, a decreased reverberation radius of the hot, circumnuclear dust in NGC 4151 is found. Dust destruction in the observed epoch seems highly improbable from the data, however a slight change of the dust morphology seems likely. While the observed decrease in the reverberation delay perfectly matches the timescale expected within the accretion wind scenario, a radius decrease due to the inward motion of dust from outside seems only marginally possible, as estimated from an upper limit for the infall velocity of dust produced by stars (see Sect. 4.5.3). From this analysis, new dust formation in a cooling BLR wind

appears to be more likely than a radius decrease due to inflow. It must be emphasized, however, that detailed modeling is indispensable to reliably discriminate between the different dust formation scenarios in AGNs.

5 NGC 3227 and GROND sub-sample

This chapter is based on the publication "AGN hot dust reverberation campaign III. – Modeling dust sublimation in the nucleus of NGC 3227" by Schnülle et al., which is close to submission to A & A (Schnülle & et al., 2017).
In this third project, 23 additional type 1 AGNs have been observed (Sect. 5.2) with the GROND camera (Sect. 2.3.1), and three of these, in addition to the Omega 2000 target NGC 4151, have been analyzed with the methods presented in Chapter 2. For the targets Ark 120 and NGC 5548 an analysis similar to NGC 4151 was applied, using the standard reverberation model without dust sublimation presented in Sect. 2.2.1. For the target NGC 3227, however, the standard reverberation model was found to be insufficient to fit the data, and the approach of Sect. 2.2.2 was developed and applied.

5.1 Introduction

In unified AGN models, a clumpy torus of dust is located around the outer edge of the BLR, with the innermost hot dust accumulating at or close to the sublimation radius of the high-luminosity state of the central engine. Due to intrinsic variability of the accretion disk irradiation, dust sublimation is an inevitable consequence whenever the current sublimation radius extends beyond the location of the innermost hot dust clouds for significantly longer than the sublimation timescale.

Reverberation measurements of the hot circum-nuclear dust in 24 type 1 AGNs are used, in order to monitor its temperature and reverberation lag as a function of the varying accretion disk brightness, and to analyze the evolution and long-term stability of toroidal circumnuclear dust distributions in AGNs. Multi-band multi-epoch photometry of NGC 3227 and 23 other type-1 AGNs have been accumulated in optical and NIR bands over four years. Thereof, 23 targets have been observed with the GROND camera, and one target – NGC 4151 – with Omega 2000. The results on NGC 4151 have been shown in Chapters 3 and 4. Here, mainly the results of NGC 3227, Ark 120, NGC 5548 are presented, concentrating on NGC 3227.

While generally, it is found in the presented NGC 3227 data that the hot dust flux and temperature closely track the accretion disk luminosity variations, the data show at some times a striking discrepancy between the optical and NIR variability signals. Specifically, the NIR light-curves do not rise as steeply and not to the same level as the optical light-curves. This missing flux in the hot dust response is interpreted as dust destruction due to sublimation. It is shown that a heuristic model with a minimum number of parameters, as presented in Sect. 2.2.2, is capable of successfully describing such sublimation events in multi-epoch

reverberation data sets and of estimating the dust re-illumination time-scales involved. The presented analysis can help decreasing the scatter in dust radius measurements due to removing the strict coupling of the location of the innermost dust clouds with the sublimation radius.

Information on the complete GROND AGN sample is presented in Sect. 5.2. This chapter is focused on NGC 3227 (Sect. 5.3), while summarizing the analyses of Ark 120 and NGC 5548 in Sect. 5.4, and presenting a sub-sample analysis of the four so-far analyzed targets in Sect. 5.5. Conclusions are given in Sect. 5.6.

5.2 The complete GROND AGN hot dust reverberation sample

Table 5.1: *The sample of 23 type 1 AGN observed with GROND within this work. Col. (4)-(7) are taken from Véron-Cetty & Véron (2010), Col. (8) from 2MASS. The expected delay $\tau_{\rm exp}$ is given in Col. (9).*

Target	RA (J2000)	DEC (J2000)	z	Class	$M_{\rm abs}$	m_V	m_J	$\tau_{\rm exp}$/days
Mrk590	02 14 33.564	-00 46 00.26	0.027	S1.0	-20.8	13.8	12.4	109
NGC1019	02 38 27.426	+01 54 27.72	0.024	S1.5	-19.3	15.0	13.7	55
IC 355	03 53 46.246	+19 58 26.16	0.029	S1.0	-20.0	15.4	13.7	76
UGC 3223	04 59 09.407	+04 58 30.35	0.018	S1.5	-19.0	14.4	13.3	47
MCG-01.13.025	04 51 41.518	-03 48 33.71	0.013	S1.2	-18.6	14.2	12.8	40
Ark120	05 16 11.407	-00 08 59.22	0.033	S1.0	-21.4	13.9	12.0	143
ESO362-G18	05 19 35.813	-32 39 27.81	0.013	S1.5	-19.7	13.4	12.5	65
H 0557-385	05 58 02.057	-38 20 04.43	0.034	S1.2	-19.8	15.0	12.3	69
Mrk704	09 18 25.999	+16 18 19.70	0.029	S1.2	-20.6	14.2	12.7	100
NGC3227	10 23 30.571	+19 51 54.30	0.003	S1.5	-17.9	11.8	11.3	29
ESO377-G24	11 12 33.348	-36 25 32.70	0.010	S1.0	-19.1	13.1	12.9	50
NGC3783	11 39 01.711	-37 44 18.98	0.009	S1.5	-18.7	13.4	12.0	41
NGC4235	12 17 09.880	+07 11 29.63	0.007	S1.2	-17.7	13.6	12.5	26
Mrk50	12 23 24.128	+02 40 44.54	0.023	S1.2	-17.7	16.6	14.1	26
3C 273	12 29 06.695	+02 03 08.59	0.158	S1.0	-26.2	12.9	11.8	1310
HE1228+013	12 30 50.037	+01 15 22.60	0.118	S1n	-24.1	14.4	13.7	498
NGC4593	12 39 39.455	-05 20 39.02	0.009	S1.0	-18.7	13.2	12.0	41
ESO 323-G77	13 06 26.115	-40 24 52.63	0.015	S1.2	-19.6	13.4	11.5	62
ESO 383-G035	13 35 53.767	-34 17 44.23	0.008	S1.5	-18.1	13.6	12.2	32
CTSJ13.12	13 51 29.507	-18 13 46.44	0.012	S1n	-18.0	15.5	13.4	30
NGC5548	14 17 59.554	+25 08 12.63	0.017	S1.5	-19.9	13.7	11.8	72
Fairall51	18 44 53.991	-62 21 52.83	0.014	S1.5	-19.0	14.1	12.3	47
H 2107-097	21 09 09.972	-09 40 14.65	0.027	S1.2	-20.4	14.4	12.9	91

Within this thesis, optical and NIR multi-band photometric observations of a total of 23 type 1 AGNs with the GROND camera (Sect. 2.3.1) have been planned and carried out, as presented in Table 5.1. The observations were performed from 2012 October - 2016 March, in service mode. While six of the targets were observed already from 2012 October on, monitoring of most targets started in 2014 May. The scheduled mean sampling interval was roughly 2 - 4 weeks for most of the targets (except for substantial data gaps whenever

the targets were not observable from La Silla), depending on their luminosity and thus their expected hot dust reverberation lag. Before the start of the monitoring campaign of the broad AGN sample (2014 May), the targets were carefully selected, taking into account the following criteria:

- The targets should show indications for the existence of hot dust in their SEDs, to avoid that they are among the 15% of hot-dust-poor AGNs.
- After estimating the expected lag time (from the absolute magnitude according to Col. (6) and the reverberation lag of NGC 4151 ($M_{\rm abs} = -18.0$, $\tau \approx 30$ days (see Chapter 4)) between AD and hot dust, preference was given to targets showing an expected lag between 30 and 150 days. With the exception of the bright-end targets HE 1228+013 and 3C 273, an upper limit for the expected time lag was set to 150 days, in order to be able to observe the lag in a 1 - 2 semester period and to reliably monitor the dust response within a reasonable amount of time.
- Further, only targets that are observable from La Silla for a minimum of 6 months per year were selected, in order to not allow for too large gaps in the data.

5.3 NGC 3227

5.3.1 The galaxy NGC 3227

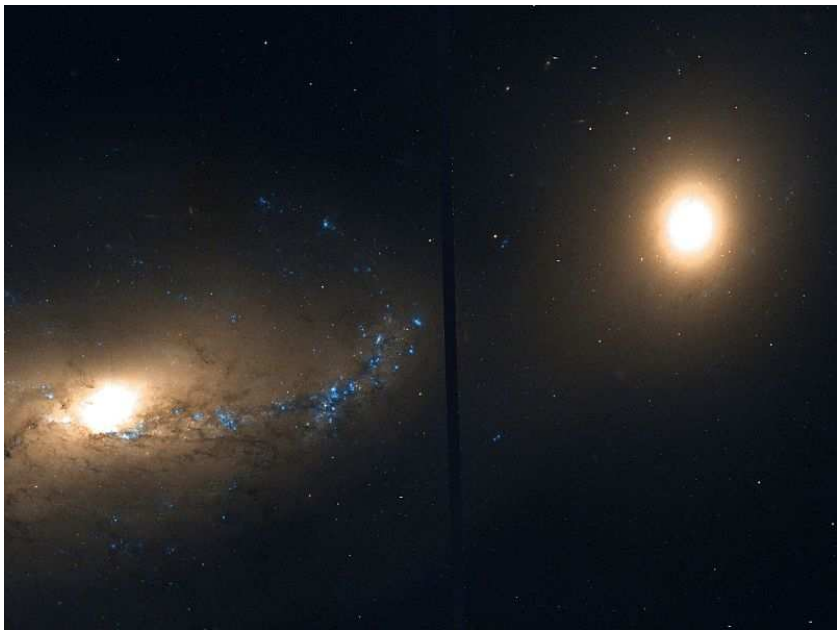

Figure 5.1: *A Hubble Space Telescope image of the Seyfert 1 galaxy NGC 3227 (Credit: NASA).*

Like NGC 4151, NGC 3227 is an intermediate spiral galaxy (SAB), and was discovered by William Herschel on February 14 in the year 1784. It is located at a right ascension

α = 10h 23m 30.6s and declination $\delta = +19°\ 51'\ 56''$ in the constellation Leo, and it is listed in the Atlas of Peculiar Galaxies for its interaction with the dwarf elliptical galaxy NGC 3226. The apparent magnitude of NGC 3227 in the V band is $m_V = 11.79$ mag, and it has an absolute magnitude of $M_V = -17.9$ mag (Véron-Cetty & Véron, 2010). NGC 3227 is a nearby galaxy with a redshift of $z = 0.003$. Its major diameter is 5.4', and its minor diameter 3.6'. An image of NGC 3227 is shown in Fig. 5.1. The luminosity of the nucleus reached a maximum in 1977, probably due to massive long-lived one-sided or two-sided streams of gas that were observed.

5.3.2 Observations

Table 5.2: *NIR fluxes of the nucleus of NGC 3227, derived with* `GALFIT`. *On some observation dates, fluxes are not available in all seven bands. No $g'r'i'z'$ fluxes were used for this analysis for 2013 Feb 21, as the AGN was located on the intersection of the two detector halves, resulting in a highly distorted psf, so that almost all of the AGN flux was attributed to the bulge component due to PSF mismatch. On 2013 Jun 02, there are no $i'z'$ fluxes due to problems with the right half of the i' and z' detectors. Fluxes in JHK were omitted from this analysis for 2014 Mar 30 due to saturation of the AGN in the NIR bands.*

Epoch	Date	MJD	F_λ / $10^{-13} W\,m^{-2}\,\mu m^{-1}$						
			g'	r'	i'	z'	J	H	K
1	2012 Nov 20	56252	2.21 ± 0.14	1.41 ± 0.07	0.91 ± 0.10	0.76 ± 0.13	0.69 ± 0.12	0.52 ± 0.05	0.39 ± 0.03
2	2012 Dec 04	56266	2.73 ± 0.48	1.84 ± 0.27	1.12 ± 0.16	0.84 ± 0.19	0.72 ± 0.06	0.50 ± 0.03	0.40 ± 0.02
3	2013 Feb 21	56345	–	–	–	–	0.78 ± 0.05	0.64 ± 0.04	0.46 ± 0.03
4	2013 Feb 28	56352	3.57 ± 0.24	2.18 ± 0.05	1.36 ± 0.09	1.00 ± 0.13	0.77 ± 0.04	0.61 ± 0.03	0.45 ± 0.03
5	2013 Apr 11	56394	3.00 ± 0.10	1.98 ± 0.06	1.26 ± 0.14	0.97 ± 0.12	0.75 ± 0.09	0.55 ± 0.04	0.46 ± 0.03
6	2013 Apr 28	56411	3.72 ± 0.13	2.30 ± 0.10	1.62 ± 0.19	1.11 ± 0.07	0.73 ± 0.03	0.53 ± 0.03	0.42 ± 0.02
7	2013 Jun 02	56446	3.27 ± 0.13	1.93 ± 0.15	–	–	0.67 ± 0.07	0.52 ± 0.05	0.41 ± 0.02
8	2013 Dec 06	56633	2.50 ± 0.18	1.63 ± 0.14	1.02 ± 0.05	0.76 ± 0.04	0.63 ± 0.04	0.50 ± 0.04	0.37 ± 0.03
9	2013 Dec 24	56651	2.50 ± 0.30	1.58 ± 0.18	1.03 ± 0.07	0.76 ± 0.05	0.68 ± 0.04	0.46 ± 0.02	0.33 ± 0.04
10	2014 Feb 05	56693	3.17 ± 0.19	1.92 ± 0.16	1.24 ± 0.06	0.92 ± 0.03	0.72 ± 0.04	0.55 ± 0.05	0.39 ± 0.03
11	2014 Feb 22	56710	2.65 ± 1.31	1.64 ± 0.87	1.02 ± 0.43	0.80 ± 0.20	0.78 ± 0.03	0.53 ± 0.05	0.46 ± 0.03
12	2014 Mar 30	56746	3.32 ± 0.07	2.05 ± 0.05	1.31 ± 0.05	0.98 ± 0.06	–	–	–
13	2014 May 12	56789	2.56 ± 0.11	1.59 ± 0.06	1.04 ± 0.05	0.86 ± 0.03	0.80 ± 0.10	0.59 ± 0.03	0.47 ± 0.04
14	2014 Dec 09	57000	2.44 ± 0.29	1.51 ± 0.21	0.94 ± 0.11	0.79 ± 0.11	0.73 ± 0.06	0.51 ± 0.04	0.40 ± 0.03
15	2014 Dec 21	57012	1.94 ± 0.31	1.23 ± 0.17	0.80 ± 0.20	0.68 ± 0.12	0.65 ± 0.23	0.53 ± 0.06	0.39 ± 0.02
16	2015 Jan 29	57051	3.41 ± 0.20	2.07 ± 0.13	1.26 ± 0.06	0.96 ± 0.07	0.68 ± 0.02	0.49 ± 0.01	0.41 ± 0.02
17	2015 Feb 08	57061	3.23 ± 0.18	2.02 ± 0.09	1.15 ± 0.06	0.89 ± 0.04	0.80 ± 0.12	0.55 ± 0.05	0.41 ± 0.12

NGC 3227 was monitored from 2012 Nov to 2015 Feb, resulting in three observing periods with data gaps in between (which lasted from 2013 Jun to 2013 Dec, and 2014 May to 2014 Dec). The fluxes of NGC 3227 are listed in Table 5.2. The weather conditions ranged from clear to photometric, and the seeing was $0.9'' - 2.5''$.

Images were reduced with the pipelines described in Sect. 2.3.2. Light-curves were extracted with `GALFIT` only, due to the lack of a sufficient number of stars in the FoV. Since NGC 3227 is a nearby galaxy, PSF-bulge degeneracies are minor. The fit model consisted of the PSF plus a Sersic profile for the bulge. This strategy lead to sufficiently smooth residuals, with statistical errors of the fit being typically 0.01 mag for each component.

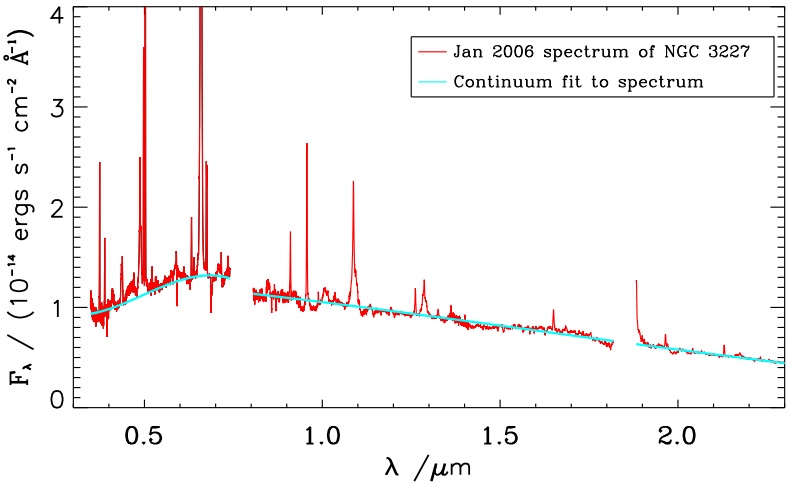

Figure 5.2: *Jan 2006 spectrum of NGC 3227, observed by Landt et al. (2008). This spectrum was corrected for foreground Galactic extinction only. One can see an untypical deviation from the* $F_\lambda \propto \lambda^{-\alpha}$ *power-law describing the AD part of the radiation, apparently caused by massive extinction due to dust present in the host of the AGN.*

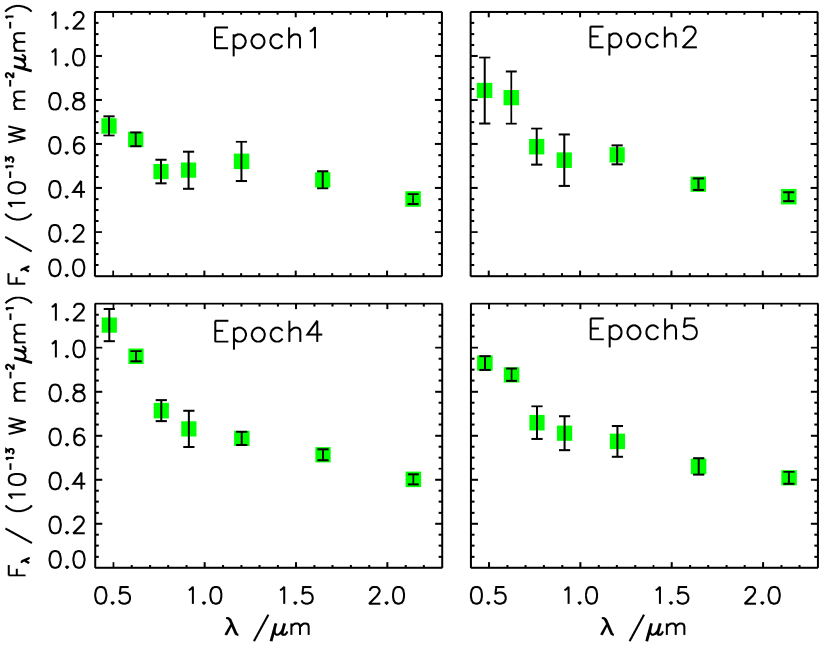

Figure 5.3: *SEDs of NGC 3227, observed with GROND, shown here for epochs 1, 2, 4, and 5 (epoch 3 misses the optical fluxes and is therefore not shown). Fluxes were corrected for foreground Galactic extinction only, and again, an untypical SED shape towards shorter wavelengths, as in Fig. 5.2, can be observed.*

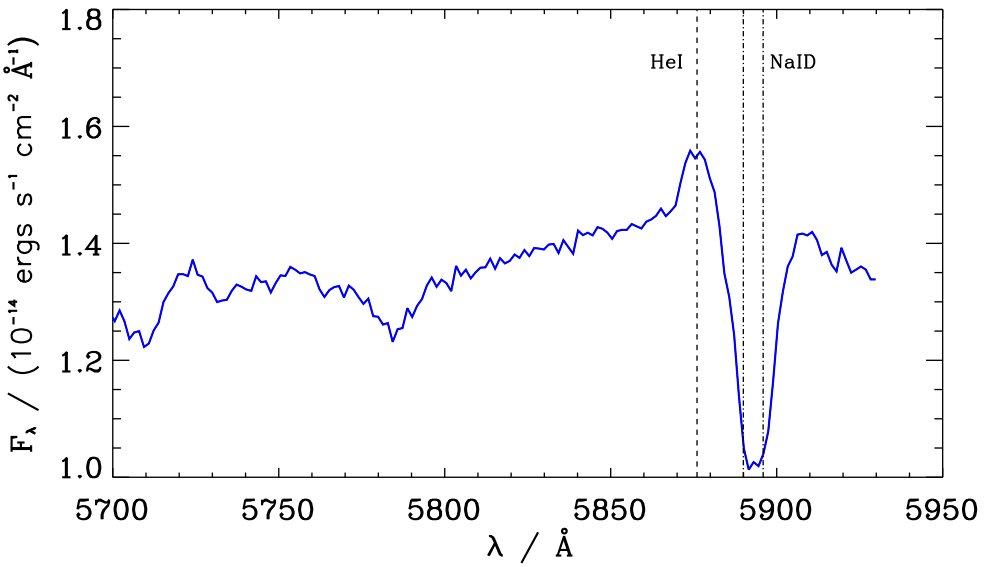

Figure 5.4: *A zoom into the Jan 2006 spectrum of NGC 3227. The two Na ID absorption lines are located at* 5890*Å and* 5896*Å and blend into a single absorption feature. This absorption feature appears very deep relative to the He I feature at* 5876*Å when comparing with the features shown in Fig. 2 of Baron et al. (2016).*

Overall, the SNR of the images was not high enough to include the disk component into the fit, i.e., the disk was mostly lost in the noise. The Sersic half-light radii R_e and Sersic indices n for the different filters and epochs were found to be temporally stable. In a final fit, R_e and n were fixed to their average values determined from the previous fits, i.e. $R_e = 12.0''$ and $n = 2.5$. These parameter values for NGC 3227 are consistent with values found in the literature (Bentz et al., 2009). Absolute flux calibration was performed as described in Sect. 2.3.1, and resulting photometric uncertainties were ≈ 0.05 mag (though up to ≈ 0.1 mag in the K band).

Further, the fluxes were corrected for foreground Galactic extinction, using the Schlafly & Finkbeiner (2011) recalibration of the dust map by Schlegel et al. (1998), as given by NED.

Optical and NIR spectra of NGC 3227 observed (in January 2006) and published by Landt et al. (2008) and Landt et al. (2011) were used to remove emission line contributions from the $g'r'i'z'JHK$ fluxes.

Before, an additional extinction correction had to be made, due to non-negligible extinction in the host galaxy of the AGN. In Fig. 5.2, the Jan 2006 optical and NIR spectra of NGC 3227 are shown. When looking at those spectra, and also at some of the observed GROND SEDs shown Fig. 5.3 (all fluxes corrected merely for Galactic extinction), a devia-

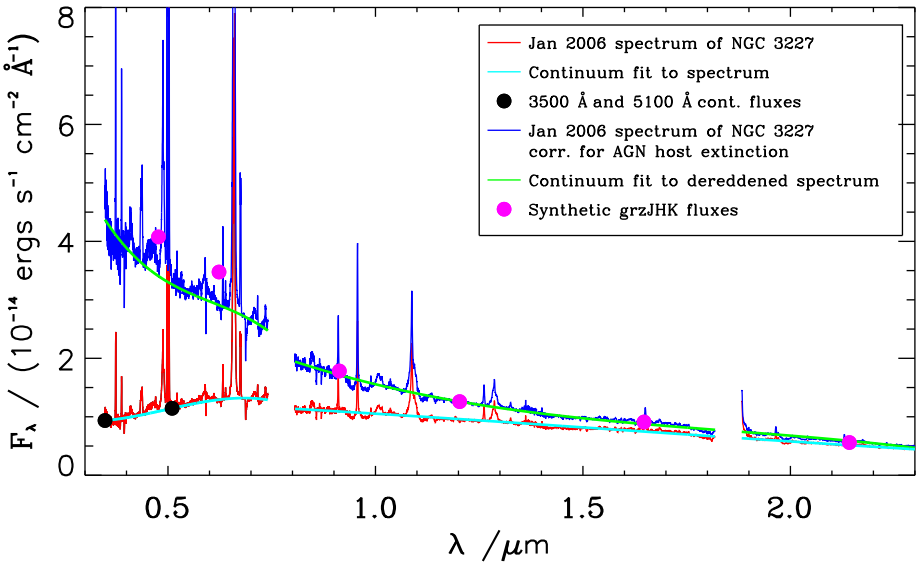

Figure 5.5: *Dereddened Jan 2006 spectrum and synthetic photometry of NGC 3227, together with the original spectrum of Landt et al. (2008). The dereddened spectrum was obtained with procedures described in the text of Sect. 5.3.2.*

tion from the typical $F_\lambda \propto \lambda^{-\alpha}$ ($\alpha > 0$) power-law for short wavelengths is observed. This might indicate that the spectrum is reddened due to extinction by dust present in the AGN host. The methods and relations published in Baron et al. (2016) are used to derive a possible AGN host reddening correction:

Baron et al. (2016) work with a sample of roughly 5000 quasar spectra from the seventh SDSS data release (DR7) and bin the data into 24 two-dimensional bins based on the FWHM of the broad H_β emission line and the index α' (of the $F_\nu \propto \nu^{\alpha'}$ relation). For the resulting stacked spectra, they derive a relation between the reddening of the spectra by dust in the host galaxy and the EW of the Na ID absorption feature (which is attributed to absorption by the host) present in the spectrum. They determine α' according to

$$\alpha' = \log(L_\nu(3000\text{Å})/L_\nu(5100\text{Å}))/\log(5100\text{Å}/3000\text{Å}) - 0.25\ , \tag{5.1}$$

and find a correlation with the equivalent width (EW) of the absorption feature, according to the relation:

$$EW(\text{Na ID}) = a(\alpha' - \alpha'_0) + b\ , \tag{5.2}$$

with a and b determined from their data, where α'_0 corresponds to those spectra where EW (Na ID) goes to zero. Finally, Eq. 5.2 is translated into:

$$E(B-V)_{\text{MW}} = 0.188(\alpha'_0 - \alpha')\ , \tag{5.3}$$

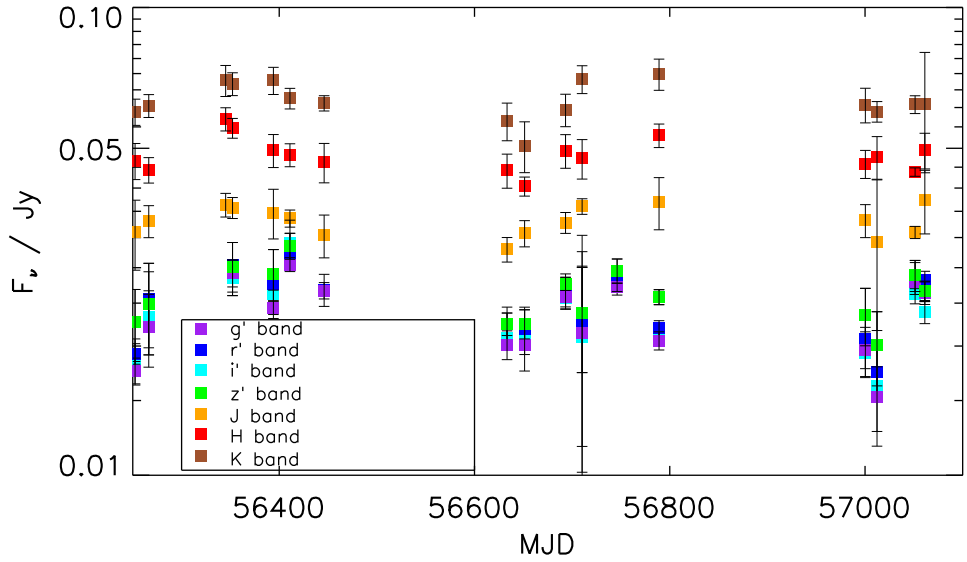

Figure 5.6: *Calibrated $g'r'i'z'JHK$ nuclear fluxes of NGC 3227, from 2012 Nov - 2015 Feb. These fluxes have been derived with* `GALFIT`.

assuming a Milky Way extinction law. This relation is very similar in all other environments, as found by Baron et al. (2016).

A zoom into the Jan 2006 spectrum of NGC 3227 (Fig. 5.4) confirms that indeed, when comparing with Fig. 2 in Baron et al. (2016) (see bottom left panel, FWHM range 4000 - 6000 km s^{-1}), NGC 3227 has a very deep Na ID absorption feature. The optical index α' is derived according to Eq. 5.1. As the spectrum only starts around 3500 Å, a continuum is fit to the spectrum[1] and the continuum fit values at 5100Å and 3500Å are used instead of 5100Å and 3000Å. A value of $\alpha' = -2.2 \pm 0.5$ is obtained. Further, the FWHM of the broad H_β line of 5138 ± 787 km/s resp. 5278 ± 1117 km/s published in Peterson et al. (2004) is used to read off the value of $\alpha'_0 = -0.43$ from Table 1 given in Baron et al. (2016). Following Eq. 5.3, one gets $E(B-V) = 0.34 \pm 0.09$. With the `IRAF` routine deredden from the package onedspec, the dereddened spectrum of NGC 3227, shown in Fig. 5.5, is obtained.

Finally, to remove emission line contributions from the $g'r'i'z'JHK$ fluxes, those contributions are estimated for each passband by applying the GROND filter curves to the spectrum of NGC 3227 obtained in Jan 2006, and comparing the resulting synthetic fluxes to the continuum level at the respective effective wavelength of each passband (see Fig. 5.5). This results in a correction of $g' \approx 17\%$, $r' \approx 25\%$, $z' \approx 8\%$, $J \approx 9\%$, $HK \approx 1\%$. The spec-

[1]The IRAF task continuum from the package onedspec is used to fit the continuum, and both spectra were fit separately (to avoid that possible offsets due to errors in the absolute flux calibration might influence the fit parameters).

trum does not cover the i' band. As there are no prominent emission lines in that passband anyway, no i'-band correction was derived. The computed corrections are very similar to the values derived in the analysis of NGC 4151. Only the J-band correction is significantly lower than in the case of NGC 4151 (with $J \approx 15\%$).

5.3.3 Methods

The two alternative reverberation models described by Eq. 2.3 and Eq. 2.6 are fit to the NGC 3227 data set. Prior to the fit, the g'-band lightcurve needs to be interpolated to get a smooth input signal for the fit.

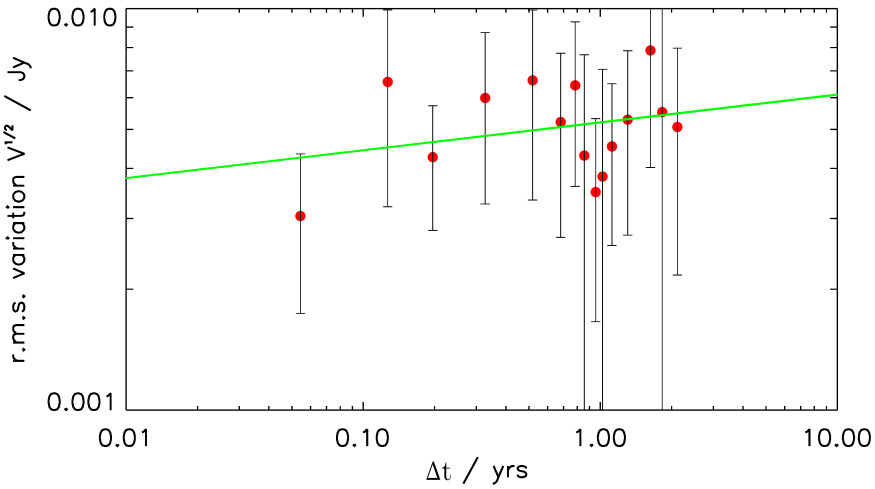

Figure 5.7: *The estimated* $(v_{ij})^{1/2}$ *(red dots) from the* g'*-band data versus* Δt_{ij}*, shown in logarithmic scale.*

This is done with the methods described in Sect. 2.4. Having confirmed that the results of the reverberation analysis is insensitive to the particular choice of the structure function model (see Sect. 4.4.2), the model has been restricted to the power-law case in this analysis. From the data, best-fit values of $A = 0.0062 \pm 0.0004$ Jy (resp. $A = 0.77 \pm 0.06 \cdot 10^{-13}$W m$^{-2}\mu$m^{-1}) and $\gamma = 0.14 \pm 0.13$ (see Fig. 5.7) are obtained for the average flux variability A on a one-year timescale, and the gradient of this variability γ. Using these parameter values, the g'-band light-curve is interpolated. The result is shown in Fig. 5.8.

As for the analysis of NGC 4151, the best model parameters are inferred using the DE-MC algorithm described in Sect. 2.5. The number of data points is $N = 110$ (NIR plus optical). Uniform priors within the limits $x_{\rm min}, x_{\rm max}$ as given in Table 5.3 are used in order to exclude

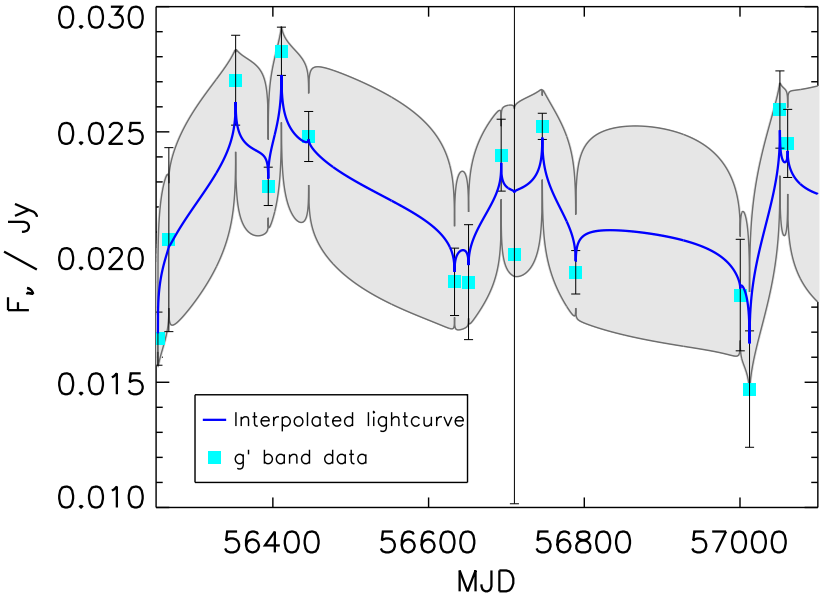

Figure 5.8: *The interpolated g'-band light-curve, obtained with the method of Rybicki & Press (1992).*

unphysical parameter ranges. Further, $p(T_{\rm sub}) = 0$ for $T_{\rm sub} < T_0$ was used. For the sublimation model, the parameter ν was fixed as it showed high degeneracies with the parameter β. A consistent value of $\nu \approx 1$ was found in the sub-sample analysis presented in Chapter 5.5, so $\nu = 1$ seems a reasonable assumption.

5.3.4 Results

The temporal evolution of the photometry of the nucleus of NGC 3227 is shown in Fig. 5.6. One can divide the data set into three periods of observations, with substantial time gaps in between. When looking at the NIR versus optical fluxes of the first period, one can immediately see a qualitative difference to the second and third period: in the later periods, the flux variations in the NIR bands clearly show a time lag behind those of the AD-dominated g' band, and this lag increases with wavelength. This band-dependent behavior is caused by the reverberation of the AD signal by the hot dust, as well as the increasing dust contribution and decreasing AD contribution for longer wavelengths.

In the first period, however, the expected behavior – i.e., the dust signal being a delayed and smoothed-out version of the AD signal – is not observed. The NIR fluxes do not follow the AD signal up to its maximum value, but decrease earlier than the AD signal (which might give the impression that the NIR data even precede the optical data). Moreover, the

Table 5.3: *Upper and lower limits $x_{\min}, x_{\max}$ for uniform prior pdfs of the model parameters, for the standard model and the sublimation model. In addition to these limits, $p(T_{\rm sub}) = 0$ for $T_{\rm sub} < T_0$ was used. In Col. (1), the notation τ_0 refers both to the initial reverberation delay τ_0 in the sublimation model, but also to the constant delay τ (denoted as τ_1 in Sect. 2.2.1) in the standard model. Similarly, the notation $C_{2,0}$ here refers to the initial value of the blackbody constant in the sublimation model, but also to the constant value of C_2 in the standard model. The variability factor was fixed to $\nu = 1$ in the sublimation model.*

Parameter	Unit	Standard model		Sublimation model	
		$x_{\min}$	$x_{\max}$	$x_{\min}$	$x_{\max}$
C_1	–	0.05	0.45	0.05	0.45
$C_{2,0}$	10^{-18}ster	0.01	10.0	0.01	10.0
T_0	1000K	1.0	2.0	1.0	2.0
τ_0	days	0.0	100.0	0.0	100.0
α	–	1.5	2.5	1.5	2.5
ν	–	0.5	3.0	–	–
C_3	10^{-3}K^{-4}	–	–	0.0	1.0
$T_{\rm sub}$	1000K	–	–	1.4	2.2
$\mathscr{T}_{\rm ref}$	days	–	–	0.0	500.0
β	–	–	–	-3.0	0.0

overall rise is not as steep as the AD curve.

It has been checked and excluded that the observed early NIR flux decrease is merely caused by calibration errors and/or a wrong decomposition in GALFIT[2]. This observed obvious lack of flux in the NIR bands in the first period of the data set might indicate a loss of flux due to dust destruction via sublimation.

Standard model without dust sublimation

The results of the standard model fit without dust sublimation are shown in Fig. 5.9. The first six panels show the temporal evolution of the fluxes for the bands $g'r'z'JHK$ (the i' band is omitted, since it is qualitatively equal to the r' band), while the bottom three panels display the SED for three selected epochs. The best-fit lag is $\tau = 40.2 \pm 2.2$ days, and the best-fit value for the power-law slope is $\alpha = 1.97 \pm 0.04$. The initial blackbody temperature has a best-fit value of $T_0 = 1599 \pm 49$ K, and then evolves (by construction) as in Eq. 2.4. It is apparent from Fig. 5.9 that the standard model fits the NIR data only poorly in the first period of the observations. To not make the deviations between model and NIR data in that first period too high, the algorithm fits a rather flat curve to the data. Consequently, the

[2]To exclude calibration errors due to flux deviations of single calibration stars in any epoch, the calibration was additionally performed with each of the calibration stars alone. To exclude a wrong flux attribution between the different components in GALFIT, all images were additionally fit using only a PSF model for the AGN. The light-curves obtained using any of these methods look qualitatively equal (after accounting for the different absolute flux level in the PSF-only fit) to the ones presented in Fig. 5.6.

Table 5.4: *Global mean and errors for the parameters of the two models. The errors are given by* $\Delta x = \sqrt{\hat{V}}$ *of the Gelman convergence diagnostics (Gelman & Rubin, 1992; Brooks & Gelman, 1998) for each parameter (see Sect. 2.5.2). In Col. (1), the notation* τ_0 *refers both to the initial reverberation delay* τ_0 *in the sublimation model, but also to the constant delay* τ *(denoted as* τ_1 *in Sect. 2.2.1) in the standard model. Similarly, the notation* $C_{2,0}$ *here refers to the initial value of the blackbody constant in the sublimation model, but also to the constant value of* C_2 *in the standard model. The variability factor was fixed to* $\nu = 1$ *in the sublimation model. For the sublimation model, the reverberation delay at sublimation end,* $\tau_{\rm max}$*, is listed as well (even though this value is not a fit parameter).*

Parameter	Unit	Standard model	Sublimation model
C_1	–	0.24 ± 0.01	0.24 ± 0.01
$C_{2,0}$	10^{-18}ster	0.52 ± 0.06	0.59 ± 0.10
T_0	1000K	1.599 ± 0.049	1.626 ± 0.060
τ_0	days	40.2 ± 2.2	34.1 ± 1.6
α	–	1.97 ± 0.04	1.95 ± 0.04
ν	–	0.68 ± 0.12	1.00 (fixed)
C_3	10^{-3}K^{-4}	–	0.34 ± 0.24
$T_{\rm sub}$	1000K	–	1.697 ± 0.057
$\mathcal{T}_{\rm ref}$	days	–	139.9 ± 76.3
β	–	–	-1.15 ± 0.70
$\tau_{\rm max}$	days	–	39.5

variability factor is only $\nu = 0.68 \pm 0.12$. The reduced χ^2 of this fit is shown for each band in Fig. 5.9.

Clearly, the derived reverberation delay in this standard model fit is determined by the data of period 2 and 3, since no delay $\tau > 0$ can suitably describe the data in period 1 (as the NIR signal does not seem to be a delayed version of the AD signal here).

Sublimation model

The results of the sublimation model fit are shown in Fig. 5.10. As for the standard model, the first six panels show the temporal evolution of the fluxes for the bands $g'r'z'JHK$, while the bottom three panels display the SED for the same three epochs as in Fig. 5.9. The best-fit initial lag before sublimation start is $\tau_0 = 34.1 \pm 1.6$ days, and the best-fit value for the power-law slope is $\alpha = 1.95 \pm 0.04$. The initial blackbody temperature has a best-fit value of $T_0 = 1626 \pm 60$ K. The best-fit sublimation temperature is 1697 ± 57 K. Sublimation starts at $t_{\rm start} = t_0 + \tau_0 + 18$ days in this model, and the reverberation delay is increased to $\tau_{\rm end} = 39.5$ days at sublimation end. The reduced χ^2 of this fit is shown for each band in Fig. 5.10.

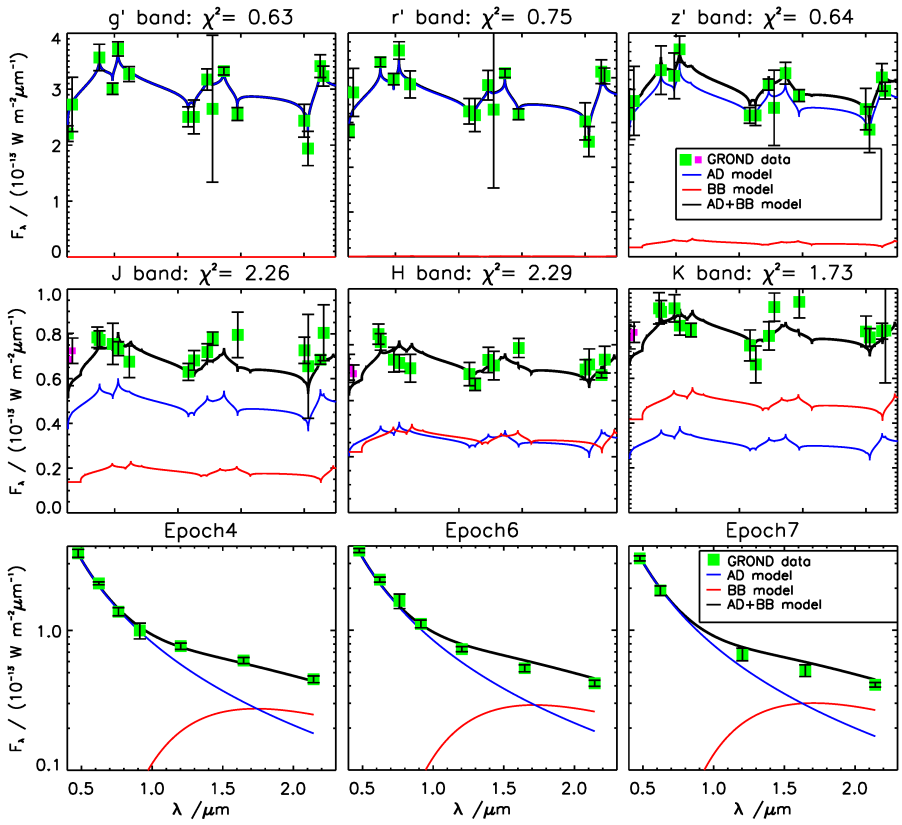

Figure 5.9: *Results of the standard model fit plotted over time (g', r', z', J, H, K bands, panels 1-6) and over wavelength (for epochs 4, 6, and 7 in panels 7-9). Green and magenta squares represent the data, where magenta marks those data points that were excluded from the fit (epochs 1 and 2 in the NIR data, as $t < \tau_0$). The red line represents the blackbody contribution for each band, blue the AD contribution, and the black line is the sum of both. From the reduced χ^2 values given for each band, it can be seen that the standard model fits the optical data well, but fails to reproduce the NIR fluxes, especially in period 1.*

The temporal evolution of some of the quantities of the sublimation model, namely the AD g'-band flux F_g, the hot dust temperature T, the blackbody constant C_2, and the hot dust flux $F_{\rm BB}$ in the K band are plotted in Fig. 5.11. The marginalized posterior probability distributions for the parameters $C_{2,0}$, T_0, τ_0, C_3, $T_{\rm sub}$, and $-\beta$ are shown in Fig. 5.12. As can be seen, $C_{2,0}$ and T_0 are strongly anti-correlated, and so are $C_{2,0}$ and $T_{\rm sub}$. However, any increase or decrease in $C_{2,0}$, and hence decrease or increase in T_0, will only shift the resulting temperature curve in vertical direction. Furthermore, as can be expected, T_0 and $T_{\rm sub}$ are strongly correlated. The parameter $\mathcal{T}_{\rm ref}$ (not shown in Fig. 5.12) cannot be constrained by the data. It is roughly equally distributed between 0 and 200 days, i.e. no specific re-illumination timescale is preferred as long as the re-illumination falls into the data gap between the first and second period of the data.

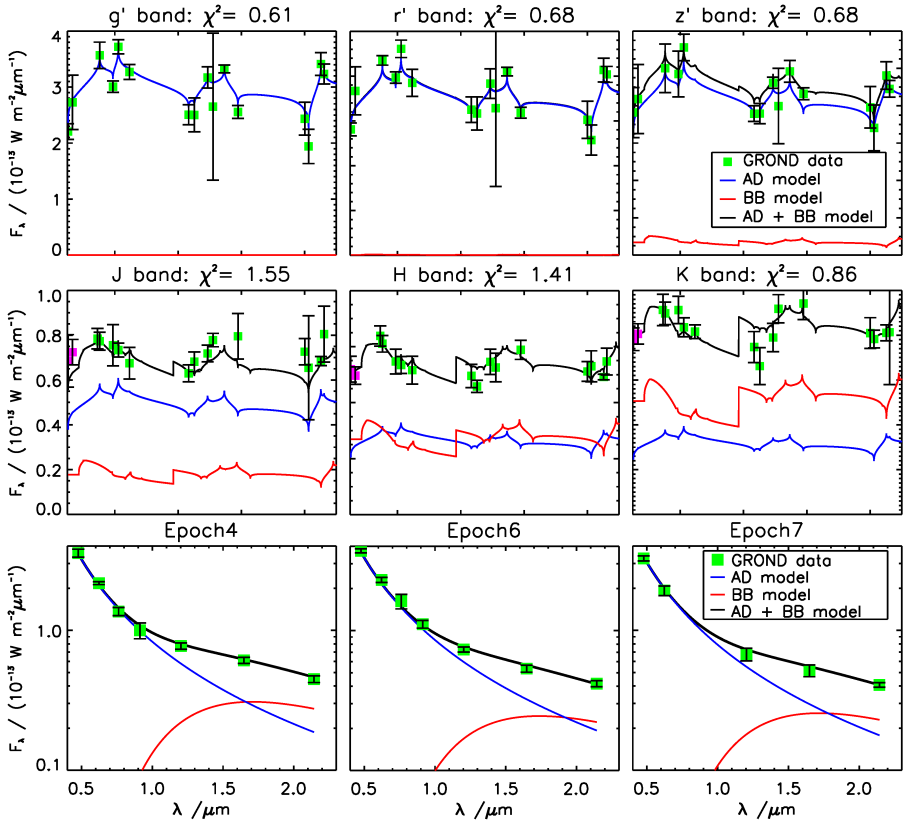

Figure 5.10: *Results of the sublimation model fit, plotted over time (g', r', z', J, H, K bands, panels 1-6) and over wavelength (for epochs 4,6,and 7 in panels 7-9). Green and magenta squares represent the data, where magenta squares mark those data points that were omitted in the fit (epochs 1 and 2 of the NIR data, as $t < \tau_0$). The red line represents the blackbody contribution for each band, blue the AD contribution, and the black line is the sum of both. From the reduced χ^2 values (and visually from period 1) for each band, it can be seen that the sublimation model is able to reproduce the NIR data much better than the standard model. The optical data are fit equally well by both models.*

5.3.5 Discussion

As can be seen from Fig. 5.9 and Fig. 5.10 and the reduced χ^2 given there for each band, the sublimation model fits the NGC 3227 data significantly better than the standard model without dust sublimation. Regarding the fact that historically, the absolute AD luminosity has increased by a factor of 3-4 compared to observations in 2001-2007 (showing a reverberation delay $\tau \approx 15$ days as found by Suganuma et al. (2006) and Koshida et al. (2014)), sublimation of dust and an increased reverberation delay in 2012 - 2014 seem a plausible possibility for this target.

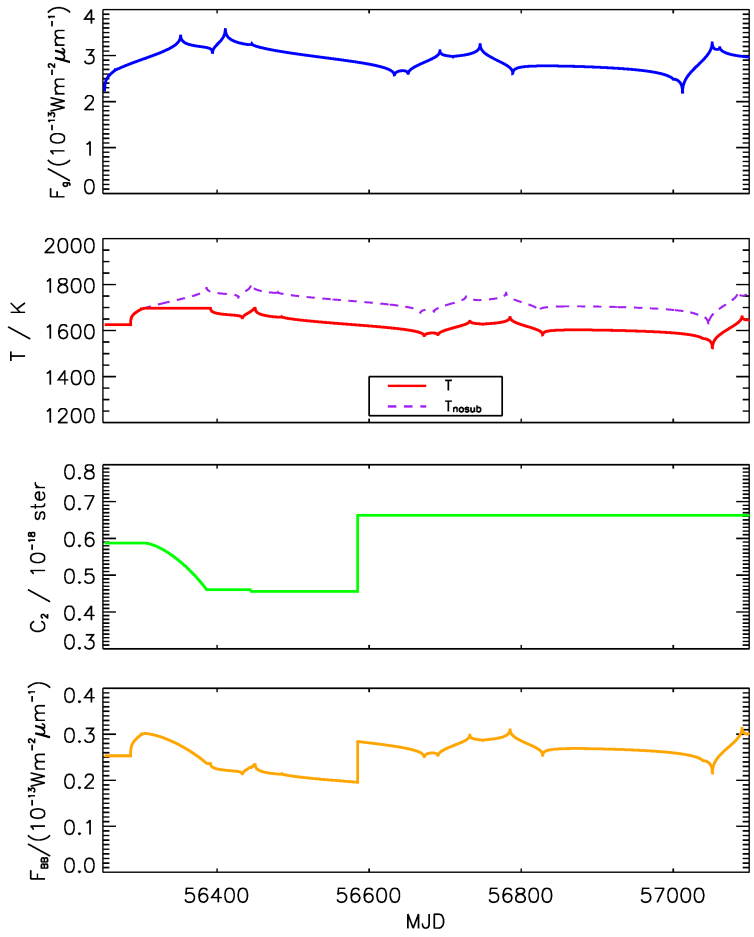

Figure 5.11: *Evolution of the AD g'-band flux F_g, the hot dust temperature T with and without the assumption of sublimation, i.e., T and $T_{\rm nosub}$ (as defined in Eq. 2.11), the blackbody constant C_2, and the K-band hot dust flux $F_{\rm BB}$ for the best fit of the sublimation model.*

Sublimation fluxes

In the sublimation model, the instantaneous flux is used as the driving signal for the sublimation. Kishimoto et al. (2013) have claimed that any changes in the dust reverberation radius only follow changes in the incident flux averaged over a long retro timescale, using their Spearman rank correlation analysis of a compilation of historic AD lightcurves and K-band dust radii (observed with interferometry and dust reverberation). They found $\mathcal{T}_{\rm retro} > 6$ years for the observed reverberation measurements.
However, they also point out that their derived timescale $\mathcal{T}_{\rm retro}$ might actually be an average of the two distinct timescales for sublimation and reformation, with the former likely being shorter than the latter. Indeed, looking at their data (Fig. 1.9) suggests that the derived $\mathcal{T}_{\rm retro}$ for the reverberation measurements is completely governed by those data points measuring a delayed decline of the dust radius following a period of high AD luminosity roughly

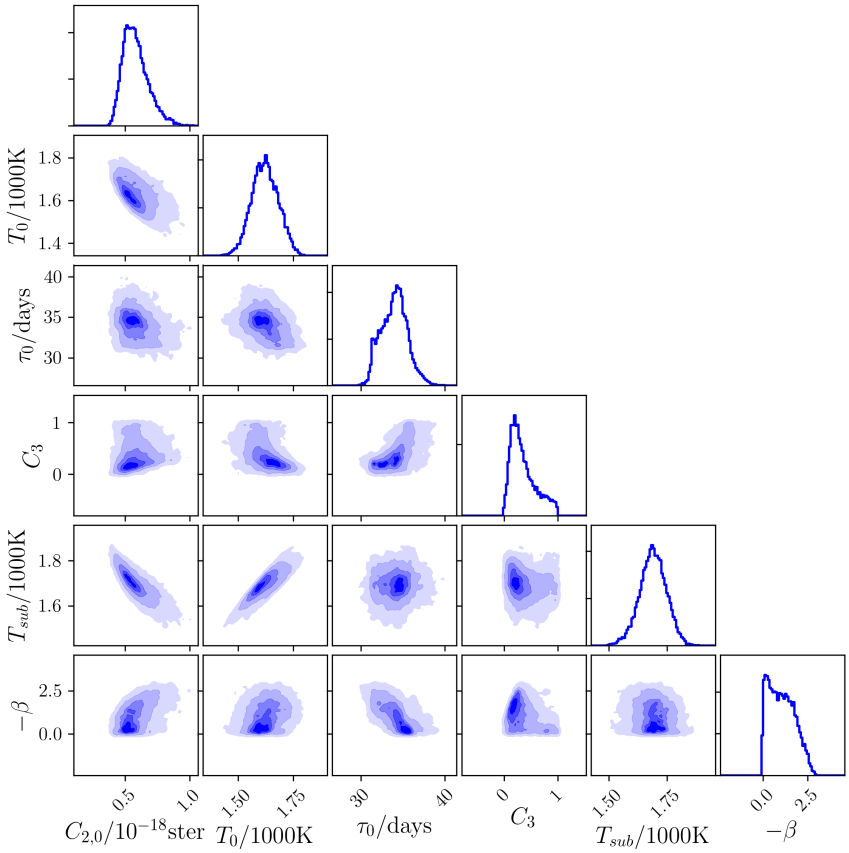

Figure 5.12: *Marginalized posterior probability distributions for the parameters $C_{2,0}$, T_0, τ_0, C_3, $T_{\rm sub}$, and $-\beta$ of the sublimation model fit. Contours mark the 10%, 25%, 50%, 85% and 99% confidence intervals.*

7-8 years before. These data points presumably mark a period of dust surface reformation, following substantial dust sublimation 7-8 years before. This observed radius decline contributes 12 out of 14 data points, so the derived $\mathcal{T}_{\rm retro}$ for the reverberation radii is very likely to represent the reformation timescale alone.

When performing the analysis without the radius reformation measurements (Fig. 5.13)[3], but also including the inferred NIR reverberation radii from Sect. 4.4, a high Spearman rank correlation coefficient of the dust radii with the instantaneous AD signal ($\rho = 1.0$) is found, and the correlation decreases rapidly with increasing the averaging time $\mathcal{T}_{\rm retro}$, as is already suggested by pure visual inspection of the data (Fig. 1.9). Due to the now substan-

[3]For the re-calculated correlation coefficients of the reverberation data, minor deviations from the corresponding curve in Kishimoto et al. (2013) are presumably caused by slight differences in the used V-band light-curve, since not all of the data used by Kishimoto et al. (2013) were publicly available. Further, the z-band fluxes from Sect. 4.2 were included and converted to V-band fluxes using the derived α for NGC 4151.

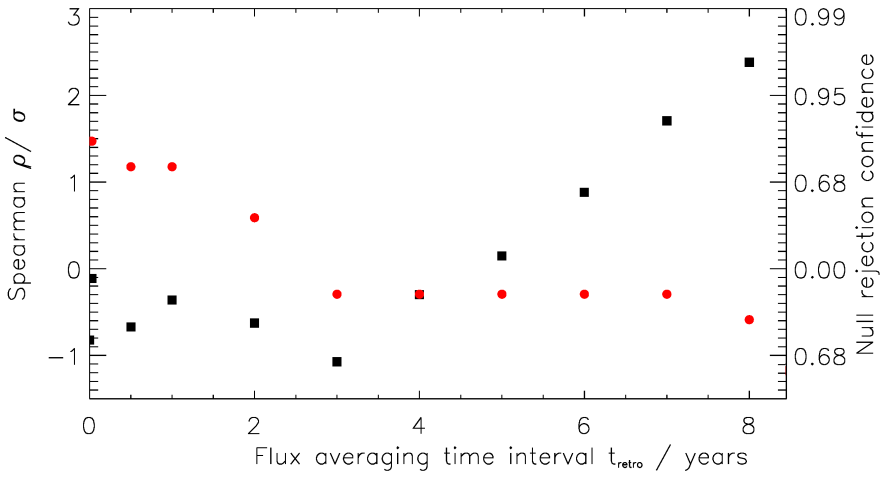

Figure 5.13: *Spearman rank correlation coefficient, in units of the standard deviation expected in the null hypothesis (following the representation of Kishimoto et al. (2013), for consistency). Black squares show the correlation for all reverberation measurements used by Kishimoto et al. (2013), including the 12 out of 14 data points tracing dust reformation. Red circles mark the correlation for the radii tracing dust sublimation, including also the data points from the analysis presented in Chapter 4. The maximum value of ρ/σ is lower for the sublimation-only data points, but ρ is absolutely higher ($\rho = 1.0$). The correlation of the sublimation-only reverberation radii with the AD signal is highest for $\mathcal{T}_{\rm retro} = 0$ days and $\mathcal{T}_{\rm retro} = 10$ days ($\approx$ instantaneous flux), and decreases rapidly for $\mathcal{T}_{\rm retro} > 1$ year.*

tially decreased number of data points ($n = 4$), any found correlation cannot be statistically significant (as reflected by the high p-value 0.2).
More radius measurements are indispensable to resolve this issue. When taking the inferred K-band-only delays derived in Sect. 4.4 instead of the delay inferred from the multi-band analysis, the results found here remain qualitatively unaltered.[4]

Sublimation timescales

From Fig. 5.11, it can be seen that the destruction of innermost dust clouds (or substantial parts of these) happens in roughly 150 days, as inferred from the best fit.
Following derivations by Guhathakurta & Draine (1989), Kimura et al. (2002), and Kobayashi

[4]It should be emphasized that even if $\mathcal{T}_{\rm retro} > 6$ years also for sublimation, this does not contradict the potential dust sublimation observed in the data. A strong increase in the averaged AD flux prior to the observations carried out in this work is likely, as the absolute AD luminosity has significantly increased compared to observations 5 years before (Suganuma et al., 2006).

et al. (2011), the timescale for sublimation of a region with optical depth unity is given in Kishimoto et al. (2013) as:

$$\mathscr{T}_{\rm dest} = \frac{m}{|{\rm d}m/{\rm d}t|} \tag{5.4}$$

$$= \frac{4}{3}\pi a^3 \rho \left(4\pi a^2 \sqrt{\frac{M_r u}{2\pi k_{\rm B} T}} P_{\rm vap}\right)^{-1} . \tag{5.5}$$

Here, ρ is the bulk density of a dust particle assumed to be spherical, a is its radius, M_r is the molecular mass of gas released from dust due to sublimation, and u is the atomic mass unit. The vapor pressure $P_{\rm vap}$ entering Eq. 5.5 depends on the assumed dust temperature during sublimation as $P_{\rm vap} \propto \exp(-A/T)$, with $A = -81,200$K for graphite dust. The resulting sublimation timescale is thus highly dependent on T.
An optical depth of the innermost dust clouds of ≈20 suggests $\mathscr{T}_{\rm dest} \approx 7$ days. Assuming graphite dust particles with a grain size of $a = 0.05\mu$m, Eq. 5.5 then implies a sublimation temperature of $T_{\rm sub} \approx 1850$ K. This value seems to contradict the inferred best-fit sublimation temperature $T_{\rm sub} \approx 1700$ K, at first glance.

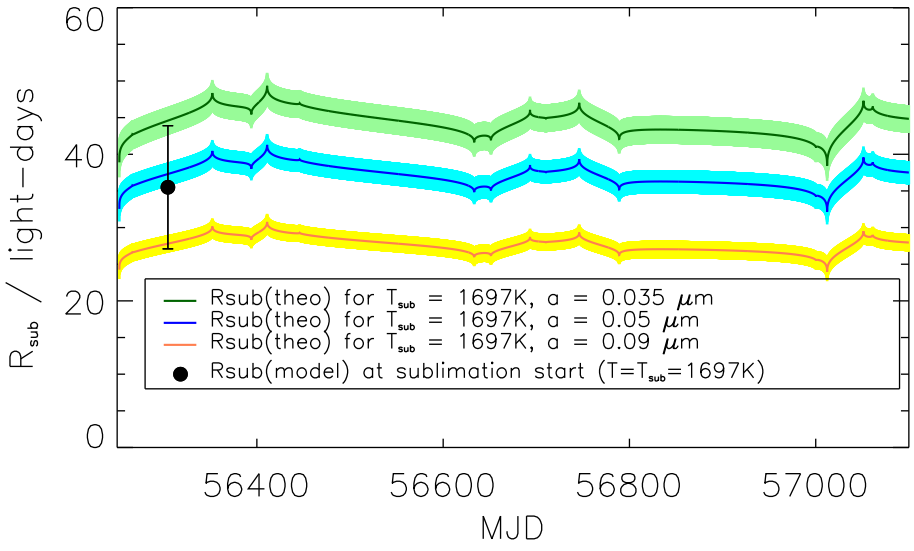

Figure 5.14: *Estimated hot dust sublimation radius for NGC 3227 (using Eq. 1 in Kishimoto et al. (2007)), for the best-fit sublimation temperature* $T_{\rm sub} = 1697$ *and different grain sizes a. Overplotted is the best-fit sublimation radius obtained from the sublimation model (as given by the best-fit reverberation delay* $\tau_0 = 34.1 \pm 1.6$ *days at sublimation start* $t_{\rm start} = t_0 + \tau_0 + 18$ *days).*

However, it has to be pointed out that the inferred sublimation temperature is likely to not adequately represent the real, physical sublimation temperature of the innermost, hottest dust. To be precise, the hot dust blackbody temperature measured with the pre-

sented method always represents an average temperature of the inner radial dust distribution, i.e., of those clouds that contribute significantly to the NIR fluxes. From the analysis of NGC 4151 in Chapter 4, it has been found that the temperatures of the innermost (J-band) and outermost (K-band) clouds contributing to our NIR fluxes span a range of roughly 300 K. Similarly, the inferred sublimation temperature $T_{\rm sub}$, and all other parameters related to the hot dust, represent an average over the inner radial dust distribution rather than the precise value of the innermost, hottest dust[5].

Furthermore, it must be emphasized that the temperatures inferred with the presented model show strong degeneracies with the parameter $C_{2,}$, and should therefore not be taken as precise absolute temperature values, as already pointed out in Sect. 5.3.4. However, any increase or decrease in $C_{2,0}$, and hence decrease or increase in T_0 and $T_{\rm sub}$, will only shift the resulting temperature curve in vertical direction. The qualitative finding whether or not the hot dust is found at or below sublimation, remains unaltered. An uncertainty in this context is the absolute flux level inferred for each band, especially for the NIR bands. It has been checked and confirmed that changing the absolute level of one NIR band by 5-10% results in a 100 K higher or lower best-fit value for T_0 as well as for $T_{\rm sub}$, while all other parameters (except for $C_{2,0}$) stay practically unaltered.

Further, the theoretically expected sublimation radius is calculated according to Eq. 1.14, using the best-fit sublimation temperature derived in the sublimation model fit. $L_{\rm UV}$ in Eq. 1.14 is estimated using $L_{g'}$ and the best-fit value of α. Then $R_{\rm sub,theo}$ is compared to the sublimation radius directly obtained from the sublimation model. The derived theoretical sublimation radius is shown in Fig. 5.14 using $T_{\rm sub} = 1697$ K and different grain sizes a. Overplotted is the best-fit sublimation radius (as calculated from the best-fit reverberation delay $\tau_0 = 34.1 \pm 1.6$ days at sublimation start $t_{\rm start} = t_0 + \tau_0 + 18$ days). Within the errors, grain sizes $0.03\mu{\rm m} < a < 0.09\mu{\rm m}$ are consistent with the fit results. However, as already pointed out, this estimate is influenced by uncertainties regarding the absolute value of our inferred best-fit sublimation temperature, i.e., a possibly different value of the real, physical sublimation temperature.

Radial dust distribution

From Fig. 5.12, one can see that the parameter $-\beta$ has highest probabilities for $-\beta \lesssim 0.5$, which is consistent with values for NGC 3227 as given in the literature (Ramos Almeida et al. (2009), Hönig et al. (2010), and Alonso-Herrero et al. (2011) found $-0.5 < \beta < 0$). However, values up to $-\beta = 2$ seem almost as likely, so this parameter cannot be further

[5] An additional explanation for the discrepancy between the theoretically estimated and the measured $T_{\rm sub}$ might be that one actually sees a mixture of graphite and silicate dust. For silicate dust, $T_{\rm sub} = 1440$K would lead to the value of $\mathcal{T}_{\rm dest} \approx 7$days implied by the data, so observing a mixture of both dust species in the data could perfectly reconcile measured and theoretical sublimation temperature. However, considering the absence of a strong or even moderate silicate emission feature in NGC 3227 (Hönig et al., 2010), this interpretation seems unlikely.

constrained from the data.

An upper limit for the mean inter-cloud delay can be estimated by $\tau_{\rm cl} < Y/N_0 \cdot \tau_{\rm sub}$. Here Y is the outer torus radius in units of $c \cdot \tau_{\rm sub}$, and N_0 the number of clouds along an equatorial line of sight. Further, the radius of a single cloud is assumed to be small compared to the radial torus extent (Hönig & Kishimoto, 2010), i.e., $R_{\rm cl} << Y$. Due to the radial dust distribution $\eta_r \propto r^{\beta}$ (Eq. 1.3), $\tau_{\rm cl}$ can be significantly shorter than $Y/N_0 \cdot \tau_{\rm sub}$ at the inner torus edge in some objects, but for NGC 3227, the radial dust distribution is very flat. For NGC 3227, Alonso-Herrero et al. (2011) have found $Y \approx 17$, and $N_0 \approx 14$. Assuming a slight density increase towards the inner edge due to $-0.5 < \beta < 0$, it is reasonable to assume $\tau_{\rm cl} \lesssim 1 \cdot \tau_{\rm sub}$. Such an estimate of $\tau_{\rm cl}$ is consistent with the results for $\mathcal{T}_{\rm ref}$ of the sublimation model, but cannot be further constrained. The parameter $\mathcal{T}_{\rm ref}$ is roughly equally distributed between 0 and 200 days, so no specific re-illumination timescale is preferred by the fit, and formally even a timescale as short as < 1 day is as likely as higher values. The reason for this is the large data gap between MJD 56446 and MJD 56633 (when the object was not observable from La Silla).

It must be emphasized that the inference and discussions of this analysis are based on a limited number of data points. Limitations of the method are clearly given here by the temporal sampling. To improve the reliability in similar future analyses, a better temporal sampling, specifically avoiding large data gaps, would certainly be desirable.

5.4 The targets Ark 120 and NGC 5548

Ark 120 was observed in 28 epochs from 2012 Oct - 2015 Nov . The monitoring of NGC 5548 only covered six epochs in the range 2014 Feb - 2014 Jul. Due to its declination of $\delta = +25°$ $08' 13''$, this object is observable from La Silla for only 6 months, and was mainly monitored as a part of the AGN Space Telescope and Optical Reverberation Mapping Project and (AGN STORM, see e.g. Peterson & Agn Storm Team (2015)) reverberation collaboration.

Depending on object and band, either `GALFIT` or `ISIS` or both methods, were used to extract the nuclear fluxes. The first three analyzed GROND objects are all nearby galaxies, so the use of `ISIS` was not mandatory. Whenever possible, both methods were used for comparison.

For Ark 120, photometry was performed using both methods in the optical, and the resulting fluxes were found to agree well within the errors. In the NIR, only `GALFIT` was used, since the number of stars was not sufficient for `ISIS`[6]. The `GALFIT` model here consisted of

[6]Unfortunately, two of the high SNR stars that were gained with the larger NIR FoV, were variable stars. A further variable star was located in the common optical/NIR field of view, another star was too bright and thus saturated. Masking the unsuitable stars lead to satisfying results in the optical (and good agreement with `GALFIT` light-curves), but poor results and high errors in the NIR, where the pixel scale is four times larger and the SNR is worse, and the PSF is found to vary substantially across the FoV.

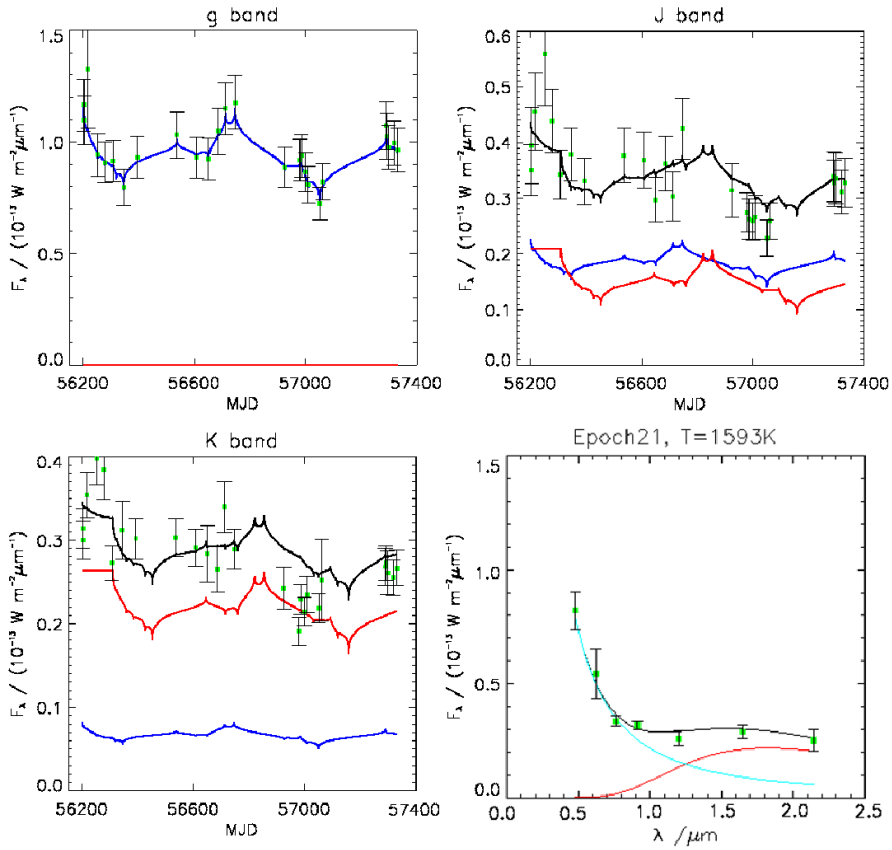

Figure 5.15: *Results of the standard model fit for Ark 120, plotted over time (g',J,K bands, panels 1-3) and over wavelength (for the exemplary epoch 21). Green squares show the GROND data. The red line represents the blackbody contribution for each band, blue the AD contribution, and the black line is the sum of both.*

the PSF plus an exponential disk profile for the disk. In the literature (Bentz et al., 2009), Ark 120 is characterized as an irregular galaxy with a very small bulge. In the GROND detector, the size of this bulge is << 1 pixel, causing degeneracies with the PSF. Therefore, the fit was restricted to a PSF plus disk model for this galaxy. The derived mean disk scale length is $R_s = 3.0''$, in good agreement with Bentz et al. (2009). To correct for a possibly non-negligible flux offset when omitting the bulge, a further fit is performed: a PSF-bulge-disk decomposition with $R_s = 2.9''$, $n = 3.62$ (taken from Bentz et al. (2009)) and $R_e = 0.6'' = 1$ NIR pixel, with fixed position angles and axis ratios of the bulge and disk component. For most of the epochs, the shape of the resulting nuclear light-curve looks like in the previous fit, indicating reasonable fit results. Only for a few epochs, PSF-bulge degeneracies (and possibly PSF mismatches) result in a far too low flux (almost zero) of the PSF component compared to the PSF-disk lightcurve. As final input to the reverberation model fit, the nuclear fluxes derived from the PSF-disk model fit were used, corrected for the mean offset between the PSF-disk fit and the PSF-bulge-disk fit (depending on the passband, roughly

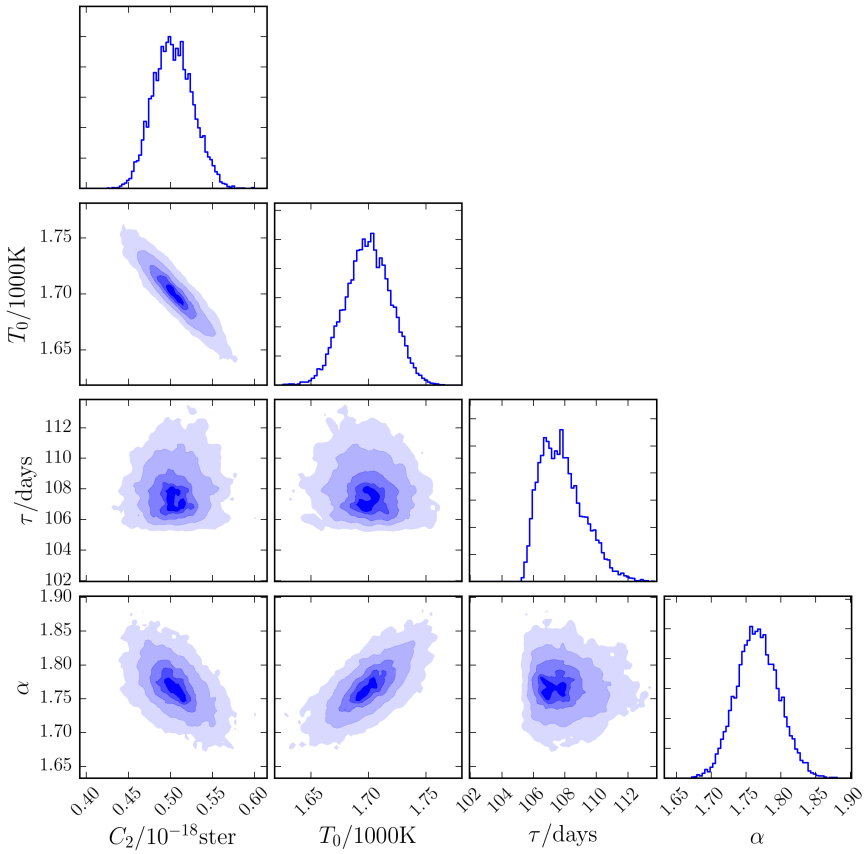

Figure 5.16: *Marginalized posterior probability distributions for the four parameters C_2, T_0, τ, and α of the standard model fit for Ark 120.*

15-25% of the flux level of the PSF-disk fit), calculated from those epochs with reasonable fit results.

For NGC 5548, optical lightcurves were extracted using `GALFIT` only, since the optical FoV does not contain enough high SNR stars. In the NIR, due to further suitable stars in the larger FoV, both methods could be used, and very good agreement is found between the derived fluxes. As in the case of NGC 3227, the SNR was generally not high enough to include the disk into the fit model. A PSF-bulge decomposition was performed, with resulting mean fit parameters $R_e = 12.6''$ and $n = 3.0$.

As described in Sect. 5.3.2, fluxes were corrected for foreground Galactic extinction (Schlafly & Finkbeiner, 2011; Schlegel et al., 1998), and a correction for emission line contamination in the derived nuclear fluxes was performed in analogy to NGC 4151 and NGC 3227. For most of the GROND targets of this program, as in the case of Ark 120

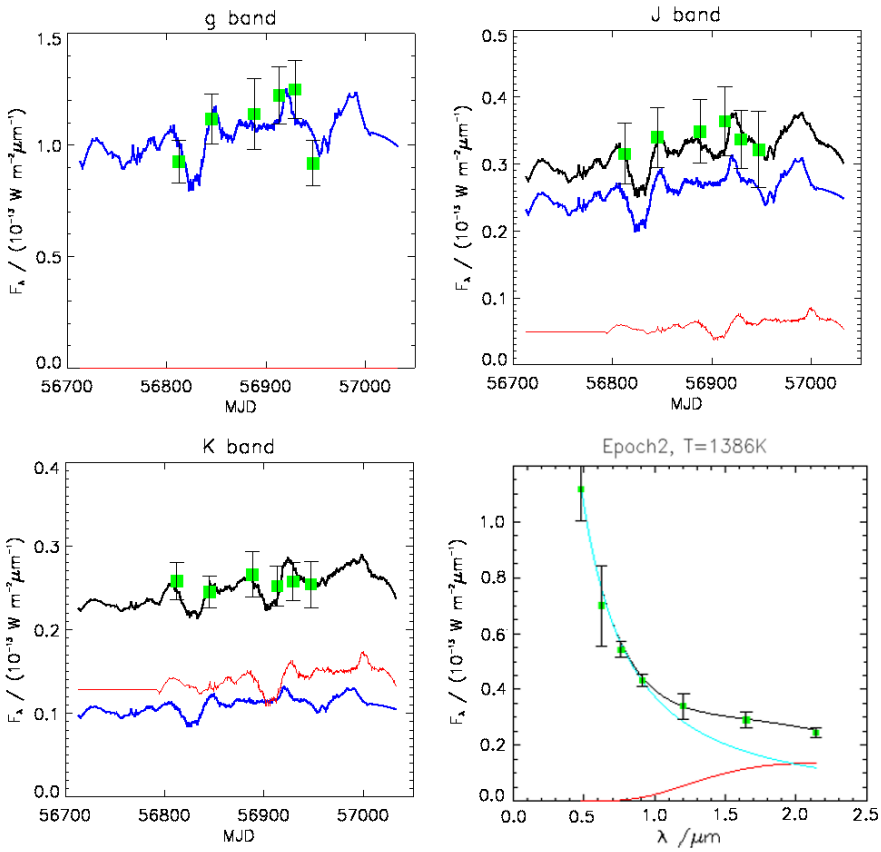

Figure 5.17: *Results of the standard model fit for NGC 5548, plotted over time (g', J, K bands, panels 1-3) and over wavelength (for the exemplary epoch 2). Green squares show the GROND data. The red line represents the blackbody contribution for each band, blue the AD contribution, and the black line is the sum of both.*

and NGC 5548, no individual spectra were observed or available. For those objects, in the optical, the equivalent widths of typical AGN emission lines are used, as derived from a composite spectrum of a large number of AGNs as given by Blandford et al. (1990), resulting in $g' \approx 20\%$, $r' \approx 25\%$, $i' \approx 0\%$, $z' \approx 3\%$. In the g' and r' bands, due to uncertainties in some of the cited EWs of up to 50%, the errors of this estimate are high. However, they seem to agree fairly well with the values derived for NGC 3227 (see Sect. 5.3.2). In the NIR passbands, the values derived for NGC 4151 were adopted ($J \approx 15\%$, $HK \approx 2\%$).

For the driving AD signal of NGC 5548, the V-band light curve from the AGN STORM project, taking place concurrently with the GROND observations (Edelson et al., 2015; Fausnaugh et al., 2016), was used. Prior to the fit, the AD signal was interpolated with the methods described in Sect. 2.4. The V-band was chosen because it has the best overlap with the GROND observations, and the temporal sampling rate is highest of all the AGN STORM bands. It should be noted, however, that the V-band variations lag behind those at

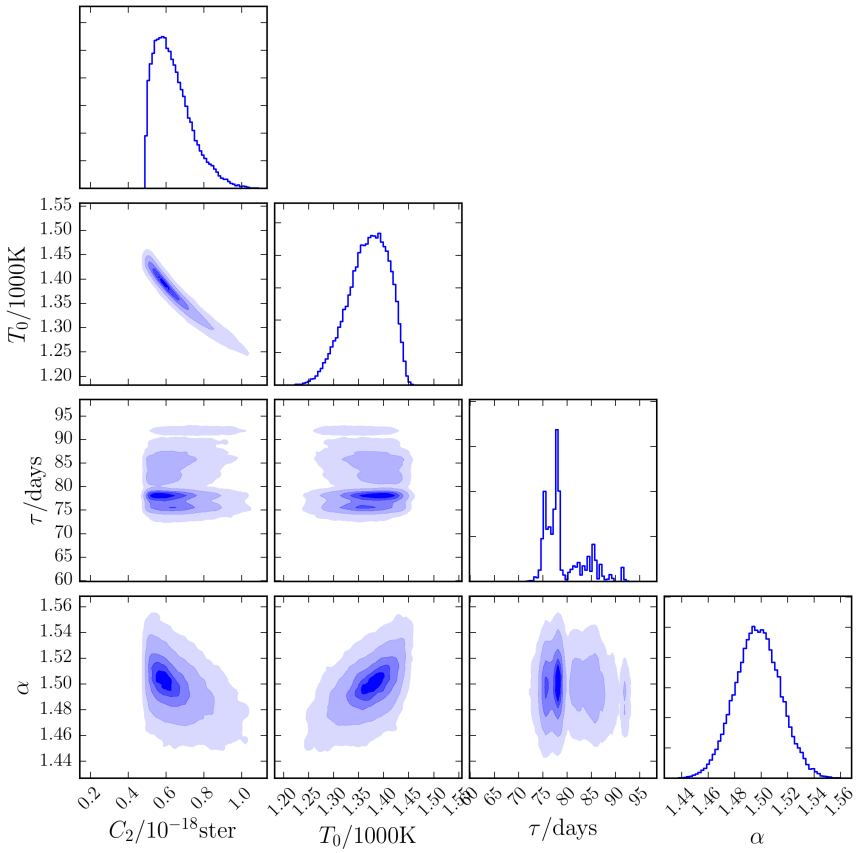

Figure 5.18: *Marginalized posterior probability distributions for the four parameters C_2, T_0, τ, and α of the standard model fit for NGC 5548.*

the shortest UV continuum bands measured from Hubble Space Telescope Cosmic Origins Spectrograph data by $\sim$ 2 days, so that the NIR lag measured relative to V-band slightly underestimates the true distance from the continuum that is most strongly driving the NIR variations. For the analysis in Sect. 5.5, this slight offset was added to the best-fit delay for NGC 5548 given in Table 5.5.

In Fig. 5.15, the temporal evolution of the Ark 120 data and model fluxes are shown for the g', J, and K bands in the first three panels, and the SED is shown in the last panel for one exemplary epoch. Best-fit parameters of this fit are $\tau = 108.0 \pm 1.4$ days, $T_0 = 1.701 \pm 20$ K, and $\alpha = 1.77 \pm 0.03$ (for the complete set of parameters see Table 5.5). The cornerplot of the parameters C_2,T_0,τ, and α is given in Fig. 5.16.
It is worth to note that this target shows temperatures close to the inferred sublimation temperature for NGC 3227 ($\approx$ 1700 K), but is not found at sublimation. As already pointed out in Sect. 5.3.5, the temperatures inferred with this model do not represent the temper-

Table 5.5: *Global mean and errors for the parameters of the targets NGC 4151, NGC 3227, Ark 120, and NGC 5548. In Col. (1), the notation τ_0 refers both to the initial reverberation delay τ_0 in the sublimation model, but also to the constant delay τ (denoted as τ_1 in Sect. 2.2.1) in the standard model. Similarly, the notation $C_{2,0}$ here refers to the initial value of the blackbody constant in the sublimation model, but also to the constant value of C_2 in the standard model. For NGC 3227, only the best-fit values of the sublimation model are listed.*

Parameter	Unit	NGC 4151 (P1)	NGC 4151 (P2)	NGC 3227	Ark 120	NGC 5548
C_1	–	0.78 ± 0.01	0.78 ± 0.01	0.24 ± 0.01	0.25 ± 0.01	0.46 ± 0.01
$C_{2,0}$	10^{-18}ster	4.63 ± 0.33	3.52 ± 0.22	0.59 ± 0.10	0.51 ± 0.02	0.64 ± 0.1
T_0	1000K	1.392 ± 0.020	1.455 ± 0.018	1.626 ± 0.060	1.701 ± 0.020	1.371 ± 0.040
τ_0	days	42.5 ± 4.0	29.6 ± 1.7	34.1 ± 1.6	108.0 ± 1.4	79.4 ± 4.0
α	–	1.65 ± 0.07	1.63 ± 0.04	1.95 ± 0.04	1.77 ± 0.03	1.50 ± 0.02
ν	–	0.96 ± 0.04	0.81 ± 0.03	1.00 (fixed)	1.06 ± 0.05	0.97 ± 0.07

Table 5.6: *Characteristic quantities of the targets of the analyzed sub-sample. For NGC 3227, only the values of the sublimation model are listed.*

Target	$\langle V \rangle$ 10^{-13}Wm$^{-2}\mu^{-1}$m	$\langle T \rangle$ K	$\langle \tau \rangle$ days	d Mpc	$\langle L_V \rangle$ 10^{35} W	$F_{\rm var}$
NGC 4151 (P1)	3.59	1424	42.5	17.7	7.38	0.08
NGC 4151 (P2)	1.65	1308	29.6	17.7	3.44	0.35
NGC 3227	1.99	1626	36.7	21.1	5.80	0.17
Ark 120	0.69	1627	108.0	140.2	88.55	0.14
NGC 5548	0.77	1393	81.4	76.6	29.53	0.13

ature of the innermost dust clouds alone, but an average temperature of those clouds that contribute significantly to the NIR fluxes. In that regard, a different radial dust distribution, characterized by a different radial distribution index β, could have significant influence on this averaged temperature. Indeed, there is a tendency that more luminous AGNs show more compact radial dust distributions (Hönig et al., 2010), while the one for NGC 3227 is very flat.

In Fig. 5.17, the temporal evolution of the NGC 5548 data and model fluxes are shown for the g', J, and K bands in the first three panels, and the SED is shown in the last panel for one exemplary epoch. Best-fit parameters of this fit are $\tau = 79.4 \pm 4.0$ days, $T_0 = 1.371 \pm 40$ K, and $\alpha = 1.50 \pm 0.02$ (for the complete set of parameters see Table 5.5). The cornerplot of the parameters C_2,T_0,τ, and α is given in Fig. 5.18. The reverberation delay is obviously not very well determined, which is caused by a rather low variability in the observed time range, combined with improvable temporal sampling.

5.5 Sample analysis

In this Section, a summary of results is presented on the sub-sample of the first four type 1 AGNs that have been analyzed so far with this method, namely the targets NGC 4151,

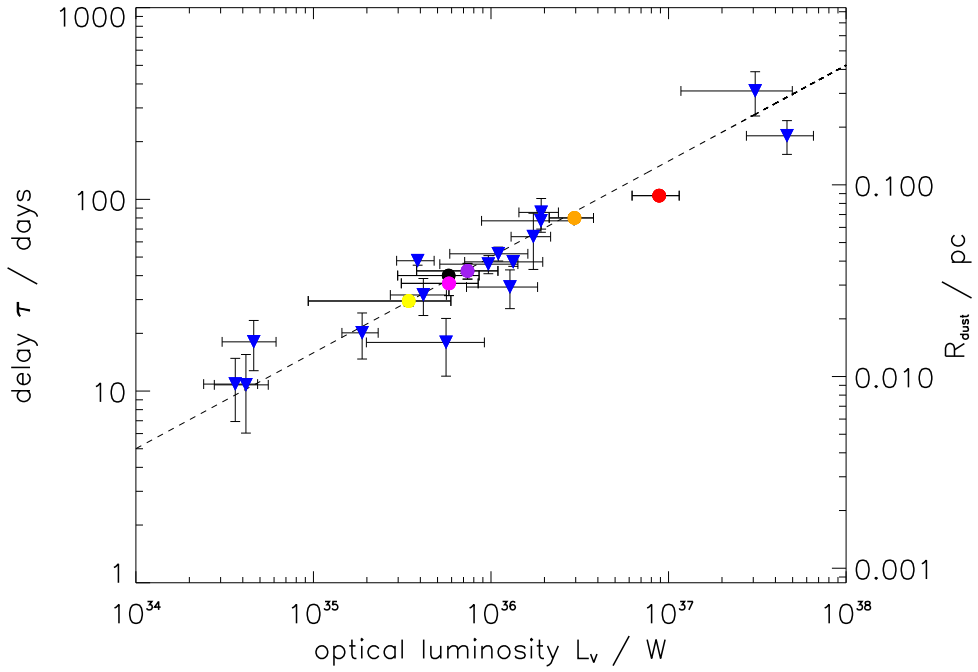

Figure 5.19: *For each target, the mean hot dust reverberation delay $\langle\tau\rangle$ resp. the mean size of the NIR hot dust torus $\langle s\rangle$ is plotted against the mean V-band luminosity $\langle L_V\rangle$. Blue triangles are data points taken from Suganuma et al. (2006), the circles represent the data points derived with the method presented here (purple: NGC 4151 P1, yellow: NGC 4151 P2, magenta: NGC 3227 sublimation model, black: NGC 3227 standard model, red: Ark 120, orange: NGC 5548). Overplotted (dashed line) is the relation $\tau = p_\tau \cdot L_V^{1/2}$ resp. $s = p_s \cdot L_V^{1/2}$.*

NGC 3227, Ark 120, and NGC 5548.

Size-luminosity relation

For all AGNs of this sub-sample – except for NGC 3227 – the standard model was sufficient to describe each data set, and no dust sublimation events were observed. The best-fit parameters for NGC 4151, Ark 120, and NGC 5548 are summarized in Table 5.5. As discussed in Sect. 4.5.3, for NGC 4151, the dataset was split into two parts (epochs 1-6 versus epochs 10-29), as they were found to be qualitatively different, with distinct luminosities and reverberation lags.

Table 5.6 presents for each data set the mean V-band flux $\langle V\rangle$ (estimated for NGC 4151 using $\langle z\rangle$ and the best-fit power-law slope α, and for the others targets using $\langle g'\rangle$ and α), mean blackbody temperature $\langle T\rangle$, mean reverberation delay $\langle\tau\rangle$, distance d, mean V-band

luminosity $\langle L_V \rangle$, and the variability $F_{\rm var}$ of the AD band signal. Following Suganuma et al. (2006), this quantity is given by:

$$F_{\rm var} = \frac{\sqrt{\sigma^2 - \delta^2}}{\langle V \rangle} \,, \tag{5.6}$$

where δ and σ are the measurement uncertainty and the standard deviation of the V-band flux. $F_{\rm var}$ is used as the horizontal error bars in the size-luminosity relation plotted in Fig. 5.19. As in Suganuma et al. (2006), the distance of each target is calculated using the radial velocity corrected for cosmic background (from NED) and a value of $H_0 = 70 \mathrm{kms}^{-1}\mathrm{Mpc}^{-1}$.

Figure 5.19 shows for each target the mean reverberation delay $\langle \tau \rangle$ resp. the mean size of the hot dust torus $\langle s \rangle$ plotted against the mean V-band luminosity, for the four targets analyzed here (with two data points for NGC 4151) plus all targets published in Suganuma et al. (2006). As can be seen, the data points fit very well into the plot and nicely follow the $\tau \propto L^{1/2}$ resp. $s \propto L^{1/2}$ relation. A proportionality constant of $p_\tau = 5.00 \cdot 10^{-17} \pm 1.44 \cdot 10^{-17}$days $\mathrm{W}^{-0.5}$ is derived for the τ-L-relation resp. $p_s = 4.21 \cdot 10^{-20} \pm 1.21 \cdot 10^{-20}$pc $\mathrm{W}^{-0.5}$ for the s-L-relation using the complete data set.

Intrinsic source properties

The above size-luminosity relation suggests for a sample of AGN a common dust radius for targets of equal brightness, which implies a common hot dust temperature. One can give this claim a closer look and check in the multi-band data how best-fit accretion disk flux and hot dust temperature relate to each other. A basic assumption of the model is that if the dust radius in an AGN deviates from the sample mean radius suggested by the size-luminosity relation, then the dust temperature should change.

In Fig. 5.20, the mean blackbody temperature versus the mean AD flux incident at the location of the hot dust is plotted for each target. The incident AD flux at $R_{\rm dust}$ is given by:

$$F_{\rm inc} = \frac{L_V}{4\pi(c\tau)^2} \,. \tag{5.7}$$

As can be seen, the derived data points are well described by a $T \propto F_{\rm inc}^{1/4}$ relation, as it should be (considering the Stefan-Boltzmann law). A mean proporionality constant of $p_T = 99.1 \pm 10.4 \mathrm{KW}^{-1/4}\mathrm{m}^{1/2}$ is obtained for this relation, overplotted in Fig. 5.20. In particular for NGC 3227, further overplotted is the result from the standard model fit (black circle) which does not account for the observed sublimation event. This data point appears significantly off the Stefan-Boltzmann-track, which demonstrates that in case of sublimation events, the sublimation model more adequately describes the individual photometry data and offers a more unified way to describe such multi-band multi-epoch reverberation data.

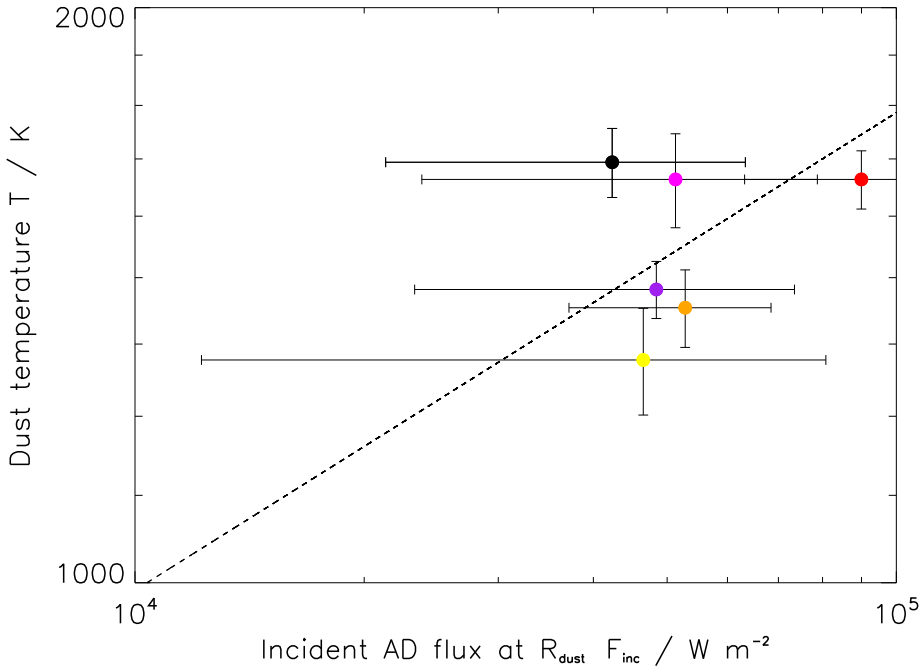

Figure 5.20: *For each target, the mean hot dust blackbody temperature $\langle T \rangle$ is plotted against the mean AD flux incident at the location of the hot dust $\langle F_{\rm inc} \rangle$. Shown are the data points for the four so far analyzed targets with the presented method (purple: NGC 4151 P1, yellow: NGC 4151 P2, magenta: NGC 3227 sublimation model, black: NGC 3227 standard model, red: Ark 120, orange: NGC 5548). The data points are consistent with a slope of 1/4 in this logarithmic plot, i.e., a relation of the form $T \propto F_{\rm inc}^{1/4}$. Overplotted (dashed line) is the relation $T = p_T \cdot F_{\rm inc}^{1/4}$ (see text of Sect. 5.5).*

In their analysis of NGC 4151, Hönig & Kishimoto (2011) have found a value of $\nu \approx 0.4$ for the response of the K-band temperature variability to the AD variability. In contrast, for the targets that are well-described by the standard model presented in this work, namely NGC 4151, NGC 5548, and Ark 120, a consistent best-fit value of $\nu \approx 1$ is found. For these targets, the AD variability seems to be 100% reprocessed by the hot dust. For NGC 3227, to avoid degeneracies between the fit parameters, we fixed $\nu = 1$, as justified by the other targets. It has been checked and ruled out that choosing a different $\nu \neq 1$ would give significantly improved fits for NGC 3227.

5.6 Conclusions

In this Chapter, results were presented from the analysis of the first four targets (three GROND targets, one Omega 2000 target) from the AGN hot dust reverberation campaign carried out in this work. These are the findings:

- Five new points have been added to the size-luminosity relation for the hot dust around AGNs in the NIR. The obtained results fit very well into the established $s \propto L^{1/2}$ relation.
- Moreover, it has been shown that the developed method produces consistent results in the T versus $F_{\rm inc}$ relation.
- For all targets that are fit well by the standard model without dust sublimation events, a value close to unity is found for the variability factor ν, i.e., the AD variablity is 100% reprocessed by the hot dust in these objects.
- Specifically for NGC 3227, two alternative reverberation models were fit to the data, and indications for a dust sublimation event observed in the nucleus of that galaxy have been found. The difference between the inferred reverberation delays with the standard and the sublimation model is roughly 15%, and thus substantially lower than the total scatter in the radius-luminosity relation. However, especially for measurements long after the last sublimation event, a larger deviation of the current reverberation radius from the sublimation radius is expected.
- The presented sublimation model offers a unified model description for hot AGN dust data with and without sublimation events, which will inevitably occur in larger sample sizes and over longer monitoring periods due to the intrinsic variability of AGNs.
- NGC 3227, having dust close to sublimation temperatures, is a very promising target to investigate dust sublimation and dust surface re-illumination processes in AGNs with hot dust reverberation observations. Further monitoring with a closer sampling would be desirable, to be able to further constrain the model parameters, and to develop a more complex and realistic dust sublimation and re-illumination model.

6 Conclusions and outlook

6.1 Conclusions

In this work, an extended hot dust reverberation model has been developed, and successfully applied to multi-epoch multi-wavelength data using a maximum likelihood approach, in order to investigate the evolution of characteristic parameters of the hot dust around type 1 AGNs in response to varying accretion disk emission.
Optical to NIR photometric observations have been planned and carried out for a sample of 24 type 1 AGNs, with the Omega 2000 and GROND instruments. Starting off with rather simple single-epoch SED fits, an advanced multi-epoch multi-wavelength model was developed in the course of this thesis, and sophisticated methods were implemented for the interpolation of the input accretion disk signal to the model, and for the inference of the best model parameters. This model was first developed as a standard reverberation model without sublimation, as is also found to be the case for all dust reverberation approaches found in the literature, with the dust signal being a delayed and smoothed version of the accretion disk variations. In the course of this work, the reverberation idea has been extended, and for the first time a tool has been developed to verify the existence of sublimation events in AGN monitoring data.

With the presented methods, four of the 24 observed AGNs have been analysed within the course of this work[1]. The findings are:

- The presented method is capable of characterizing the hot dust in AGNs beyond an exclusive determination of the reverberation delay τ.
- Five new points have been added to the size-luminosity relation for the hot dust around AGNs in the NIR wavelength regime. The obtained results fit very well into the established $s \propto L^{1/2}$ relation.
- Moreover, it has been shown that the method developed in this work produces consistent results in the T versus F_{inc} relation.
- Three of the four analysed targets can be described within a standard dust reverberation model without sublimation. For these targets, the hot dust is not at sublimation temperatures yet, and it seems that the inner rim of the dusty torus is located beyond the sublimation radius in the observed time span. The hot dust emission, and moreover, the host dust temperature closely track the AD flux variations on a short-term response timescale, as given by the hot dust reverberation delay for each target.

[1] The analysis of the remaining targets will be carried out within the group, and will be published elsewhere.

- Long-term changes in the hot dust reverberation delay, caused by a reformation of hot dust at innermost radii, can be detected with the presented method. Specifically for the galaxy NGC 4151, a change of the the reverberation delay of ≈13 days in 2 years has been found.
- Moreover, the presented method is capable of detecting short-term increases in the hot dust reverberation delay – caused by destruction of innermost dust clouds due to sublimation – as well as a subsequent re-illumination of the hot dust surface. Specifically for NGC 3227, indications for dust sublimation in the nucleus have been found. A better temporal sampling in future observations is clearly desirable to place reliable constraints on all model parameters.
- For all targets that are fit well by the standard model without dust sublimation, a value close to unity is found for the variability factor ν, i.e., the AD variablity is 100% reprocessed by the hot dust in these objects.
- Whereas the inferred parameters always represent an average over all inner dust clouds that contribute significantly to the observed NIR fluxes, the presented method also enables to measure the reverberation delay of each NIR band alone (when fixing part of the other parameters) and thereby "resolve" the wavelength stratification of the dust location, confirming that there is even hotter dust, located further in than the K-band dust that is typically used for hot dust reverberation.
- With the presented method, one can reliably infer whether or not the hot dust around an AGN is observed at or below sublimation. Independent of uncertainties in the absolute temperature level, this is achieved by diagnozing whether or not the hot dust reponse is suitably described by a delayed and smoothed-out version of the AD variability signal. Whereas it has already been stated in the literature that a subtantial part of the intrinsic scatter in the size-luminosity relation is presumably caused by a non-trivial variation of the inner hot dust radius with the AD luminosity, in this work direct proof has been presented that typically, the innermost hot dust in AGN tori is found below sublimation temperatures in the majority of targets.

6.2 Outlook

In this work, an approach has been presented that is able to detect sublimation events. To facilitate a detection of more of such events in future observations, one needs to concentrate on AGNs close to sublimation, via temperature monitoring. Specifically, to constrain the re-illumination timescale $\mathscr{T}_{\rm ref}$, one then needs monitor closely and intensely in time.

Concerning the diagnostics whether or not the dust in an observed target undergoes a sublimation event, the presented model is robust against uncertainties in the derived absolute flux levels. However, to be able to reliably identify promising candidates that show temperatures close to sublimation, one needs perform precise temperature measurements, i.e., one has to obtain very accurate absolute flux levels. For that purpose, it is advisable to

concentrate on nearby galaxies, in order avoid PSF-bulge degeneracies in the flux decomposition, and to obtain at least one contemporaneous spectrum per target to facilitate reliable emission line corrections.

Moreover, it would be desirable to allow for continuous changes of the hot dust blackbody constant in the presented model, not only during sublimation times, but also during the process of recovery of the blackbody constant (re-illumination). Furthermore, dust reformation could be incorporated into the model, allowing for the continuous decrease of the reverberation delay in dim AD times, in order to be able to constrain reformation timescales from long-term data sets. This might also offer the possibility to discriminate between intrinsic versus extrinsic dust reformation for well-sampled data sets.

To be able to measure and disentangle sublimation and reformation timescales from cross-correlation analyses between single-target hot dust radii and (time-averaged) AD fluxes, it is indispensable to obtain additional radius measurements for single targets, preferentially for objects that have been closely monitored already. The well-studied galaxy NGC 4151 seems a particulary suitable target for this purpose.

An inclusion of dust sublimation events into radiative transfer clumpy torus models would be desirable.

Implementing these modifications will facilitate a better understanding of dust sublimation and reformation processes as well as the involved timescales, and provide a tool for relating each radius (delay) measurement with its appropriate associated luminosity, i.e., the luminosity that is causally related to the delay. Such an assignment is needed to reduce the intrinsic scatter in size-luminosity relations and to derive appropriate measures of the sizes and distances of AGN dust tori.
For targets undergoing a sublimation event, at the very start of the sublimation process, there is a unique relation between the reverberation hot dust radius (delay) and the AD luminosity. It is expectable that the scatter in the size-luminosity-relation for a sample of such targets tracing the sublimation radius would be significantly reduced.

However, with the current scatter in the size-luminosity relation, dust tori as standard rulers seems to provide a more reliable method for a potential use of AGN dust tori as a tool to constrain cosmological models.

The origin of dust remains an open question. Potentially observable differences between the two scenarios, i.e., “dust from outside” versus “dust from inside”, could be:

- In the “dust from outside scenario”, dust will likely accumulate at the innermost possible radius, thus the sublimation radius, assuming that it has had enough time to get there after potential sublimation events. It will be found outside the sublimation radius only whenever the AD luminosity has decreased on timescales shorter than the dynamical timescale. In contrast, dust coming from inside, condensating in BLR

clouds, would only form well outside the sublimation radius (Elvis et al., 2002). It might be possible to discriminate between the two scenarios with detailed modelling.

- Concerning the radial dust distribution, in the "'dust from outside" scenario, one would expect an accumulation of dust at the innermost radius, whereas the outflowing clouds in the "dust from inside" scenario would not exhibit such a dense accumulation.

- After a sublimation event, comparing expected to observed reformation timescales might help to discriminate between the two scenarios. The expected reformation timescale can be estimated by $(R_{\mathrm{dust;2}} - R_{\mathrm{dust;1}})/v$ in the "'dust from outside" scenario, where $R_{\mathrm{dust;2}} - R_{\mathrm{dust;1}}$ is the difference in observed dust radii before and after reformation, and v is the inflow velocity (for which an upper limit can be estimated by the freefall velocity). For "dust from inside", condensation of dust in outflowing BLR clouds occurs roughly 3-9 years after the initial launching of clouds (then being roughly 3 times as big as initially, Elvis et al. (2002)) from the BLR , when they have expanded enough to meet the dust condensation conditions.

Observed timescales for NGC 4151 (see text of Sect. 4.5.3, but also Fig. 1.9) give slight preference to the "dust from inside" scenario, as the estimated reformation timescales for dust moving in from outside seem too long to match the data. While with the data sets at hand, the "dust from outside" scenario cannot be excluded, it seems likely that intrinsic dust formation contributes at least part of the (re-) formed dust.

An imporant question is, however, even if one would be able to discriminate between the different dust formation mechanisms in AGNs: what does this mean? Can quasars be net producers of dust? Would the dust be truly formed in the outflows, or merely re-formed? As already stated by Dwek & Cherchneff (2011), the "... effectiveness of AGNs as sources of newly-formed dust remains unclear. The origin of the dense broad-line-emitting clouds, and whether they were initially dusty so that the AGN merely reformed pre-existing dust, are questions that need to be addressed to ascertain their role as dust sources in quasars".

Publications

Paper I: Schnülle, K., Pott, J.-U., Rix, H.-W., et al. 2013: Dust physics in the nucleus of NGC 4151, A&A, 557, L13

Paper II: Schnülle, K., Pott, J.-U., Rix, H.-W., et al. 2015: Monitoring the temperature and reverberation delay of the circumnuclear hot dust in NGC 4151, A&A, 578, A57

Paper III: Schnülle, K., Pott, J.-U., Rix, H.-W., et al. 2017: AGN hot dust reverberation campaign III. – Modeling dust sublimation in the nucleus of NGC 3227, close to submission

Chapter 2 of this thesis makes use of the corresponding presentations of the methods in Paper I, Paper II and Paper III. Further, Paper I has been used for Chapter 3, Paper II for Chapter 4, and Paper III for Chapter 5.

Bibliography

Alard, C. 2000, A&AS, 144, 363

Alard, C. & Lupton, R. H. 1998, ApJ, 503, 325

Alonso-Herrero, A., Quillen, A. C., Simpson, C., Efstathiou, A., & Ward, M. J. 2001, AJ, 121, 1369

Alonso-Herrero, A., Ramos Almeida, C., Mason, R., et al. 2011, ApJ, 736, 82

Antonucci, R. 1993, ARAA, 31, 473

Antonucci, R. R. J. & Miller, J. S. 1985, ApJ, 297, 621

Baron, D., Stern, J., Poznanski, D., & Netzer, H. 2016, ApJ, 832, 8

Barvainis, R. 1987, ApJ, 320, 537

Bauer, A., Baltay, C., Coppi, P., et al. 2009, ApJ, 696, 1241

Beckmann, V. & Shrader, C. R. 2012, Active Galactic Nuclei

Bentz, M. C., Denney, K. D., Cackett, E. M., et al. 2006, ApJ, 651, 775

Bentz, M. C., Denney, K. D., Grier, C. J., et al. 2013, ApJ, 767, 149

Bentz, M. C., Peterson, B. M., Netzer, H., Pogge, R. W., & Vestergaard, M. 2009, ApJ, 697, 160

Berger, J. P. & Segransan, D. 2007, New Astronomy Review, 51, 576

Bianchi, S., Corral, A., Panessa, F., et al. 2008, MNRAS, 385, 195

Bianchi, S., Maiolino, R., & Risaliti, G. 2012, Advances in Astronomy, 2012, 782030

Blandford, R. D., Netzer, H., Woltjer, L., Courvoisier, T. J.-L., & Mayor, M., eds. 1990, Active Galactic Nuclei, 97

Brooks, S. P. & Gelman, A. 1998, Journal of Computational and Graphical Statistics, 7, 434

Burtscher, L., Jaffe, W., Raban, D., et al. 2009, ApJL, 705, L53

Chiaberge, M., Capetti, A., & Celotti, A. 2002, A&A, 394, 791

Clavel, J., Reichert, G. A., Alloin, D., et al. 1991, ApJ, 366, 64

Crenshaw, D. M., Kraemer, S. B., Boggess, A., et al. 1999, ApJ, 516, 750

Czerny, B., Doroshenko, V. T., Nikołajuk, M., et al. 2003, MNRAS, 342, 1222

Czerny, B. & Hryniewicz, K. 2011, A&A, 525, L8

De Rosa, G. & et al. 2017, in preparation

Dietrich, M., Kollatschny, W., Peterson, B. M., et al. 1993, ApJ, 408, 416

Dwek, E. & Cherchneff, I. 2011, ApJ, 727, 63

Edelson, R., Gelbord, J. M., Horne, K., et al. 2015, ApJ, 806, 129

Elitzur, M. & Ho, L. C. 2009, ApJL, 701, L91

Elitzur, M. & Shlosman, I. 2006, ApJL, 648, L101

Elvis, M. 2014, Nature, 515, 498

Elvis, M., Marengo, M., & Karovska, M. 2002, ApJL, 567, L107

Fanti, R., Kellermann, K., & Setti, G. 1984, Science, 226, 473

Fausnaugh, M. M., Denney, K. D., Barth, A. J., et al. 2016, ApJ, 821, 56

Gaskell, C. M., Goosmann, R. W., Antonucci, R. R. J., & Whysong, D. H. 2004, ApJ, 616, 147

Gelman, A. & Rubin, D. B. 1992, Statistical science, 457

Granato, G. L. & Danese, L. 1994, MNRAS, 268, 235

Greiner, D. J. 2009, GROND calibration issues, `http://www.mpe.mpg.de/~jcg/GROND/calibration.html`, accessed: 2017-04-14

Greiner, J., Bornemann, W., Clemens, C., et al. 2008, PASP, 120, 405

Grier, C. J., Peterson, B. M., Horne, K., et al. 2013, ApJ, 764, 47

Guhathakurta, P. & Draine, B. T. 1989, ApJ, 345, 230

Hernitschek, N., Rix, H.-W., Bovy, J., & Morganson, E. 2014, ArXiv e-prints

Hönig, S. F. 2014, ApJL, 784, L4

Hönig, S. F., Beckert, T., Ohnaka, K., & Weigelt, G. 2006, A&A, 452, 459

Hönig, S. F. & Kishimoto, M. 2010, A&A, 523, A27

Hönig, S. F. & Kishimoto, M. 2011, A&A, 534, A121

Hönig, S. F., Kishimoto, M., Gandhi, P., et al. 2010, A&A, 515, A23

Hönig, S. F., Watson, D., Kishimoto, M., & Hjorth, J. 2014, Nature, 515, 528

Jaffe, W., Meisenheimer, K., Röttgering, H. J. A., et al. 2004, Nature, 429, 47

Kaspi, S., Maoz, D., Netzer, H., et al. 2005, ApJ, 629, 61

Kawaguchi, T. & Mori, M. 2010, ApJL, 724, L183

Kimura, H., Mann, I., Biesecker, D. A., & Jessberger, E. K. 2002, Icarus, 159, 529

Kishimoto, M., Antonucci, R., Blaes, O., et al. 2008, Nature, 454, 492

Kishimoto, M., Hönig, S. F., Antonucci, R., et al. 2011a, A&A, 527, A121

Kishimoto, M., Hönig, S. F., Antonucci, R., et al. 2009, A&A, 507, L57

Kishimoto, M., Hönig, S. F., Antonucci, R., et al. 2013, ApJL, 775, L36

Kishimoto, M., Hönig, S. F., Antonucci, R., et al. 2011b, A&A, 536, A78

Kishimoto, M., Hönig, S. F., Beckert, T., & Weigelt, G. 2007, A&A, 476, 713

Kobayashi, H., Kimura, H., Watanabe, S.-i., Yamamoto, T., & Müller, S. 2011, Earth, Planets, and Space, 63, 1067

Kobayashi, Y., Sato, S., Yamashita, T., Shiba, H., & Takami, H. 1993, ApJ, 404, 94

Kollatschny, W. & Zetzl, M. 2013, A&A, 551, L6

Koratkar, A. P. & Gaskell, C. M. 1991, ApJs, 75, 719

Koshida, S., Minezaki, T., Yoshii, Y., et al. 2014, ApJ, 788, 159

Koshida, S., Yoshii, Y., Kobayashi, Y., et al. 2009, ApJL, 700, L109

Kovács, Z., Mall, U., Bizenberger, P., Baumeister, H., & Röser, H.-J. 2004, in SPIE Conference Series, Vol. 5499, Optical and Infrared Detectors for Astronomy, ed. J. D. Garnett & J. W. Beletic, 432–441

Krolik, J. H. 2007, ApJ, 661, 52

Krolik, J. H. & Begelman, M. C. 1988, ApJ, 329, 702

Lacy, M., Canalizo, G., Rawlings, S., et al. 2005, MemSAI, 76, 154

Lamb, D. Q. & Reichart, D. E. 2000, ApJ, 536, 1

Landt, H., Bentz, M. C., Ward, M. J., et al. 2008, ApJs, 174, 282

Landt, H., Elvis, M., Ward, M. J., et al. 2011, MNRAS, 414, 218

Lawrence, A. & Elvis, M. 2010, ApJ, 714, 561

MacLeod, C. L., Ivezić, Ž., Kochanek, C. S., et al. 2010, ApJ, 721, 1014

Maiolino, R., Nagao, T., Marconi, A., et al. 2006, MemSAI, 77, 643

Maiolino, R., Salvati, M., Bassani, L., et al. 1998, A&A, 338, 781

Maoz, D., Netzer, H., Peterson, B. M., et al. 1993, ApJ, 404, 576

Martínez-Sansigre, A., Rawlings, S., Garn, T., et al. 2006a, MNRAS, 373, L80

Martínez-Sansigre, A., Rawlings, S., Lacy, M., et al. 2006b, MNRAS, 370, 1479

McLean, B. J., Golombek, D. A., Hayes, J. J. E., & Payne, H. E., eds. 1998, IAU Symposium, Vol. 179, New Horizons from Multi-Wavelength Sky Surveys

Mengersen, K. & Robert, C. 2003, in Bayesian Statistics 7, ed. J. Bernardo, M. Bayarri, J. Berger, A. Dawid, D. Heckerman, A. Smith, & M. West (Oxford University Press, Oxford)

Meusinger, H., Hinze, A., & de Hoon, A. 2011, A&A, 525, A37

Minezaki, T., Yoshii, Y., Kobayashi, Y., et al. 2004, ApJL, 600, L35

Monnier, J. D. 2003, Reports on Progress in Physics, 66, 789

Mor, R. & Netzer, H. 2012, MNRAS, 420, 526

Mor, R., Netzer, H., & Elitzur, M. 2009, ApJ, 705, 298

Morganson, E., Burgett, W. S., Chambers, K. C., et al. 2014, ApJ, 784, 92

Morganson, E., De Rosa, G., Decarli, R., et al. 2012, AJ, 143, 142

Nayakshin, S. 2005, MNRAS, 359, 545

Nenkova, M., Ivezić, Ž., & Elitzur, M. 2002, ApJL, 570, L9

Nenkova, M., Sirocky, M. M., Ivezić, Ž., & Elitzur, M. 2008a, ApJ, 685, 147

Nenkova, M., Sirocky, M. M., Nikutta, R., Ivezić, Ž., & Elitzur, M. 2008b, ApJ, 685, 160

Nicastro, F., Martocchia, A., & Matt, G. 2003, ApJL, 589, L13

Nikutta, R., Elitzur, M., & Lacy, M. 2009, ApJ, 707, 1550

Ogle, P., Whysong, D., & Antonucci, R. 2006, ApJ, 647, 161

Oknyanskij, V. L. 1999, Odessa Astronomical Publications, 12, 99

Oknyanskij, V. L., Lyuty, V. M., Taranova, O. G., & Shenavrin, V. I. 1999, Astronomy Letters, 25, 483

Oliva, E., Origlia, L., Maiolino, R., & Moorwood, A. F. M. 1999, A&A, 350, 9

Peng, C. Y., Ho, L. C., Impey, C. D., & Rix, H.-W. 2002, AJ, 124, 266

Peterson, B. M. 1993, PASP, 105, 247

Peterson, B. M. 1997, An Introduction to Active Galactic Nuclei

Peterson, B. M. 2006, in Lecture Notes in Physics, Berlin Springer Verlag, Vol. 693, Physics of Active Galactic Nuclei at all Scales, ed. D. Alloin, 77

Peterson, B. M. & Agn Storm Team. 2015, in American Astronomical Society Meeting Abstracts, Vol. 225, American Astronomical Society Meeting Abstracts, 103.01

Peterson, B. M., Balonek, T. J., Barker, E. S., et al. 1991, ApJ, 368, 119

Peterson, B. M., Ferrarese, L., Gilbert, K. M., et al. 2004, ApJ, 613, 682

Peterson, B. M. & Horne, K. 2006, in Planets to Cosmology: Essential Science in the Final Years of the Hubble Space Telescope, ed. M. Livio & S. Casertano, 89

Pier, E. A. & Krolik, J. H. 1992, ApJL, 399, L23

Pogge, R. W. 1988, ApJ, 332, 702

Pott, J.-U., Malkan, M. A., Elitzur, M., et al. 2010, ApJ, 715, 736

Press, W. H., Rybicki, G. B., & Hewitt, J. N. 1992, ApJ, 385, 404

Rakshit, S., Petrov, R. G., Meilland, A., & Hönig, S. F. 2015, MNRAS, 447, 2420

Ramos Almeida, C., Levenson, N. A., Rodríguez Espinosa, J. M., et al. 2009, ApJ, 702, 1127

Rayner, J. T., Toomey, D. W., Onaka, P. M., et al. 2003, PASP, 115, 362

Ridgway, S. E., Harrison, C., Lacy, M., et al. 2009, in RMxAA Conference Series, Vol. 35, Revista Mexicana de Astronomia y Astrofisica Conference Series, 239–240

Riffel, R. A., Storchi-Bergmann, T., & McGregor, P. J. 2009, ApJ, 698, 1767

Rybicki, G. B. & Press, W. H. 1992, ApJ, 398, 169

Ryden, B., Peterson, B. M., & Demianski, M. 2010, American Journal of Physics, 78, 127

Schartmann, M., Burkert, A., Krause, M., et al. 2010, MNRAS, 403, 1801

Schartmann, M., Meisenheimer, K., Camenzind, M., et al. 2008, A&A, 482, 67

Schlafly, E. F. & Finkbeiner, D. P. 2011, ApJ, 737, 103

Schlegel, D. J., Finkbeiner, D. P., & Davis, M. 1998, ApJ, 500, 525

Schmidt, K. B., Marshall, P. J., Rix, H.-W., et al. 2010, ApJ, 714, 1194

Schnülle, K. & et al. 2017, in preparation

Schnülle, K., Pott, J.-U., Rix, H.-W., et al. 2013, A&A, 557, L13

Schnülle, K., Pott, J.-U., Rix, H.-W., et al. 2015, A&A, 578, A57

Seyfert, C. K. 1943, ApJ, 97, 28

Shappee, B. J. & Stanek, K. Z. 2011, ApJ, 733, 124

Shi, Y., Rieke, G. H., Hines, D. C., et al. 2006, ApJ, 653, 127

Siverd, R. J., Beatty, T. G., Pepper, J., et al. 2012, ApJ, 761, 123

Smith, D. A. & Done, C. 1996, MNRAS, 280, 355

Stern, J., Hennawi, J. F., & Pott, J.-U. 2015, ApJ, 804, 57

Storchi-Bergmann, T., Mulchaey, J. S., & Wilson, A. S. 1992, ApJL, 395, L73

Suganuma, M., Yoshii, Y., Kobayashi, Y., et al. 2006, ApJ, 639, 46

Sulentic, J. W., Marziani, P., & D'Onofrio, M. 2012, Fifty Years of Quasars: From Early Observations and Ideas to Future Research, 386, 549

Swain, M., Vasisht, G., Akeson, R., et al. 2003, ApJL, 596, L163

Ter Braak, C. J. F. 2006, Statistics and Computing, 16, 239

Trèvese, D., Kron, R. G., & Bunone, A. 2001, ApJ, 551, 103

Tristram, K. R. W., Meisenheimer, K., Jaffe, W., et al. 2007, A&A, 474, 837

Tristram, K. R. W., Raban, D., Meisenheimer, K., et al. 2009, A&A, 502, 67

Veilleux, S., Goodrich, R. W., & Hill, G. J. 1997, ApJ, 477, 631

Véron-Cetty, M.-P. & Véron, P. 2010, A&A, 518, A10

Wada, K. & Tomisaka, K. 2005, ApJ, 619, 93

Ward, M., Elvis, M., Fabbiano, G., et al. 1987, ApJ, 315, 74

Watabe, Y. & Umemura, M. 2005, ApJ, 618, 649

Weigelt, G., Hofmann, K.-H., Kishimoto, M., et al. 2012, A&A, 541, L9

Yoshii, Y., Kobayashi, Y., Minezaki, T., Koshida, S., & Peterson, B. A. 2014, ApJL, 784, L11

Zheng, W., Kriss, G. A., Telfer, R. C., Grimes, J. P., & Davidsen, A. F. 1997, ApJ, 475, 469

Zu, Y., Kochanek, C. S., & Peterson, B. M. 2011, ApJ, 735, 80

Acknowledgments

First of all, I would like to thank my supervisors Hans-Walter Rix and Jörg-Uwe Pott for giving me the opportunity to do my PhD at MPIA, and for their scientific advice. I am especially thankful to Jörg-Uwe for facilitating discussions on an equal footing, for showing so much understanding regarding the balance between my family and work, and for agreeing that I finish my PhD from Bremen.

I am highly thankful to Jochen Heidt, who immediately agreed to be the second referee of my dissertation and a member of my PhD committee. Furthermore, I very much enjoyed tutoring the Astro-Lab block course with him. Those two weeks were an interesting and very motivating experience during my PhD. I thank Kees Dullemond for agreeing to be on my thesis committee and for taking part and providing helpful feedback in my three thesis committee meetings.

I am deeply grateful to Brad Peterson for his constant support throughout my PhD, for always believing in me and for being a good friend. Furthermore, I would sincerely like to thank Roberto Decarli, who provided valuable scientific and technical help for me, especially at the beginning of my PhD. It was always fun and very motivating to work with him, due to his careful, kind, and very humorous nature. I would also like to thank Christian Fendt, for his kind offer to be part of my PhD committee, and for all his advice during my PhD time. His door is always open and he takes his time for the students. I always felt welcome and could talk to him whenever I needed advice, and I am very thankful for this. I would also like to thank Reinhard Mundt for his kindness, and for his helpful advice.

Furthermore, I would like to thank my friends at MPIA, especially Maria Wöllert and Deniss Stepanovs. Thank you, Maria, for our walks and conversations and for listening to me whenever I needed someone to talk to. Thank you, Dennis, for the funny philosophical and psychological discussions, and for the numerous table tennis challenges which I very much enjoyed. Moreover, I thank Ina Beckmann for having nice chats at the start or end of work, or in between.

I am deeply thankful to my parents for always supporting me in everything that I do or want to do, for believing in me and for always being there for me and my family. Moreover, I would like to thank my parents-in-law, Anita and Detlef, for their constant support throughout the time of my PhD, especially for taking care of Emmy and Lilly.

Last but not least, I am deeply grateful to my husband, Sebastian, for his constant support. He advised me and was always there for me whenever I needed someone to talk to. Without his reassurance, motivation, and understanding, I might not have finished this work.